Copyright

by

Cameron Myron Knapp

2014

The Thesis Committee for Cameron Myron Knapp
Certifies that this is the approved version of the following thesis:

Thermal Characterization of Direct Metal Deposition

APPROVED BY
SUPERVISING COMMITTEE:

Supervisor: _____
Desiderio Kovar

Co-Supervisor: _____
Sheldon Landsberger

Thermal Characterization of Direct Metal Deposition

by

Cameron Myron Knapp, B.S

Thesis

Presented to the Faculty of the Graduate School of

The University of Texas at Austin

in Partial Fulfillment

of the Requirements

for the Degree of

Master of Science in Engineering

The University of Texas at Austin

May 2014

Dedication

I would like to dedicate this body of work, and my progression to graduate studies to the Knapp family, specifically the memory of Dr. Myron William Knapp and Doris Riggs Knapp, who together made education a family priority. The support of my immediate family; Bret Eric Knapp, Sheryl Ann Knapp, and Trevor Dillon Knapp has given me the inspiration, perseverance, and stability to pursue and successfully achieve a graduate education. They share in this success more than they can comprehend. I am eternally in their debt.

ACKNOWLEDGEMENTS

The temperature distribution in the vicinity of the laser used in direct metal deposition (DMD) plays a critical role in determining the final microstructure and properties of the deposit and the heat-affected zone within the substrate. Samples were produced and studied consisting of AISI 1018 steel powder deposited onto AISI 1018 steel substrates as a single pass or overwritten in multiple passes. The laser power and speed were varied to influence the heat input and the rate of cooling. The use of idealized one dimensional lines allowed for the solution of a quasi-steady state analytical temperature distribution. Numerical predictions were made using the commercial software SysWeld™ for single pass depositions. Peak temperatures and cooling rates were determined at selected locations experimentally using micro-hardness measurements and from microstructural observations. These temperature profiles were compared to thermocouple data taken during deposition. The analytical model, numerical predictions, and experimental results are compared for single pass depositions to determine the extent to which existing commercial codes can accurately model the thermal environment for DMD.

Abstract

Thermal Characterization of Direct Metal Deposition

Cameron Myron Knapp, M.S.E.

The University of Texas at Austin, 2014

Supervisor: Desiderio Kovar

Co-Supervisor: Sheldon Landsberger

The temperature distribution in the vicinity of the laser used in direct metal deposition (DMD) plays a critical role in determining the final microstructure and properties of the deposit and the heat-affected zone within the substrate. A system of deposition samples were studied consisting of AISI 1018 steel powder deposited onto an AISI 1018 steel substrate as a single pass or as overwritten multiple passes. The laser power and speed were varied to influence the heat input and the rate of cooling. The use of idealized one dimensional lines allowed for the solution of a quasi-steady state analytical temperature distribution. Numerical predictions were made using the commercial software SysWeld™ for single pass depositions. Peak temperatures and cooling rates were determined at selected locations experimentally using micro-hardness measurements which were supplemented by obtaining thermocouple data taken during deposition. The analytical model, numerical predictions, and experimental results are compared for single pass depositions to determine the extent to which existing commercial codes can accurately model the thermal environment for DMD.

Table of Contents

List of Figures

Nomenclature

A_S = Cross sectional area of melted substrate

A_{fm} = Cross sectional area of melted filler metal

a_p = Absorptivity of powder

a_s = Absorptivity of substrate

B = Molten pool conduction calibration constant

D_0 = Initial beam diameter

D_1 = Beam diameter at surface

d_{jom} = Jominy distance

ε = Emissivity of molten pool

g = Finite thickness of wall

h = Convective heat transfer coefficient

h_{fg} = Latent heat of vaporization

H_{RC} = Rockwell C scale hardness value

H_V = Vickers scale hardness value

K = Thermal conductivity

K_0 = Bessel function of the second kind, zero order

k_l = Surface transmission coefficient

L = Length of molten pool

L_b= Beam-powder interaction distance

$\lambda = \frac{K}{\rho C_p}$

$m = \frac{2*k_l}{g*K}$

$\dot{m}$ = Powder flow rate at nozzle

M = Conduction mitigation factor

μ_s = Measured cross section mean particle diameter

μ_t = True mean particle diameter

P_0 = Initial supplied laser power

P_1 = Power absorbed into work piece

P_{ap1} = Power absorbed by the powder that is deposited into the molten pool

P_{ap2} = Power absorbed by the powder that is **not** deposited into the molten pool

P_{rp1} = Power reflected by the powder that is deposited into the molten pool

P_{rp2} = Power reflected by the powder that is **not** deposited into the melt pool

π = Ratio of a circle's circumference to its diameter

Q_1 = Energy conducted into the work piece

Q_2 = Energy convected away from the molten pool

Q_3 = Energy radiated away from the molten pool

Q_4 = Energy evaporated away from the molten pool

Q_l = Total energy lost

Q_p = Energy provided to the work piece

R = Radial distance from the origin

r = Radius of powder

ρ = Density of material system

σ = Boltzmann's constant

σ_s = Measured cross-section standard deviation of particle diameter

σ_t= True standard deviation of particle diameter

T = Temperature

T_0 = Ambient/initial temperature

T_{peak} = Peak temperature

T_{mean} = Mean temperature

v = Velocity of deposition head

v_p = Exit velocity of powder from nozzle

ΔW = Change in weight of the sample

x = Direction co-linear to the deposition trajectory

y = Direction parallel to the surface of the substrate, and perpendicular to x

z = Direction perpendicular to the surface of the substrate

ζ = Quasi-steady state z value relative to a moving origin

I. INTRODUCTION

Since the very first use of a hammer and chisel in ancient times all large scale manufacturing has been subtractive, wherein a desired component is extracted from an existing block of material by removing the extraneous material around the component. Subtractive processes have been the primary mode of manufacturing over millennia, until the recent advent of additive manufacturing. In additive manufacturing, material is created by systematically compounding and fusing layers of an input material. The additive nature of the process allows for three primary advantages beyond the capabilities of subtractive manufacturing.

The first advantage is the enhanced material and time efficiencies that result from the absence of slowly machining off large amounts of waste material. This is particularly advantageous for solid parts with complex geometry. Secondly, additive manufacturing allows for the fabrication of geometries in components that are not possible with traditional subtractive machining. Complex geometric capabilities can be exploited to reduce final component weight while maintaining performance integrity. The third advantage is the ability to tailor the processing parameters to yield components with properties designed for the application. The processing parameters can be changed to optimize for hardness, ductility, heat transfer properties, and even the creation of functionally graded materials that do not contain detrimental material interfaces, such as welds or fixturing. There are two general large scale additive manufacturing techniques for producing structural parts, direct metal deposition (DMD) and selective laser sintering (SLS). There are two further subsets of DMD, the wire-fed and powder-fed methods. This research will focus on the powder-fed type of DMD.

DMD has great potential for making an impact because designs that were not previously able to be manufactured can now be fabricated in high strength metals. However, the DMD process has been largely based on trial and error fabrication tests rather than an understanding of the thermal history within the part. Understanding the dynamic temperature distribution during DMD is an important step towards improving properties because the thermal hysteresis is the

primary influence on the final microstructure, which determines the ultimate mechanical performance of the component.

The complexity of DMD processes and the extremely small time and length scales that are associated with DMD make modeling of the process very challenging. While studies have been conducted using numerical, analytical, and experimental techniques to understand the thermal distributions in the vicinity of the laser, very little work has worked to effectively merge all three of the investigation techniques. Without validation of predictive models, it is not possible to fully utilize the potential of DMD. This study aims to be able to compare analytical and numerical predictions of the temperature distribution in DMD with experimental results to gain a better understanding of the thermal processes that occur during DMD.

II. LENS™ MR-7 SYSTEM

The DMD-type machine used in this study is the LENS MR-7™, which is Optomec Incorporated's (Albuquerque, NM) research-and-development specific DMD machine. The fabrication of parts for this study was done at Optomec's Albuquerque office on the original MR-7 prototype. Although in a slightly different configuration compared to the production machine, the prototype MR-7 has the same major components as the production version that was recently purchased by Los Alamos National Laboratory. The MR-7 is powered by a class IV, 1 kilowatt IPG fiber laser that is directed into a class I laser enclosure through fiber optic cables.

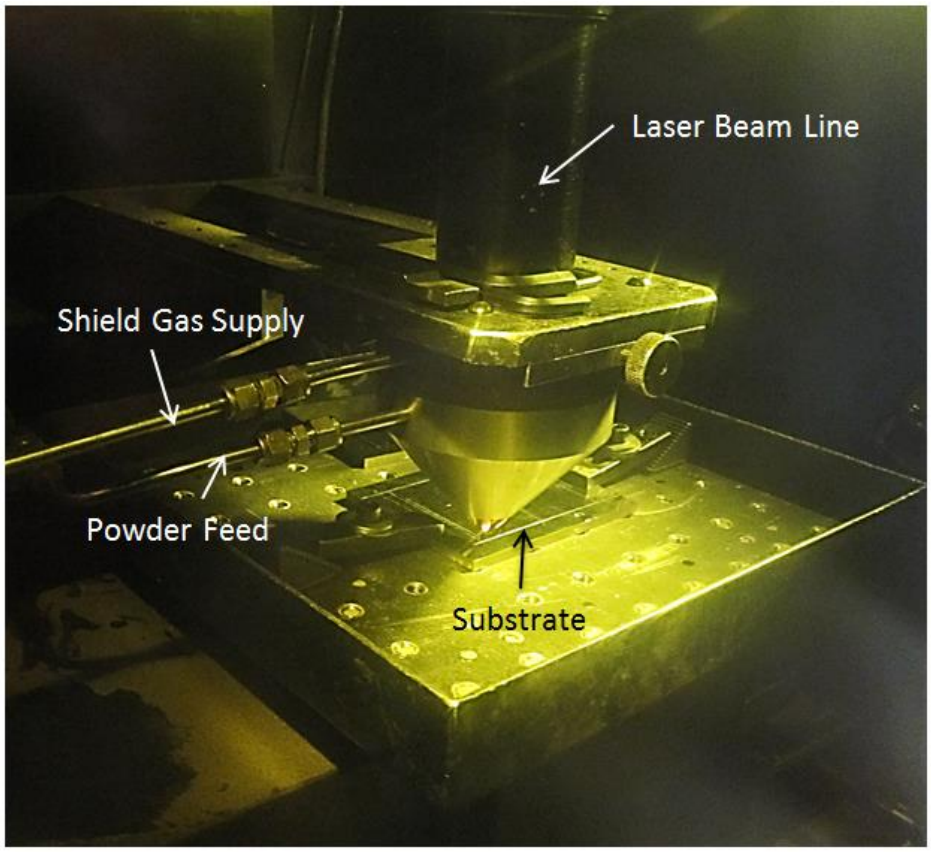

Figure 1: LENS MR-7™ in operation

The enclosure is hermetically sealed with glove ports in the front and with a ~1 ft^3 working volume in the center of the chamber. On the side of the enclosure is an anti-chamber for

passing substrates, tools, and data acquisition systems into the glovebox. The glovebox is maintained at a slightly positive pressure of argon to minimize oxygen contamination of the powders. In order for a deposition to be performed, a substrate onto which the material is deposited must be fixed to the worktable via set screws and clamps. The powder hoppers are then loaded with a powder that has appropriate flow characteristics. Optomec recommends a spherical powder with a nominal size of ~100 μm. The flow of the powder into the deposition head is performed by placing the powder inside the hopper and flowing argon into the powder bed to create an aerosol that then flows towards the outlet near the laser.

Prior to deposition, the path of the deposition head is set using the computer numerical control system, and the powder flow is turned on. Once a stable powder flow is achieved and the deposition head is in place, the laser is turned on and deposition begins.

A subtle detail occurs at this point that influences the regime of deposition; the laser pauses for a fraction of a second prior to the deposition. This pause is intentionally done in order to initiate a molten pool of metal in the substrate into which powder is then deposited.

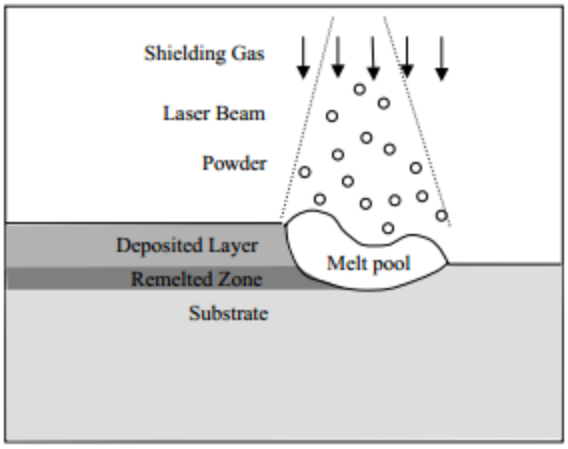

Figure 2: Cross section of the laser-initiated melt pool and injection of powder (1)

DMD is inherently different than the powder bed technology used in other additive manufacturing processes such as selective laser sintering. In these processes, the laser imparts its power into the powder bed where the particles either melt or rapidly sinter in the solid state.

Conversely in DMD, the laser power is used to liquefy the substrate before being impacted by ambient temperature powder, which then rapidly solidifies in the molten pool left in the wake of the laser. The difference, while subtle, can lead to significantly different final products. When selective laser sintering does not induce full melting, it can leave closed porosity within the part. DMD induces full melting and therefore produces fully dense components. However if the processing parameters are not carefully controlled to affect the molten pool and the resulting solidification front, it can produce very rough surface finishes on components (2). Thus, both processes have their own strengths and weaknesses.

III. LITERATURE REVIEW

The first DMD type process was invented at Los Alamos National Laboratory and was named directed light fabrication (DLF) (3). Early papers that introduced DLF simply described how the machine was put together and how the DLF operated. In addition, a simple one-dimensional heat flow model was developed (3). This model was supplemented by the experimental measurement of liquid cooling rates within the molten zone by measuring the secondary dendrite arm spacing in as-deposited AISI 316 stainless steel and in an iron - 25% nickel alloy (3). The cooling rates were calculated using known empirical relationships between the measured dendrite arm spacing and cooling rate. After this initial discovery 20 years ago, there was relatively little research conducted on DMD in the US until about 10 years ago. There are now active programs at the University of Michigan, Lehigh University, Ohio State University, and Pennsylvania State University (4) (5) (6).

The three methods that have been used to study DMD are analytical modeling, numerical predictions, and experimental results. Each have their specific strengths and weaknesses, which are reviewed in the following sections.

Numerical Simulations

The state-of-the-art in published numerical simulations invokes assumptions that significantly simplify the process by removing dynamics. This reduces the heat transfer to a simpler quasi-steady state problem which is then solved using the finite element method. However in the last few years, newer numerical models that are dynamic at the mesoscale, such as those developed for weld modeling, have been applied to DMD. While the heat transfer and thermo-mechanical processes involved in this kind of simulation are well established, these models do not account for the addition of material during the process. In DMD, powder is injected into the molten pool and this introduction of material creates significant complications for numerical simulation. The difficulty compounds when building up multiple layers to create a

structure, such as would be needed for useful manufacturing of objects with complex shapes. The difficulty is such that even relatively simple geometries, such as a one dimensional wall resulting from the stacking of successive depositions takes multiple weeks to run on codes such as SysWeld™ (ESI Group, Paris, France), Abaqus™ (Dassault Systemes, Vélizy-Villacoublay, France), and Comsol™ (Comsol Incorporated, Los Angeles, California, USA).

The numerical modeling of additive manufacturing has been largely based on the modeling of laser cladding process, because for single pass simulations they are nearly identical. Since the early 1990's Mazumder and colleagues (2) (6) , at the Center of Laser Aided Materials Processing Center (University of Michigan, Ann-Arbor, Michigan) have published numerous papers on the numerical modeling of laser cladding and additive manufacturing. The vast majority of these numerical simulations have been done using self-developed highly specialized codes. However for success in the modeling of additive processes such as DMD, the numerical simulation capability must be available in commercial codes. For this reason, the research conducted for this thesis utilizes ESI Group's SysWeld™ commercial multi-physics code.

Analytical Modeling

Analytical models can, in principle, be used to predict both qualitative and quantitative trends in how processing parameters influence the microstructure and properties of the deposit resulting from DMD. However the large number of input parameters, variables, and assumptions required for an accurate analytical model is extremely challenging and thus usually only parts of the problem can be addressed analytically. There has been work done in the analytical characterization of the various portions of the DMD process by Peyre *et al.* (7), Labudovic *et al.* (8), Madigan (9), and Pinkerton (10). These sub-process analytical solutions are unique in that they are multi-physics based, and are not simply curve fits of experimental data. While both of these techniques are useful in manufacturing parts, the refinement of the analytical models is the true progression of physics-based knowledge of the process.

Many of the analytical models focus on the dimensions of deposited material, meaning that the focus is on geometry, rather than temperature transients. While geometry is very important, a more direct way to determine the projected performance of a manufactured component is to know its thermal history. Thermal history has a significant impact on microstructure morphology, which in turn determines the mechanical performance of materials. Therefore in order to better understand how a DMD-produced component will perform, this research targets the temperature history of the component to better understand the process, and its effect on the final component.

Experimental Results

By far the largest body of work exists in the experimental analysis of additive manufacturing. For the most part, this involves fabricating simple components and subsequent sectioning and *post-mortem* examination. These studies provide useful information about the process such as the diameter and depth of penetration of the molten zone, the dimensions of the heat affected zone, the amount of closed porosity in the structure, layer height, grain size, and mechanical properties. These parameters are then used to show the relationships between processing variables and microstructure for a given geometry and material system. Research of this type has been done dating back to 1995 beginning with Lewis *et al.* (11), and progressing with Mazumder *et al.* (2) , Unocic *et al.* (5), Battacharya *et al.* (12), and Kumar *et al.* (13).

The first experimental data obtained from a DMD type process was from the inventors of the DLF technique. Lewis *et al.* (11) obtained the liquid-state cooling rates for DLF process from the measurement of secondary dendrite arm spacing. The observed liquid cooling rates were extremely rapid, ranging from 100 $\frac{^{o}\mathrm{C}}{\mathrm{second}}$ to $10^{4}\,\frac{^{o}\mathrm{C}}{\mathrm{second}}$. Similarly high cooling rates are used in bulk rapid solidification process for the production of amorphous alloys. Subsequent research from Hochanadel *et al.* (14) from Los Alamos National Laboratory involved the testing of bulk mechanical properties of AISI 316 stainless steel components produced by the DLF technology as compared to conventional subtractive production techniques. The measured

ultimate tensile strength approached that of wrought tensile specimens, but exhibited a ~20% lower strain-to-failure.

In the 1990's, research on DMD-type machines began at academic institutions. Research from Mazumder *et al.* (2) detailed data obtained from DMD experiments using H13 tool steel. This publication was one of the first to carry out a production-type study on a given material system. The research correlates raw processing parameters to final microstructure, cooling rates, and deposition dimensions. The cooling rates are determined using secondary dendrite arm spacing of the deposited H13 tool steel. The techniques are similar to the work done by Lewis *et al.* (11) at Los Alamos National Laboratory. Beyond the experimental observation of liquid-state cooling rate, the research showed correlation between deposition dimensions and processing parameters. However, the relations shown were purely empirical, rather than being physics based.

Beyond purely empirical relationships, more precise measurements of efficiency in the DMD processes were needed. The research done by Unocic *et al.* (5) quantified the three main efficiency losses associated with DMD, the laser energy transfer, melting efficiency, and deposition efficiency. The laser transfer efficiency did have a slight dependence on laser power, but was nominally around 40%. This dependence is to be expected because of the dependence on the optical properties of the roughened substrate. The melting efficiency is the amount of energy absorbed by the work piece that is used to maintain a stable melt pool on the substrate. It was measured by examining the melt dilution in the cross section of the deposition. The melt dilution is a term that comes from welding metallurgy and is defined as (4):

$$\text{Dilution} = \frac{A_S}{A_s + A_{fm}} \qquad \text{Eq. 1}$$

A_S = Cross sectional area of melted substrate $\quad A_{fm}$ = Cross sectional area of melted filler metal

There was a positive correlation between power supplied and the melting efficiency that reached a maximum at 33%. However the melting efficiency began to decrease as the maximum power of the system was approached. The third parameter measured was how efficiently the powder is used in the process. In general, the DMD process is inefficient in powder use unless optimized. The observed powder use in the experiment ranged from near zero to 14%.

More recent experimental data and analysis comes from Kumar *et al.* (13) and Jang *et al.* (15), and are very similar in their approach to the characterization of a DMD-type process. Both of these publications present a dimensionless regression analysis of experimental data. They developed an algorithm that can predictively model the dimensions of depositions for a given material from *post-mortem* test analysis. While these regression analytics are accurate inside the operational window for which they are intended, they offer little in the understanding of the multi-physics of DMD, and cannot be applied if the material system is changed.

While there has been significant research in analytical and numerical modeling and experiments of DMD, there has been very limited work done in trying to tie all three methods together. Each of these methods has their own distinct advantages. However, the congruence of all three methods provides the only way to validate existing numerical models. These numerical models can then be used to develop realistic and predictive analytical models. The purpose of this research is to attain a better understanding of the process by using experimental results, numerical simulations, and an analytical model to study DMD.

IV. METHODOLOGY

Analytical Model Derivation

Direct metal deposition has many similarities with multi-pass welding, which has been around since the advent of arc welding in the late 19th century. Significant differences between the two are that the nature of the heat source and how material is introduced into the molten zone. Nevertheless, in the beginning of an investigation of heat flow in DMD, the logical place to start is by reviewing of existing analytical models of welding, and the relevant temperature distribution equations.

The first work done on analytical temperature distributions resulting from moving heat sources was done by Daniel Rosenthal and focused on arc welding (16). While the analytical solutions were intended to apply to arc welding, they apply even better to laser welding because the power transients that exists in arc welding does not exist in laser processes. There are two equations that can be utilized as the bounding analytical solutions for the two extreme solutions of the deposition, a semi-infinite plate and plate of finite thickness. The two relevant equations from Rosenthal's work are summarized below.

THREE DIMENSIONAL CONDUCTION IN A SEMI-INFINITE PLATE

In this model a point source representation of heat input is moving through a semi-infinite medium at a fixed speed. This model is a reasonable initial approximation for a single pass deposit onto a large substrate because the thermal affects under these circumstances do not extend beyond the first millimeter of the plate. Therefore, as far as thermal length scales, this substrate can be considered semi-infinite.

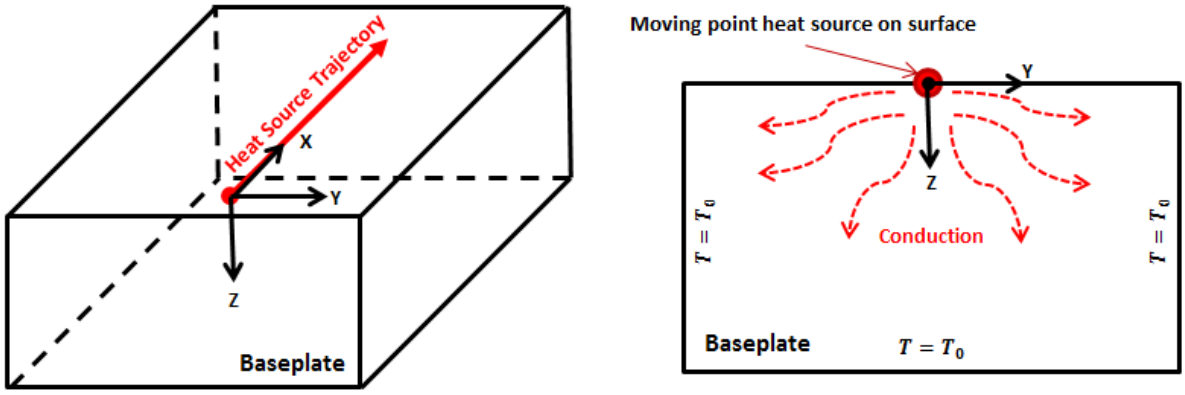

Figure 3: Schematic for 3D conduction in an semi-infinite plate from a moving point source

The assumptions for the analytical solution for the temperature distribution in a plate of finite thickness are:

1. **Heat conducts evenly in all directions in the material:**

$$R = \sqrt{\xi^2 + y^2 + z^2} \qquad \text{Eq. 2}$$

where : $\xi = x - vt$

R = Radial distance from the origin

x = Direction co-linear to the deposition trajectory

y = Direction parallel to the surface of the substrate, and perpendicular to x

z = Direction perpendicular to the surface of the substrate

ζ = Quasi-steady state z value relative to a moving origin

2. **No heat lost from the work piece to the surroundings:**

$$\frac{dT}{dz} = 0 \text{ for } z = 0 \text{ and } R \neq 0 \qquad \text{Eq. 3}$$

T = Temperature

T_0 = Ambient/initial temperature

3. Temperature at large radius R is unchanged:

$$\lim_{R\to\infty} T(x,y,z) = T_0 \qquad \text{Eq. 4}$$

Under these conditions, the analytical solution for the temperate at any point (x,y,z) is as follows (16):

$$T(x,y,z) = T_0 + \frac{Q_P}{2\pi K} e^{-\lambda v x} \frac{e^{-\lambda v R}}{R} \qquad \text{Eq. 5}$$

$$R = \sqrt{\xi^2 + y^2 + z^2}$$

K = Thermal conductivity

$\lambda = \frac{K}{\rho C_p}$

Q_p = Energy provided to the work piece

T = Temperature

T_0 = Ambient/initial temperature

v = Velocity of deposition head

TWO DIMENSIONAL CONDUCTION IN A PLATE OF FINITE THICKNESS

The second applicable analytical model by Rosenthal (16) is for a line heat source in a plate of finite-thickness. While the link between through-thickness welding and DMD is not inherently obvious, this analytical model can be modified to reflect depositions where multiple passes are overwritten to form a wall. A schematic showing Rosenthal's original applicable geometry is shown in Fig. 4.

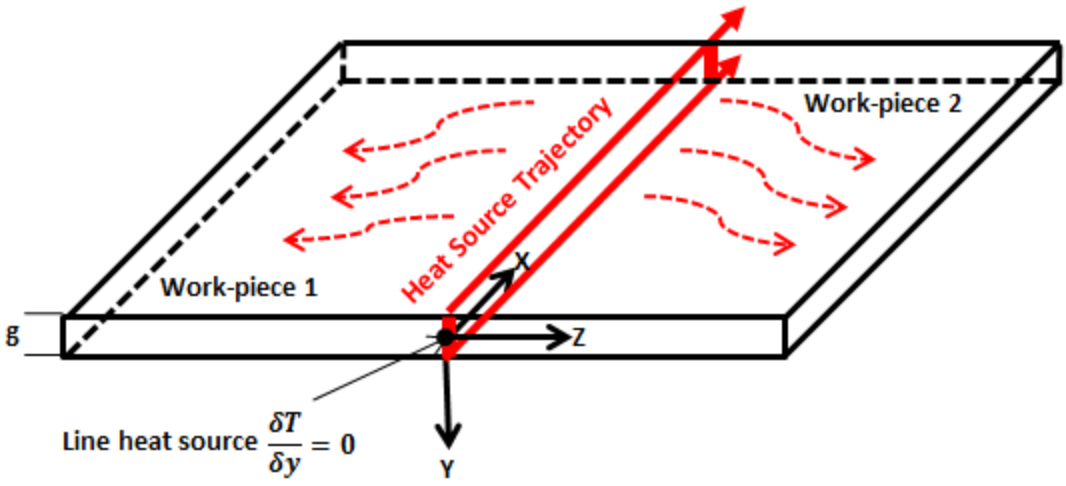

Figure 4: Schematic for 2D conduction in a plate of finite thickness *g* from a moving line source

The assumptions and boundary conditions to solve this problem analytically are:

1. **No temperature gradient through the thickness of the work piece:**

$$\frac{\delta T}{\delta y} = 0 \qquad \text{Eq. 6}$$

2. **Heat conducts uniformly in the x and y direction and tends toward Q_P as R approaches zero:**

$$\lim_{R \to 0} -2\pi R g K \frac{\delta T}{\delta R} = Q_P \qquad \text{Eq. 7}$$

g = Finite wall thickness

K = Thermal conductivity

Q_p = Energy provided to the work piece

R = Radial distance from the origin

T = Temperature

3. **At infinite length the temperature remains at the initial temperature**

$$\lim_{R\to\infty} T(x,y) = T_0 \qquad \text{Eq. 8}$$

Under these conditions, the analytical solution for the temperate at any point (x,y,z) is (16):

$$T(x,y) = T_0 + \frac{Q_P}{2\pi K} e^{-\lambda \nu x} \frac{K_0(\sqrt{\lambda \nu^2 + m} \times R)}{g} \qquad \text{Eq. 9}$$

g = Finite wall thickness

K = Thermal conductivity

K_0 = Bessel function of the second kind, zero order

$\lambda = \frac{K}{\rho C_p}$

$m = \frac{2 * k_l}{g * K}$

Q_p = Energy provided to the work piece

π = Ratio of a circle's circumference to its diameter

T = Temperature

T_0 = Ambient/initial temperature

v = Velocity of deposition head

PINKERTON MODEL FOR POWER LOSSES

It is clear that these models do not incorporate all of the physics necessary to describe DMD processes. One of the primary modifications necessary to link the model to DMD is the fact that the heat input in DMD is from a laser, which is highly influenced by the optics and absorption characteristics of the base metal, powder, and melt pool. Modeling of these optics effects is fairly new due to the fact that it is unique to DMD processes. One approach uses Pinkerton *et al's*. (10) analytical solution and a series approximation to solve for power efficiencies in DMD processes. The assumptions for this model are:

1. Laser power is uniform inside the spot diameter
2. Powder is fed parallel to the laser and interacts with the laser only over the distance between the nozzle and the work piece
3. The melt pool is equal to the diameter of the laser spot size
4. The melt pool is a sphere with hemispherical caps
5. Powder particles are ideal spheres
6. Absorptivity is independent of time in the laser (i.e. independent of temperature)
7. Particle shadowing is negligible
8. There is no heat loss from the particles due to convection or radiation during their time of flight
9. Powder that strikes the melt pool is absorbed into then melt pool

With these assumptions, the following relationships for the energy balances were derived by Pinkerton *et al*. (10)

Power absorbed by the powder that is deposited into the melt pool P_{ap1}

$$P_{ap1} = \frac{3a_p \dot{m} D_1 L_b P_0}{\pi r v_p \rho D_0^3} \qquad \text{Eq. 10}$$

a_p = Absorptivity of powder

D_0 = Initial beam diameter

D_1 = Beam diameter at surface

L_b= Beam-powder interaction distance

$\dot{m}$ = Powder flow rate at nozzle

r = Radius of powder particle

ρ = Density of material system

v_p = Exit velocity of powder from nozzle

P_0 = Initial supplied laser power

π = Ratio of a circle's circumference to its diameter

Power reflected by the powder that is deposited into the melt pool P_{rp1}

$$P_{rp1} = \frac{3(1 - a_p)\dot{m}D_1 L_b P_0}{\pi r v_p \rho D_0^3} \quad \text{Eq. 11}$$

Power absorbed by the powder that is **not** deposited into the melt pool P_{ap2}

$$P_{ap2} = \frac{3a_p\dot{m}(D_0 - D_1)L_b P_0}{\pi r v_p \rho D_0^3} \quad \text{Eq. 12}$$

Power reflected by the powder that is **not** deposited into the melt pool P_{rp2}

$$P_{rp2} = \frac{3(1 - a_p)\dot{m}(D_0 - D_1)L_b P_0}{\pi r v_p \rho D_0^3} \quad \text{Eq. 13}$$

Of these terms only the energy from P_{ap1} goes into the work piece and factors in to the enthalpy contributed to the melt pool. This corresponds to P_1. The rest of the energy is lost to reflection from either the powder or substrate.

$$P_1 = a_s\left(P_0 - P_{ap1} - P_{ap2} - P_{rp1} - P_{rp2}\right) + P_{ap1} \quad \text{Eq. 14}$$

a_s = Absorptivity of powder

P_0 = Initial supplied laser power

P_1 = Power absorbed into substrate

P_{ap1} = Power absorbed by the powder that is deposited into the molten pool

P_{ap2} = Power absorbed by the powder that is **not** deposited into the molten pool

P_{rp1} = Power reflected by the powder that is deposited into the molten pool

P_{rp2} = Power reflected by the powder that is **not** deposited into the melt pool

Next the energy radiated, convected, and evaporated away from the melt pool, as well as energy conducted from the melt pool into the work piece must be calculated. First the peak and mean temperatures are determined

$$T_{Peak} = \frac{P_1}{4\pi D_1} + T_0 \quad \text{Eq. 15}$$

$$T_{Mean} = \frac{T_{Peak} + T_M}{2} \quad \text{Eq. 16}$$

Next the heat conducted into the work piece (Q_1), convected away from the weld pool (Q_2), and the heat radiated away from the surface of the weld pool can be determined (Q_3).

$$Q_1 = \frac{\pi k B D_1^2}{2}(T_{Peak} - T_0) + \frac{\pi k B L D_1}{2}(T_{Mean} - T_0) \quad \text{Eq. 17}$$

$$Q_2 = \frac{\pi h D_1^2}{2}(T_{Peak} - T_0) + \frac{\pi h L D_1}{2}(T_{Mean} - T_0) \quad \text{Eq. 18}$$

$$Q_3 = \frac{\pi\varepsilon\sigma D_1^2}{2}(T_{Peak}^4 - T_0^4) + \frac{\pi\varepsilon\sigma D_1}{2}(T_{Mean}^4 - T_0^4) \quad \text{Eq. 19}$$

B = Molten pool conduction calibration constant

D_1 = Beam diameter at surface

ε = Emissivity of molten pool

h = Convective heat transfer coefficient

K = Thermal conductivity

L = Length of molten pool

Q_1 = Energy conducted into the work piece

Q_2 = Energy convected away from the molten pool

Q_3 = Energy radiated away from the molten pool

σ = Boltzmann's constant

T_0 = Ambient/initial temperature

T_{peak} = Peak temperature

The energy evaporated away from the surface Q_4 is slightly more complicated and requires incorporation of the 'overall evaporation' model by Choi *et al.* (17). The resulting equation from the 'overall evaporation' model for the energy evaporated from the melt pool is:

$$Q_4 = 28295\pi h_{fg} D_1^2 \left(\frac{e^{-18836/T_{Peak}}}{\sqrt{T_{Peak}}}\right) + 28295\pi h_{fg} D_1 L \left(\frac{\sqrt{2}e^{-37672/(T_{Peak}+T_m)}}{\sqrt{T_{Peak}+T_m}}\right) \quad \text{Eq. 20}$$

D_1 = Beam diameter at surface

h_{fg} = Latent heat of vaporization

L = Length of molten pool

Q_4 = Energy evaporated away from the molten pool

T_{peak} = Peak temperature

T_{mean} = Mean temperature

Under these conditions, the power lost Q_l is equal to the sum of the calculated Q values:

$$Q_l = Q_1 + Q_2 + Q_3 + Q_4 \quad \text{Eq. 21}$$

Therefore the Q_P in the Rosenthal equations for conduction is equal to the power supplied by the laser Q_S, less the total power lost due to the four loss modes Q_l.

$$Q_P = P_0 - Q_l \quad \text{Eq. 22}$$

P_0 = Initial supplied laser power Q_p = Energy provided to the substrate

Q_l = Total energy lost

At this point we now have a fully coupled analytical equation for temperature distribution in two regimes of laser welding. However, DMD differs from laser welding, because the enthalpy and mass that is introduced by the powder must be accounted for, in addition to the subtle differences in geometry.

MODIFICATIONS FOR DMD

In order to accurately analytical model DMD, modifications to the conduction pathways are necessary for both the semi-infinite plate and finite-thickness plate deposition models.

In the case of the semi-infinite plate, the point source is not an accurate representation of the heat source in DMD. In DMD, the supplied heat source is a slightly defocused laser, which is similar to a circular (Diameter ≈ 0.7mm) moving heat source. To account for the distinctions between heat source geometries, the penetration of heat supplied from the laser is mitigated. This mitigation factor M is introduced into Equation 1.

$$R = \sqrt{\xi^2 + y^2 + (Mz)^2} \qquad \text{Eq. 23}$$

The mitigation factor is measured by the examination of the aspect ratio of the cross section of the fusion zone in the Y and Z directions relative to the centerline, where:

$$M = \frac{d_{Y-Fusion}}{d_{Z-Fusion}} \qquad \text{Eq. 24}$$

While a typical value for M obtained from experiments is 2, it can vary from between 1.8 and 2.4.

For the case of a plate with finite thickness, the original analytical solution by Rosenthal is applied to the process of through thickness welding, wherein heat is conducted away from the fusion zone by the two work pieces being joined together. In the case of DMD, the heat conduction is only through the single wall of pre-deposited material. Therefore the heat flux in the DMD process has only half that of the conduction assumed for welding. The modification to the finite thickness plate model limits the degrees of freedom of the conduction to only the positive z direction. Since convection away from the surface is addressed in Pinkerton's solution, we can assume that there is a 200% increase in heat flux for DMD relative to through thickness welding. This modification results in a temperature distribution given by

$$T(x,y) = T_0 + \mathbf{2}\left[\frac{Q_P}{2\pi K} e^{-\lambda \nu x} \frac{K_0(\sqrt{\lambda \nu^2 + m} \times R)}{g}\right] \qquad \text{Eq. 25}$$

With these modifications to the Pinkerton-Rosenthal analytical solution, an accurate analytical solution of temperature distribution inside DMD should be possible.

Analytical Model

The analytical model was used in two ways to characterize single pass the DMD. The model was used to both calculate the cooling rate at a fixed point and the peak temperature as a function of R for given input parameters. Each of the two solutions were implemented in MATLAB (MathWorks, Natick, MA, USA*)(Shown in Appendix III)*.

The cooling rate portion of the code was written first and requires the user to designate a query point for which to obtain a temperature transient. To obtain the solution to a temperature transient calculation, the following are required:

1. Define all necessary physical constants and input parameters
2. Calculate the time to deposit by diving the length of the deposit by velocity of the deposition head
3. Create a one-dimensional time array with a small time step (0.1 seconds was used in this calculation) that covers from time zero to the total calculated deposit time
4. Calculate the number of elements inside the time array for use later in a calculation loop
5. Create the ζ array by subtracting the product of the deposition head velocity and the time array from the set x-location of your query point. The ζ value calculation allows for the use of a quasi-steady state solution by moving the origin as a function of time
6. Calculate a time dependent R array using Equation 23
7. Calculate the initial Pinkerton power loss terms $P_{ap1,}$ P_{ap2}, P_{rp1}, P_{rp2},
8. Subtract losses due to laser-powder interaction from the initial laser output and use that as the total power input for the rest of the calculation
9. Calculate the T_{peak} and T_{mean} according to Equations 15 and 16

10. Calculation of the Rosenthal's four Q values Q_1, Q_2, Q_3, and Q_4, according to Equations 17-20
11. The sum of Q_1, Q_2, Q_3, and Q_4, should equal the total power absorbed into the substrate. This step does not affect the power applied to the substrate, but it does show the relative amounts of energy that are dissipated though the four modes of cooling considered in this model
12. Calculation of the temperature distribution as a function of time using either the semi-infinite plate model *(Equation 5)* or the finite thickness model (Equation 25).
13. As a supplement, the peak temperature as a function of position can be calculated by creating an array of locations for x or y. Then running a loop that will re-calculate the array R (which is a function of ζ and either x or y) and the temperature distribution for the corresponding x value according Equation 5 or 25.
14. After each loop, the maximum value of the temperature transient array is taken and stored in a peak temperature array that corresponds to the x (or y) array value it was calculated for. When the peak temperature array is plotted against the user defined x(or y) array, the peak temperature as a function of position can be determined.

The first data that was obtained was the cooling transient. The temperature distribution in Fig. 5 is for the deposition conditions in test 2 for a set of points at x=8.2 mm z = 0.00 and y varying from 0.5 mm to 5.0 mm.

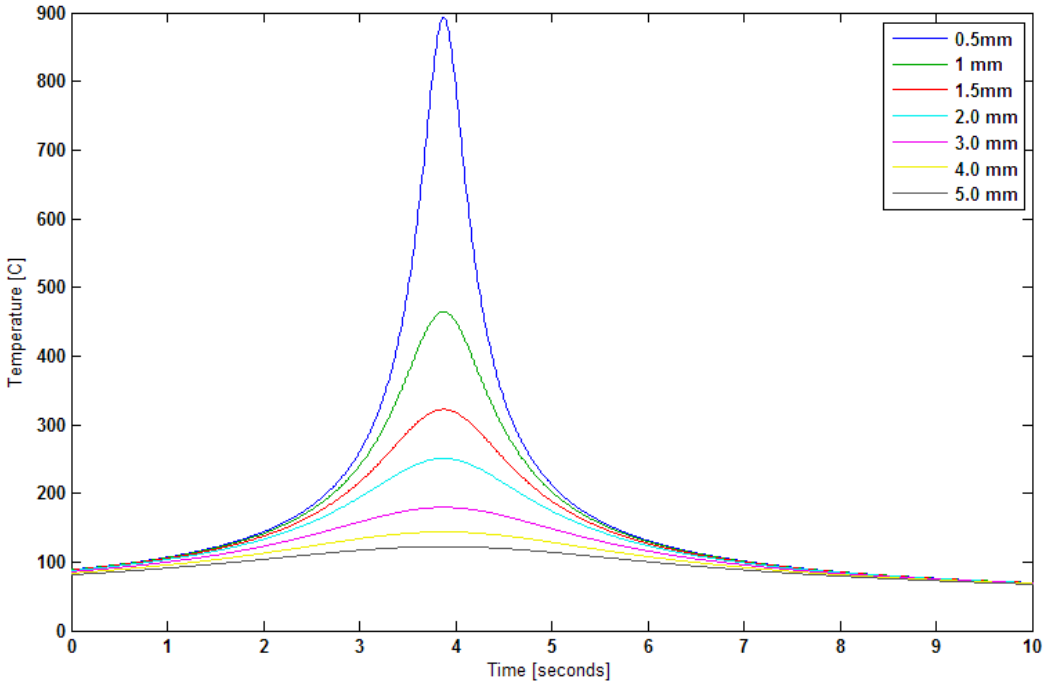

Figure 5: Analytical solution for temperature transient for the deposition conditions in test 2 (defined in experimental section) for a set of points at x=8.2 mm z = 0.00 and y varying from 0.5 mm to 5.0 mm.

The second portion of the analytical solution is to find peak temperatures as a function of distance from the heat source. This solution is used to determine the temperature distribution as a function of time at each location and extracts the maximum. The radius is subsequently increased in small increments and the maximum is calculated for each to create a continuous distribution of peak temperatures as a function of radial distance from the source. This data is shown below in Fig. 6 is for the second test series deposition conditions.

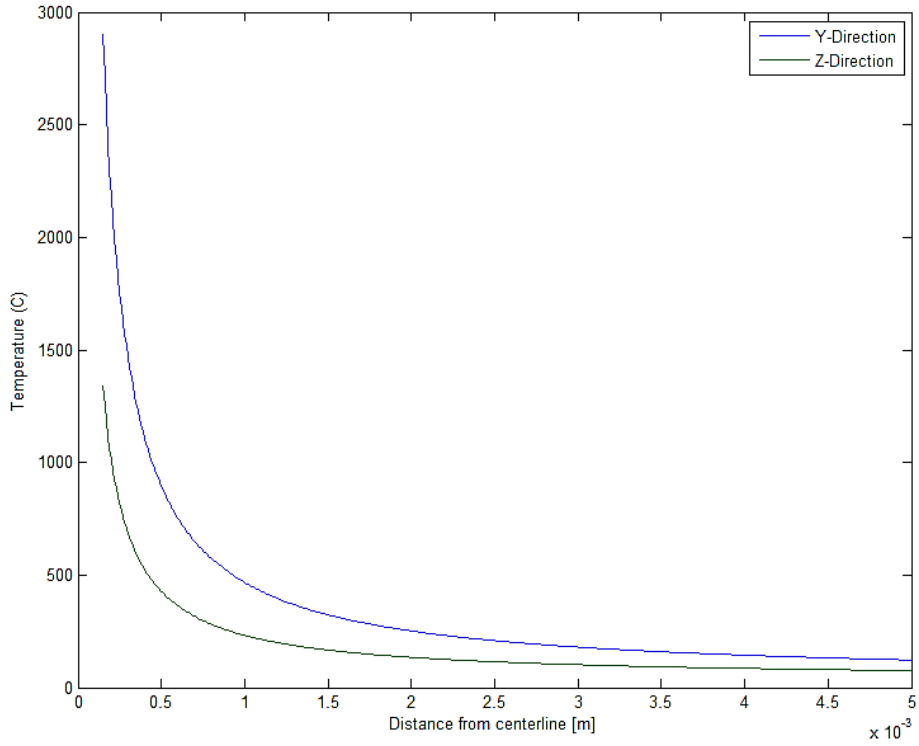

Figure 6: Analytical solution for peak temperature as a function of position in the Y and Z directions for the deposition conditions in test 2 (defined in experimental section).

The peak temperature distribution is directly applicable to examining the heat affected zones in the single pass depositions.

Numerical Model

The SysWeld™ (ESI Group, Paris, France) code was used to model a single pass. There are many advantages to numerical modeling, one of which is the ability to use temperature-dependent properties of materials. This feature is very advantageous for processes where a wide temperature range is studied; such is the case with DMD. With peak temperatures surpassing 2000ºC, the properties of the high temperature metal and the room temperature peripheral portions of the substrate will be vastly different. The disadvantage is that numerical models of complex processes such as these are very time consuming. However if only a single pass is

studied, and the shape is idealized, the calculation time on a single processor can be decreased to around 48 hours.

The mesh used for the study on a single pass line is a square 1 mm × 1 mm deposition on top off a ¼ inch thickness substrate. It uses a hexagonal meshing scheme and comprises 268,000 unit cells. Fig. 7 shows the macro view of the meshed component.

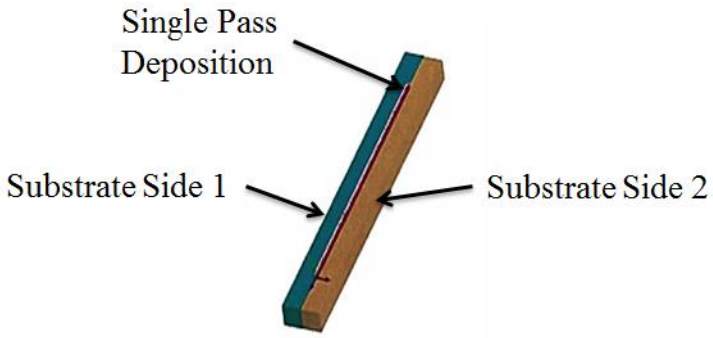

Figure 7: Full geometry for DMD SysWeld numerical simulation

Zones of high heat flux and thermal gradients require finer cell sizes to retain accuracy. In order to be computationally efficient, the mesh becomes much coarser towards the edges of the simulated substrate, away from areas of high thermal gradients.

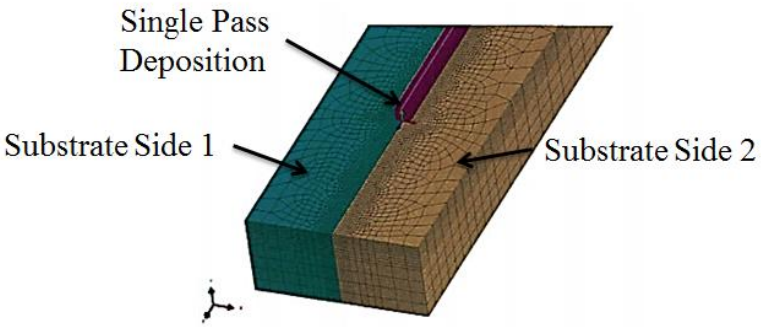

Figure 8: Detail view of cell size in meshed components

The SysWeld code has the capability to use thermal and mechanical solvers to model complete thermo-mechanical response of components. However the scope of this research does not take into account mechanical response of the material. Below are the modeled temperature dependent properties of AISI 1018 steel. The properties are modified from those listed for low carbon steels similar to 1018 from Touloukian *et al.* (18) (19) (20) (21).

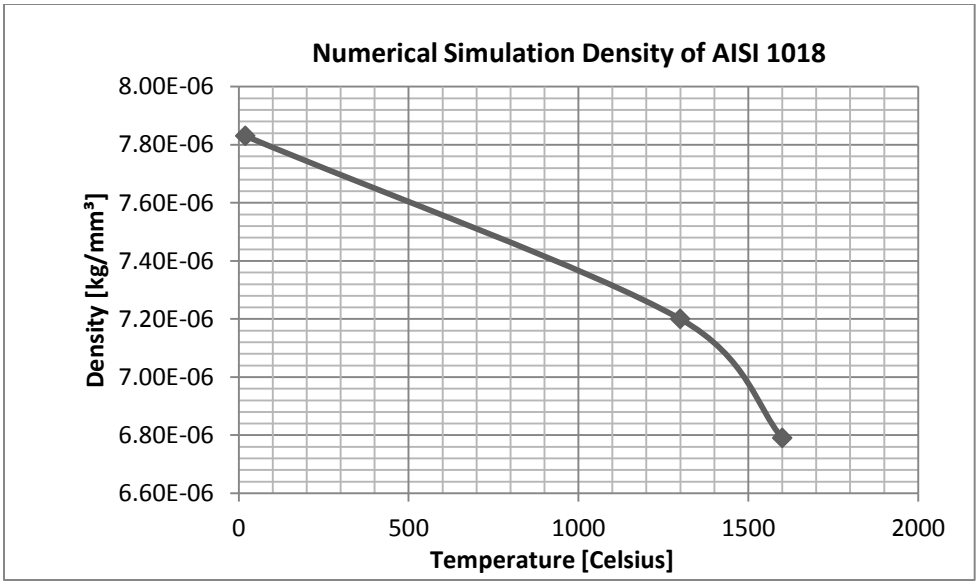

Figure 9: Density of AISI 1018 used for numerical modeling

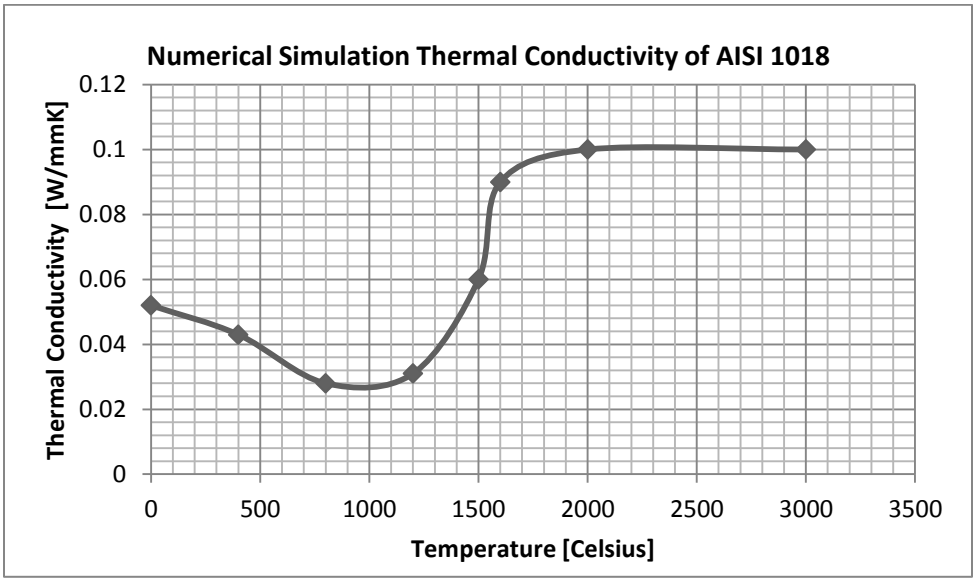

Figure 10: Thermal conductivity of AISI 1018 used for numerical modeling

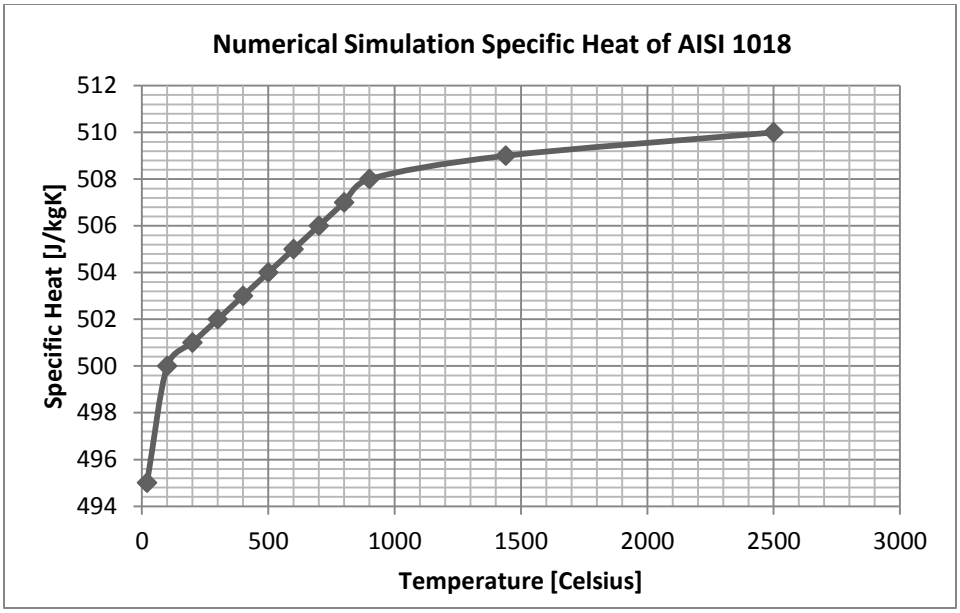

Figure 11: Specific heat of AISI 1018 used for numerical modeling

After the approximate 48 hour run time, the results of the SysWeld code were post processed and iterated. Even in the numerical model there are certain parameters that must be modified for each process. The most sensitive is the thermal conductivity values of the material. The fine grain material in the deposit will have a slightly lower thermal conductivity than the more large grained material in the substrate. The mitigation of the thermal conductivity in the deposit is accomplished by a multiplication factor of 0.7 being applied to the material in the deposition component prior to the simulation. The 0.7 factor comes from a convention used by Dr. Chen at Los Alamos National Laboratory; it has been proven accurate on previous welding projects that were modeled with SysWeld.

Due to time constraints on the machine licensed to run SysWeld, only one of the tests could be modeled. The test parameters modeled were for test two with the following conditions:

Table 1: Conditions for SysWeld numerical model

Test Series #	Specimen #	Powder Feed Rate [g/min]	Power [Watts]	Laser Speed [mm/s]
2	7	3.75	290	2.11

The results of the iterated model were compared visually to experimental data by the inspection of the fusion zone, as well as probe locations corresponding thermocouple placement.

V. EXPERIMENTAL PROCEDURE

Material

The goal in choosing a model material system was to select a material where characteristic markers would be left in the microstructure upon cooling that would allow us to quantify the peak temperature and cooling rates at various points in the sample. AISI 1018 steel was selected because certain phase transformations occur at fast and slow cooling rates, and the resulting microstructures can be analyzed readily and correlated to known empirical relations yielding the peak temperatures and cooling rate. Another consideration was the wide availability of both the steel plate and metal powder in the appropriate size range. The iron-carbon phase diagram is shown below with the composition of AISI 1018 steel indicated on the diagram.

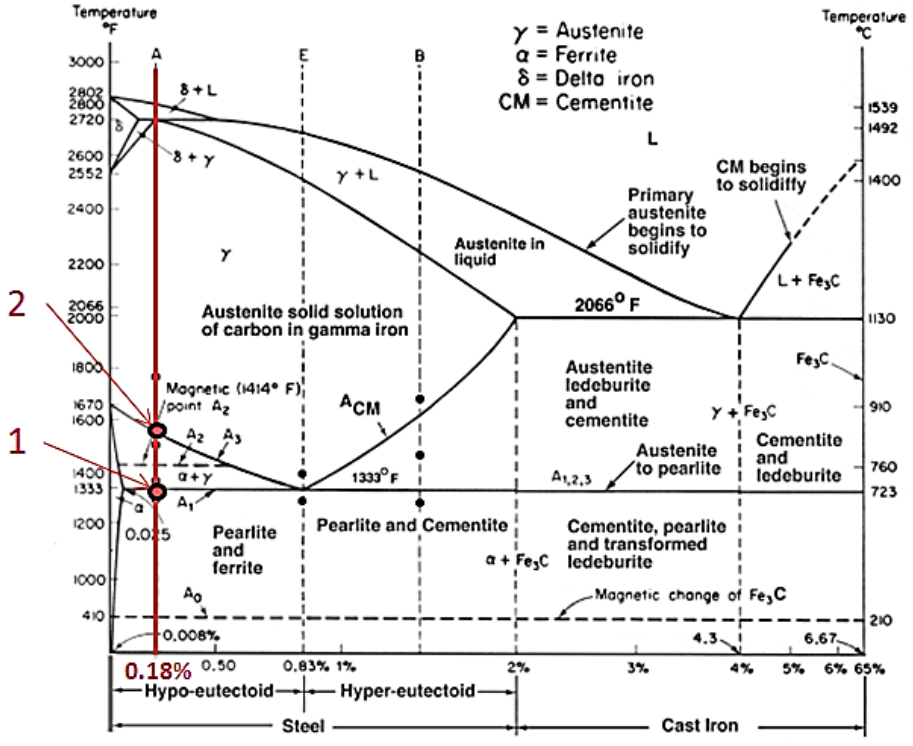

Figure 12: Fe-Fe_3C Phase Diagram. Taken from (22)

AISI 1018 steel has several unique thermal markers that can be used to experimentally determine cooling rates and peak temperatures. The original base metal has a homogenous microstructure consisting of coarse ferrite and pearlite with a slight anisometry in the grain shape in plane resulting from the cold finishing operation performed as the final step in its manufacture. After DMD, the microstructure within the fusion zone (FZ, the region where melting occurred) and the heat affected zone (HAZ, the region of the plate that did not melt but where solid state reactions occurred) is directly related to the peak temperatures and cooling rates experienced in these regions. Sufficiently far from the heat source, in the unaffected base zone (UBZ), the temperature is too low to influence the microstructure. Within the FZ and HAZ, cooling rates can be determined from both the pearlite spacing and from micro-hardness measurements. For regions that cooled at moderately fast or slower cooling rates, the pearlite spacing can be directly correlated to the solid-state cooling rate at the A1 temperature and below. At faster cooling rates micro-hardness can be used to estimate cooling rate because it is sensitive to the amount of martensite present at a specific location and the amount of martensite present is related to the cooling rate.

Peak temperatures can also be ascertained by examining where microstructural changes occur in the samples. In the region of the heat affected zone that is farthest from the heat source, prior ferrite grains will remain unchanged during heating from DMD but, pearlite will transform to austenite above the A1 temperature at point 1 in Fig. 12, which upon cooling will transform back to pearlite, but with a different spacing. This location where the pearlite spacing first changes can be used to identify the location where the temperature exceeded the A1 temperature. A second marker in the microstructure occurs where the peak temperature exceeds the A3 temperature at point 2 in Fig. 12. At this point, both the ferrite and pearlite transform into austenite, which upon cooling transforms back to ferrite and pearlite, but with a different ferrite grain size and possibly pearlite colony spacing. Thus visual inspection of the microstructure can be used to determine where the peak temperatures exceed the A1 and A3 temperatures.

Although generally not observed at typical cooling rates for welding in low carbon steels such as AISI 1018, the very high cooling rates that occur during DMD also lead to the formation of martensite and bainite. These phases are not shown in the phase diagram because they are metastable rather than stable, equilibrium phases. Since martensite and bainite phases form only from austenite, examination of the microstructure can also be used to determine the location where the peak temperature exceeded the A1 temperature (the lowest temperature at which pearlite transforms to austenite) under conditions where the cooling rates are fast enough to form martensite or bainite. The cooling rate at these specific locations can also be estimated. For example, from the continuous cooling curve shown in Fig. 13, a cooling rate of at least 59 $\frac{^{\circ}C}{sec}$ [3,540 $\frac{^{\circ}C}{min}$] is required to form even a small fraction of martensite. Even at very high cooling rates where considerable martensite is formed, it is accompanied by at least 50% bainite.

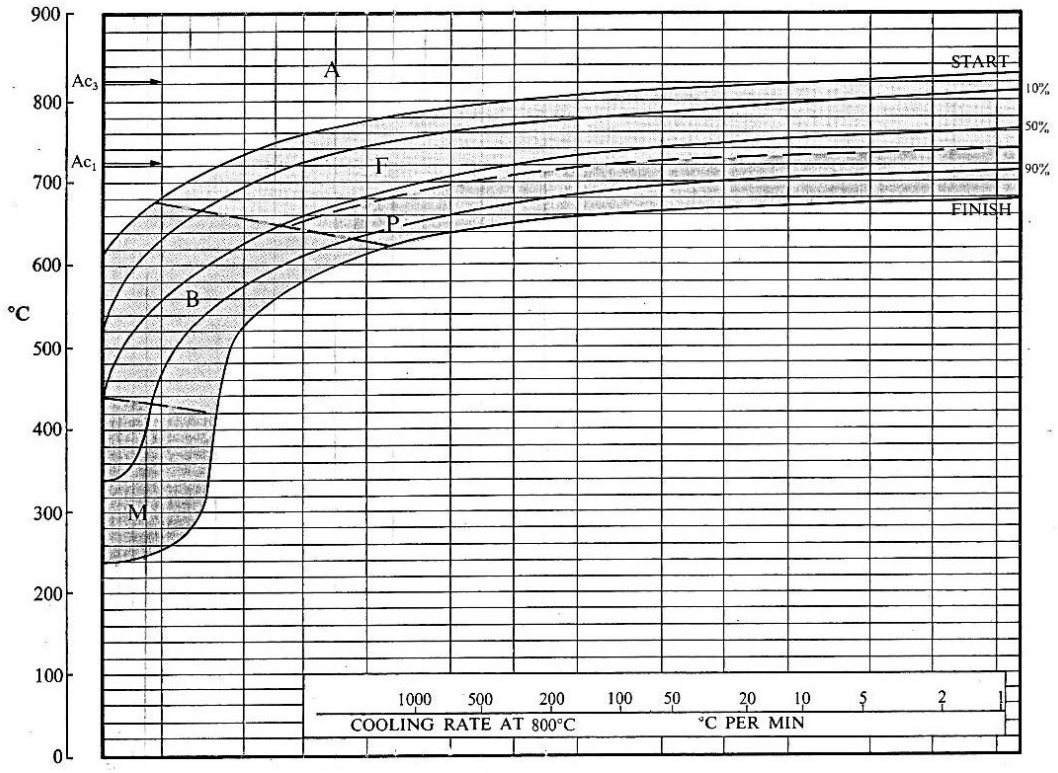

Figure 13: Continuous cooling curve for 1018 low carbon steel. Taken from the Atlas of Continuous Cooling Curves (23)

When martensite, bainite, and ferrite are present in the microstructure the micro-hardness at specific locations can, in principle, be used to determine the fractions of each phase present because these phases have different hardness values. Micro-hardness measurements can be correlated to known hardnesses of martensite, bainite, and ferrite+pearlite to determine percentage of martensite. Thus, by measuring hardness as a function of position, approximate location specific cooling rates can be determined. The relationship between the hardness and the cooling rate is determined experimentally using a Jominy test. A Jominy test is performed by bringing a sample rod to a fully austenitic state above the A3 temperature and then quenching it from one end with water. The resulting cooling gradient results from the unidirectional heat flux. The variation in cooling rate along the rod results in the stabilization of different types of microstructure and an associated variation of hardness. The hardness of an alloy is nominally proportional to the cooling rate; however the hardness values in Jominy tests are specific to each alloy type. The combined use of micro-hardness data, Jominy test data for AISI 1018, and the published conversion for distance along the rod during a Jominy test (the Jominy distance), allows the cooling rate to be determined from the hardness. A second cooling rate can be experimentally measured, if the cooling rate is slow enough, within the heat affected zone. The measurement of the pearlite lamellae spacing has been widely used to measure solid state cooling rates. The preferential diffusion of the Fe_3C cementite carbide out of the pre-existing γ-austenite is extremely cooling rate dependent. The width of the banded Fe_3C carbide and cementite inside the pearlite colonies can indicate the cooling rate.

Powder

The deposition material used was a -100/+200 mesh sieved *(-149μm/+74μm)* 1018 steel powder. The powder was originally manufactured by Nuclear Metals Incorporated (Concord, Massachusetts) for another project decades ago at LANL. In order to ensure the powder was

indeed 1018 steel, the powder was sent to Exova Corporation (Santa Fe Springs, California) for inductively coupled plasma mass spectroscopy *(ICP-MS)* testing to determine metallic composition. Additionally Horiba interstitial analysis was done at LANL to determine the carbon and sulfur content. The results are shown below:

Table 2: Metallic composition of the powder used in this study from ICP-MS measurements

	Major Metallic Constituents									
	Al	Cr	Co	Cu	Ge	Mn	Mo	Ni	P	V
%w	0.002	0.052	0.0047	0.073	0.0022	0.78	0.016	0.062	0.004	0.057
ppm	20	520	47	730	22	7800	160	620	40	570

Table 3: Interstitial carbon and sulfur content for the powder in this study

	Non-metallic Constituents	
	C	S
%wt	0.1939	0.0225
ppm	1939	225

Table 4: Comparison between the compositions measured in the powders used in this study and the standards for AISI 1018

	Alloying Element Weight Percent				
	Fe	C	Mn	P	S
AISI 1018	99.25-98.5	0.15-0.2	0.6-0.9	0.04 max	0.05 max
Powder Used	98.71	0.194	0.78	0.004	0.0225

From the combination of ICP-MS and interstitial analysis tests that were performed, it is evident that the powder being used is indeed AISI 1018 steel. Subsequently, the morphology, pre-deposition microstructure, and the particle size distribution were determined using metallographic mounting and polishing, along with image analysis.

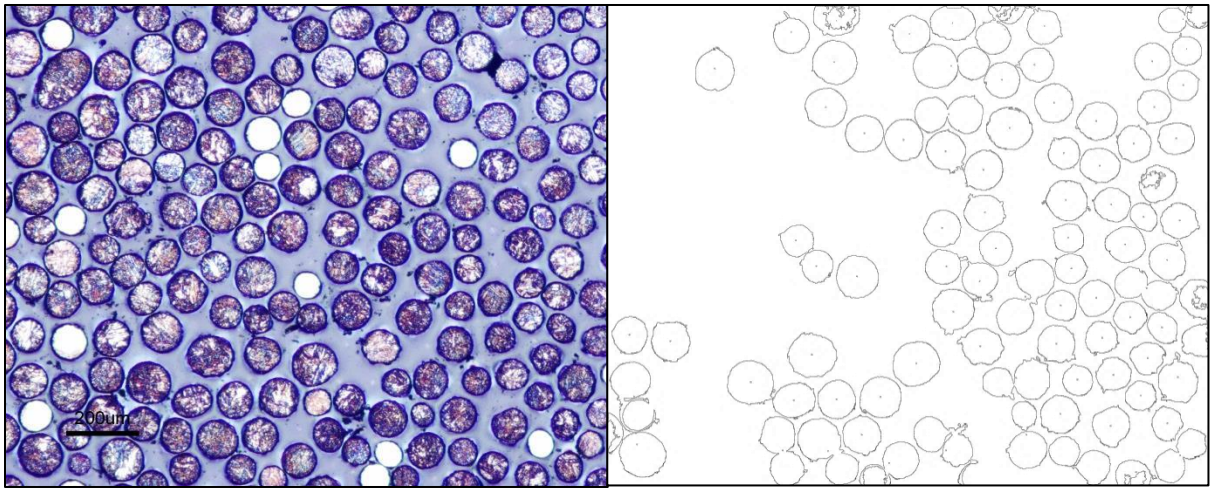

Figure 14: *(Right)* Example 10× micrograph of mounted, unprocessed 1018 powder. *(Left)* Image after processing using ImageJ™

This image analysis was performed by the summation of data obtained from four different micrographs using the ImageJ freeware (1.47v, NIH, Bethesda, MD). In order to obtain particle size distribution a series of image analysis steps were done.

1. Loading of the 4 micrographs into ImageJ
2. Setting a global measurement scale that relates the number of pixels to the 200 μm scale in the micrograph
3. Covert all images into 8-bit grayscale
4. Covert all images into binary
5. Remove the scale bar from each micrograph to prevent it from interfering with the data

6. Select “show outlines” to show the image seen on the left in Fig. 14
7. Run the automated analyze particle script in ImageJ, which measures the area of each of the particles and calculates an equivalent radius based on the assumption of a spherical particle. *(which applies well for the spherical gas atomized powder used in this study)*
8. Select “display results” and “summary” to yield the data in Table 5.
9. This data can be used to create the histogram seen in Fig. 15.

Table 5: Measured particle statistics

Diameter [μm]	**Number of Particles**
80	7
85	11
90	16
95	13
100	11
105	17
110	38
115	15
120	15
125	15
130	11
135	7
140	8
145	6

Particle Statistics		
Sample N=	196	particles
Mean	109.2	micron
St.Dev=	18.0	micron
Min=	75.0	micron
Max=	153.0	micron

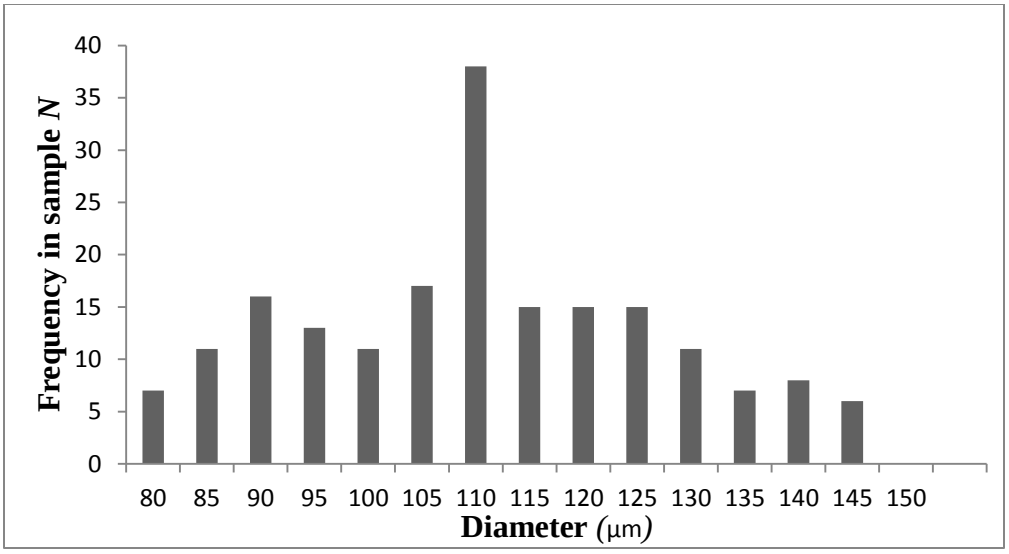

Figure 15: Powder size distribution histogram

However, because these measurements are taken from a random cross section of a sphere, there is an observation bias that systematically underestimates the true size of the sphere. The correction for this cross sectional measurement has been determined by Heilbronner (24) for normal distributions.

$$\frac{\mu_s}{\mu_r} = .91 \qquad \text{Eq. 26}$$

$$\frac{\sigma_s}{\sigma_r} = 1.04 \qquad \text{Eq. 27}$$

μ_s = Measured cross section mean particle diameter

μ_t = True mean particle diameter

σ_s = Measured cross section standard deviation of particle diameter distribution

σ_t = True standard deviation of particle diameter distribution

When this correction is applied, the true mean particle diameter μ_t is 121 μm and the true standard deviation σ_t is 17.3 μm.

Substrate

In order to maintain a consistent material system throughout the deposit, the same material was used for the powdered steel and the steel in the substrate. The substrate that was used was part number F3145, C1018 Cold Finish Flat bar, from Metals Depot (Winchester, Kentucky, USA). Eleven 5 in. × 4 in. × ¼ in. cold finished 1018 steel blanks were cut from the bar for use as substrates for DMD. After cutting, the plates were ground on both sides to remove surface oxide and contamination. Next, each plate was marked with an engraver at the target locations of the deposition lines. The plates were then placed in an ultrasonic detergent bath to remove any grease or residue from machining. Once the plates were cleaned they were individually measured, weighed, and engraved with a number to track them throughout the process. In order to prevent the relatively rapid oxidation of the 1018 substrates, they were each stored in separate heavy duty plastic containers with a desiccant inside.

In order to obtain *in-situ* temperature data from each of the samples, two type K (Alumel/Chromel) thermocouples were attached to the surface at a distance of approximately 2 and 2.5 mm away from the deposition centerline using a Gleeble 1000 spot welder. The nature of this spot welder made precise placement difficult, so the locations of the thermocouples were measured more precisely after they were spot welded to the surface of the plate. In order to prevent premature contact of the thermocouples, shrink-tubing was placed on each wire to isolate them until intended contact on the surface of the plate. Each thermocouple was then secured with heat resistant aluminum tape to add structural integrity and protect the low melting temperature shrink tubing. A representative plate after attachment of the thermocouples but before deposition is shown Fig. 16.

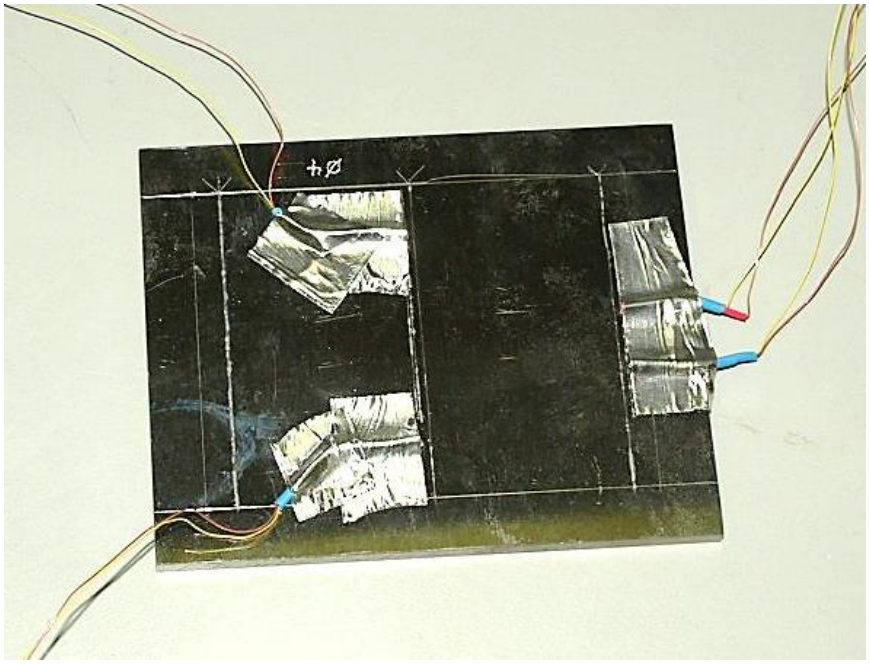

Figure 16: Instrumented 1018 steel substrate ready for LENS MR-7 experiment

The LENS unit used did not have thermocouple inputs for data acquisition, so a wireless unit was connected and tested prior to introduction into the glovebox. The wireless unit transmitted data to a computer outside the machine using an Agile-Link MicroStrain (LORD, Williston, Vermont, USA) using a 128 bit analog channel.

Test Configuration

Each substrate was marked for three deposition tests, but only 2 of the depositions could be instrumented, due to limitations in data acquisition transmitter. The deposition geometries that were selected for instrumentation were 1) a single pass line and 2) a one inch tall wall, built from multiple passes. A schematic of the thermocouple array is shown for one of the tests in Fig. 9.

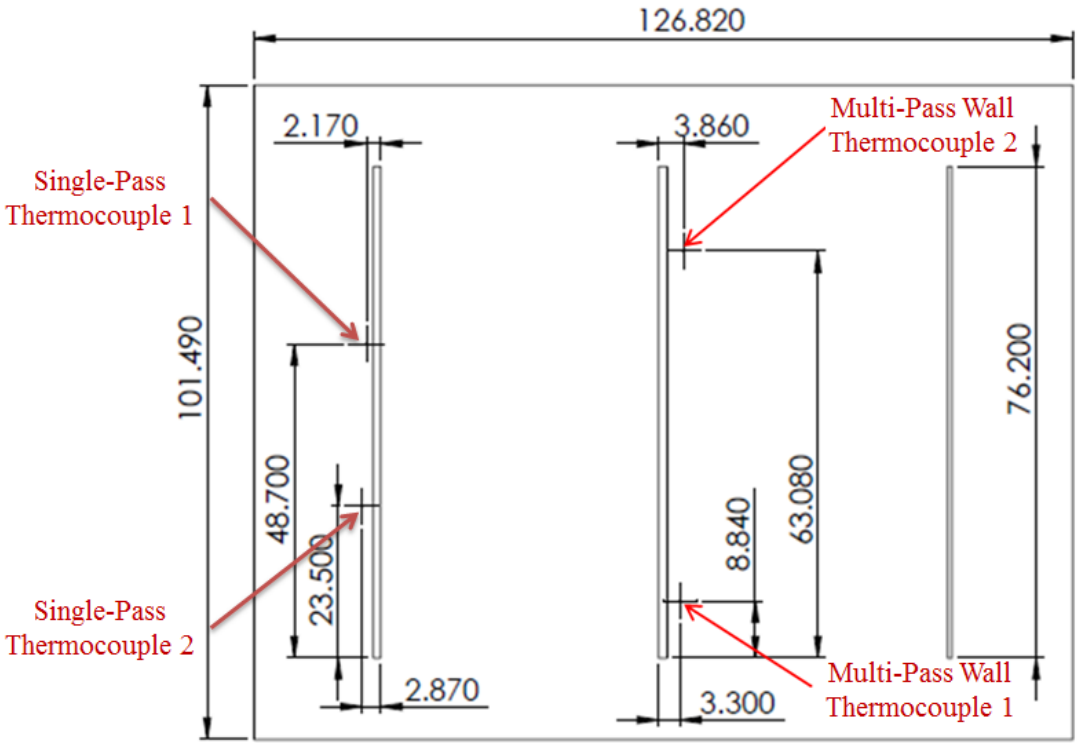

Figure 17: Schematic showing the locations of three lines produced using LENS along with the thermocouple locations

In order to quantify all of the deposition parameters, the power being produced by the laser and the powder flow rate need to experimentally measured. To determine the power being produced by the laser, a lollipop calorimeter was placed in the laser focus for 30 second intervals at the power levels tested. The power levels measured by the calorimeter were used as the input power in order to account the losses that were present in the laser. Additionally the powder flow rates were measured by flowing powder into plastic bags for 1 minute and weighing the powder that was deposited.

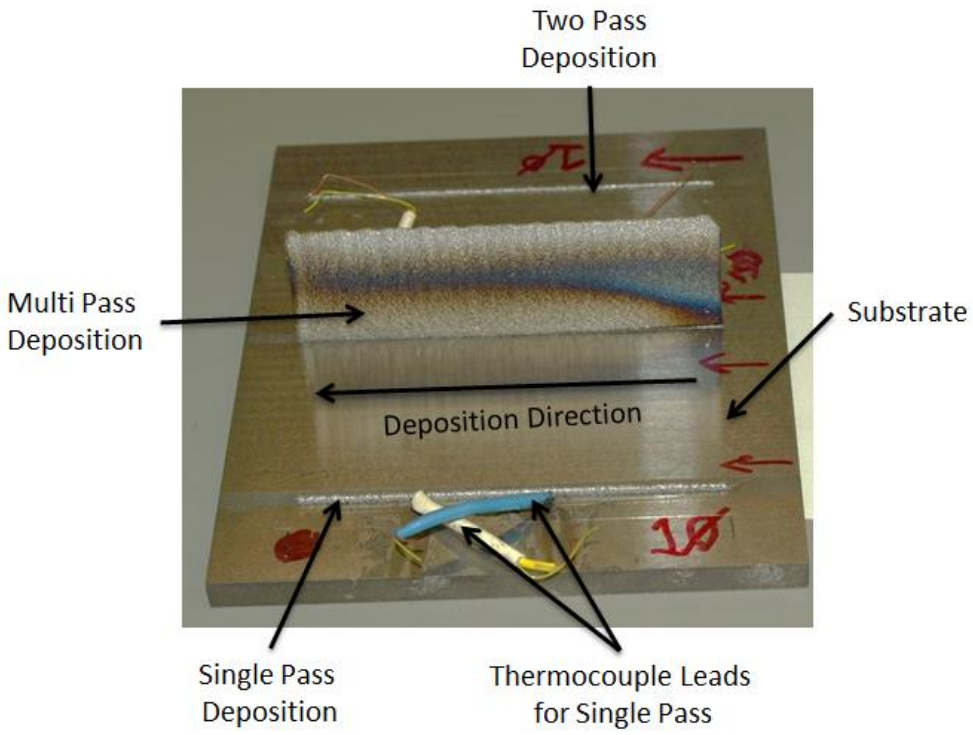

Figure 18: Completed test series of three depositions per substrate

Sample Preparation

After the samples were deposited using the LENS machine, each plate needed to be sectioned so that each deposition line could be examined. This presented an interesting problem in that post-deposition sectioning can introduce a damage layer on the sample depending on how much heating occurs during cutting. In order to decrease the size and magnitude of this damage layer, two different machines were used to section each of the samples.

The first saw used was a high speed Struers Labotom (Struers Incorporated, Westlake, Ohio, USA), which is a cooled abrasive saw. The coolant is deposited directly onto the spinning blade while cutting and minimizes heat buildup adjacent to the cutting surface. This saw was used for the rough cutting needed to isolate each of deposits from each other. These rough cuts

were made by making 5 cuts parallel to the deposits, each with a generous offset from the deposits themselves. By cutting at an offset from the deposits, the damaged layer that was created existed only in the substrate at a large relative distance from the deposit itself and the data-rich heat affected zone.

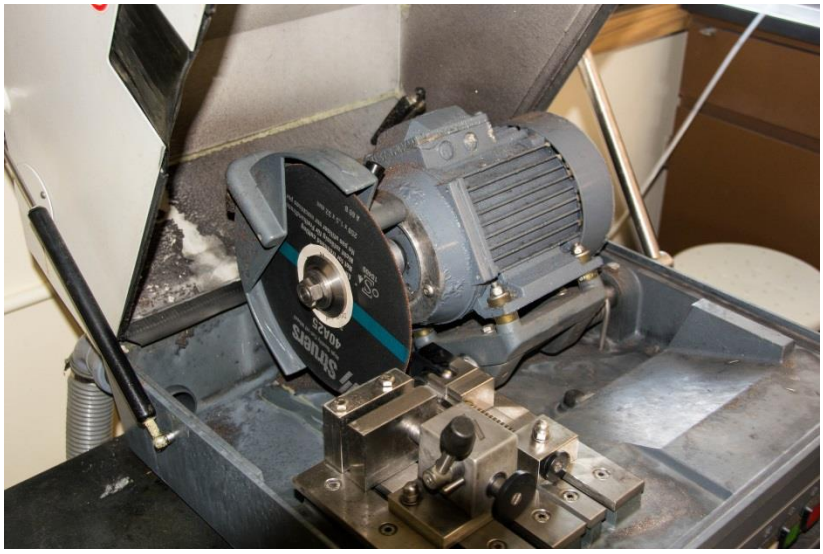

Figure 19: Struers Labotom cooled abrasive saw

The resulting sectioning left each sample isolated (shown in Fig. 20) and ready to be cut perpendicular to the deposition direction with a low speed saw that generated minimal heat but had a much slower cutting speed.

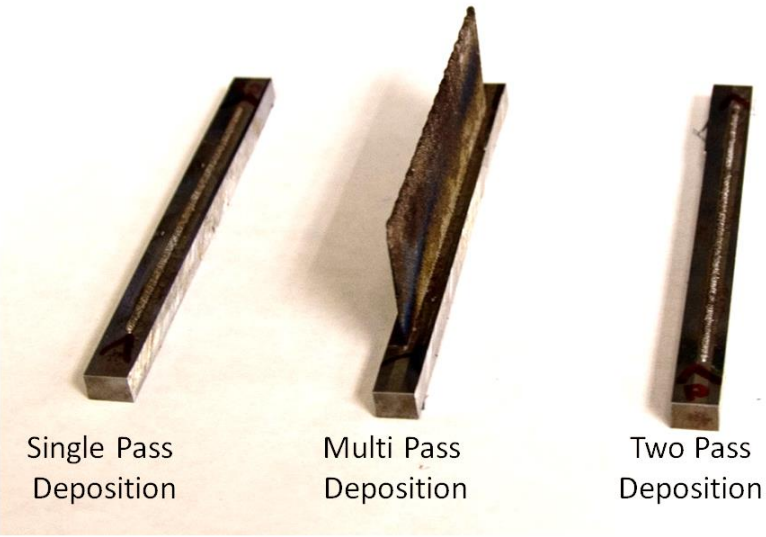

Figure 20: Examples of samples after cutting on the high speed saw

The low speed saw that was used to cut the cross sections was a Struers Isomet saw (Struers Incorporated, Westlake, Ohio) equipped with a Buehler 5 inch Isomet wafering blade 20HC (Buehler, Lake Bluff, Illinois, USA). The low speed and forces used by this saw produced a minimal damage layer that could easily be taken off during polishing.

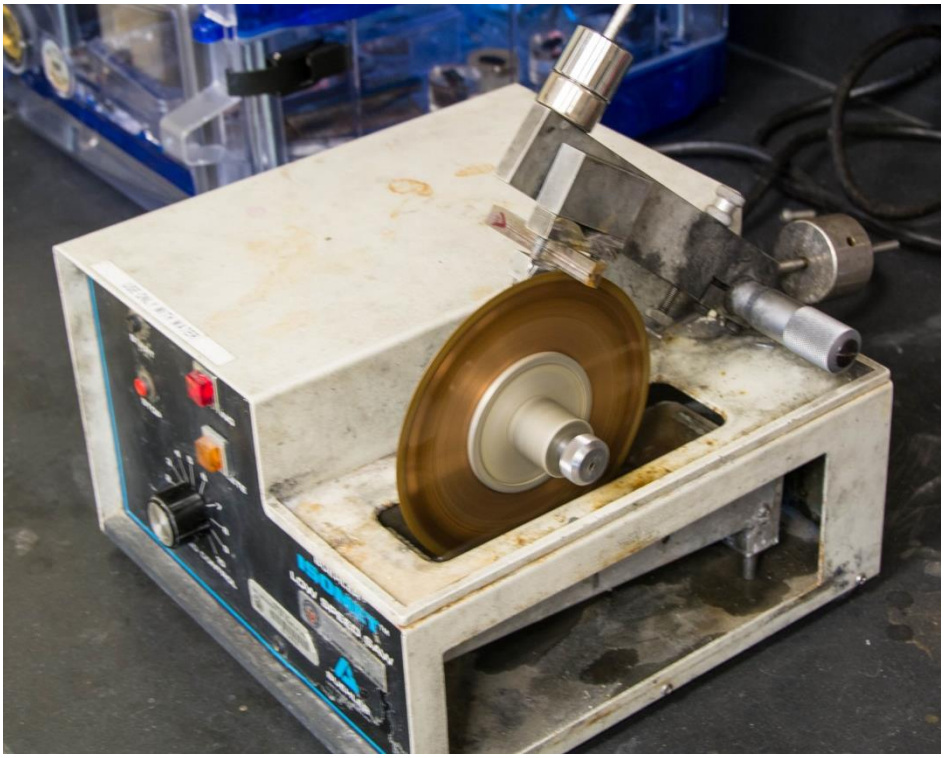

Figure 21: Struers Low Speed Isomet Saw

Each deposition was cut into two small cross section samples so multiple etchants, and visualization techniques could be explored. The samples were mounted using Buehler Kwick Kit long cure epoxy (Buehler, Lake Bluff, Illinois, USA) to reduce possible thermal effects from the curing process. After the samples had completely cured, they were stored in a desiccator to minimize oxidation that occurs under ambient conditions in low carbon steels of this type.

Prior to examination under an optical, stereo, or scanning electron microscope the samples were polished and etched. The polishing process for 1018 steel is well documented and was conducted following the procedures recommended by Struers. The polishing system used was comprised of a linked Struers Rotopol-11 and Struers RotoForce-1 (Struers Incorporated, Westlake, Ohio, USA) that held 3 samples at a time in a rotating rack, on top of rotating platen.

Figure 22: Struers RotoPol-11, Rotoforce-1 system

A first rough grinding pass was done with 240 grit silicon carbide paper that removed the small damaged layer caused by sectioning on the isomet saw. A second pass of much finer 600 grit silicon carbide was then performed to minimize the deep scratches left from the 240 grit paper. After grinding, polishing was performed using a series of successively finer diamond suspensions to slowly reduce the depth of scratches and create a mirror-like surface. The series of diamond suspensions used was, in order, 9µm, 3µm, and 1µm. These diamond suspensions were applied on the Struers RotoPol-11 for approximately 5 minutes each at 30 N of force.

After the diamond suspension polishes, a final pass of 0.05 µm alumina polish was done and the sample was then washed, cleaned with ethanol, and dried with a heat gun to reduce the adherence of any solidified chemicals and minimize oxidation. The polishing process of metallography is the most sensitive part of sample preparation; hand washing, sample cleaning, and glove changes were done in between each step of the process to ensure no contamination from previous polishing steps.

In order to be able to distinguish microstructure, the samples were chemically etched. The etchant preferential reacts with certain types of boundaries and creates a slight topography that is visible in light microscopes and electron microscopes. The reagent used for most steels to reveal microstructure and pearlite spacing is Nital, which is a mix of nitric acid and ethanol. The amount of nitric acid in the solution controls the etching rate of the solution; however, as the etchant concentrations approach 10% nitric acid, the mixture becomes explosive. The etchant used in this study was a 5% nitric acid Nital etch. To etch the samples, soft cotton-tipped applicator was immersed into the 5% Nital and was swabbed across the surface of the sample for 10-15 seconds and immediately immersed in de-ionized water to stop the chemical reaction. The samples were then individually placed in an ultrasonic bath, washed with ethanol, and dried with a heat gun. At this point the samples were ready for examination under various microscopes, and hardness testing.

Figure 23: Wilson Tukon 2100 micro-hardness tester

Cooling Rate Determined from Linear Regression

Micro-hardness measurements were used to experimentally determine calculate cooling rates by using data taken from the literature (25) (26) obtained from Jominy tests. To obtain cooling rates, first Vickers hardness values were converted to Rockwell C scale hardness. From previously reported data from Jominy tests, the Rockwell C hardness was then correlated to the Jominy distance. Finally, the Jominy distances were then directly correlated to cooling rates at 704ºC.

To convert the Vickers hardness values to Rockwell C hardness values, and empirical expression was determined from a linear regression to the experimental data, as shown in Fig. 24. This relationship was found to be

$$H_{RC} = 38.063\ln(H_V) - 186.48 \qquad \text{Eq. 28}$$

H_{RC} = Rockwell C scale hardness value H_V = Vickers scale hardness value

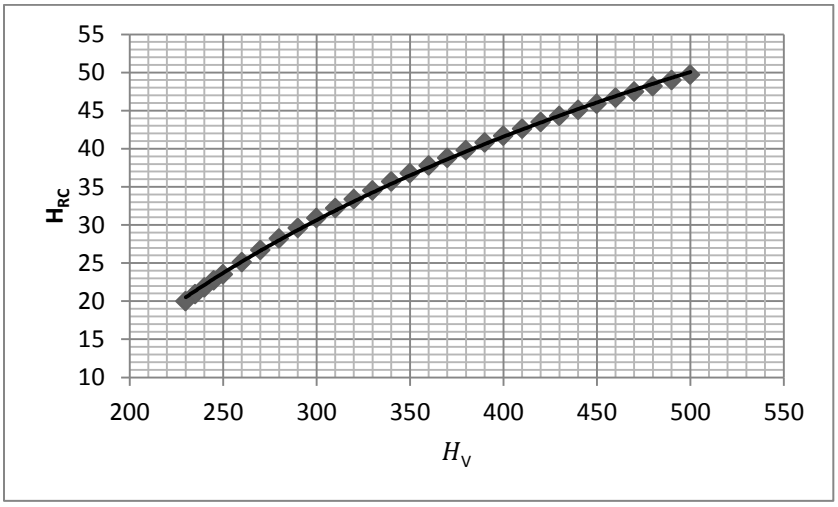

Figure 24: Conversion between Vickers hardness to Rockwell C hardness

A second linear regression was then performed to obtain the relationship between the Rockwell C hardness and the Jominy distance for AISI 1018 steel, which is shown in Fig. 25. The relationship obtained from the linear regression is given by

$$d_{jom} = -1.09E\text{-}05(H_{RC})^3 + 5.535E\text{-}04(H_{RC})^2 - 2.167E\text{-}02(H_{RC}) + 8.41E\text{-}01 \qquad \text{Eq. 29}$$

H_{RC} = Rockwell C scale hardness value d_{jom} = Jominy Distance

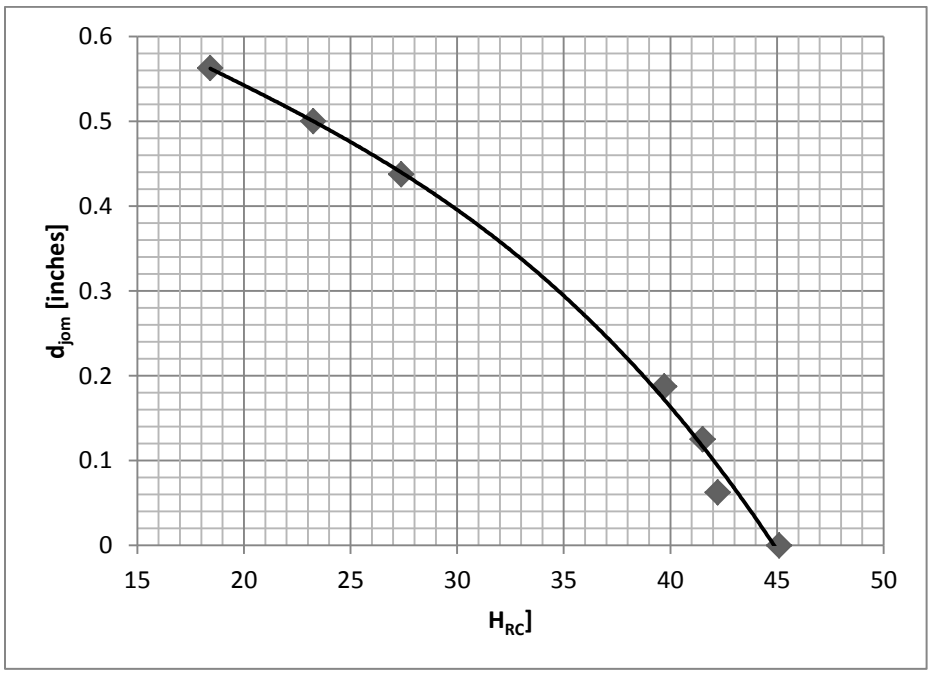

Figure 25: Jominy distance as a function of hardness. Values were calculated from published elemental composition relations. (26) (27)

A third linear regression was then performed to obtain the relationship Jominy distance and cooling rate, which is shown in Fig. 26. The relationship obtained from the linear regression is given by:

$$\frac{\delta T}{\delta t} = 6.0594(d_{jom}^{-1.41})$$ Eq. 30

d_{jom} = Jominy Distance t = time

T = Temperature

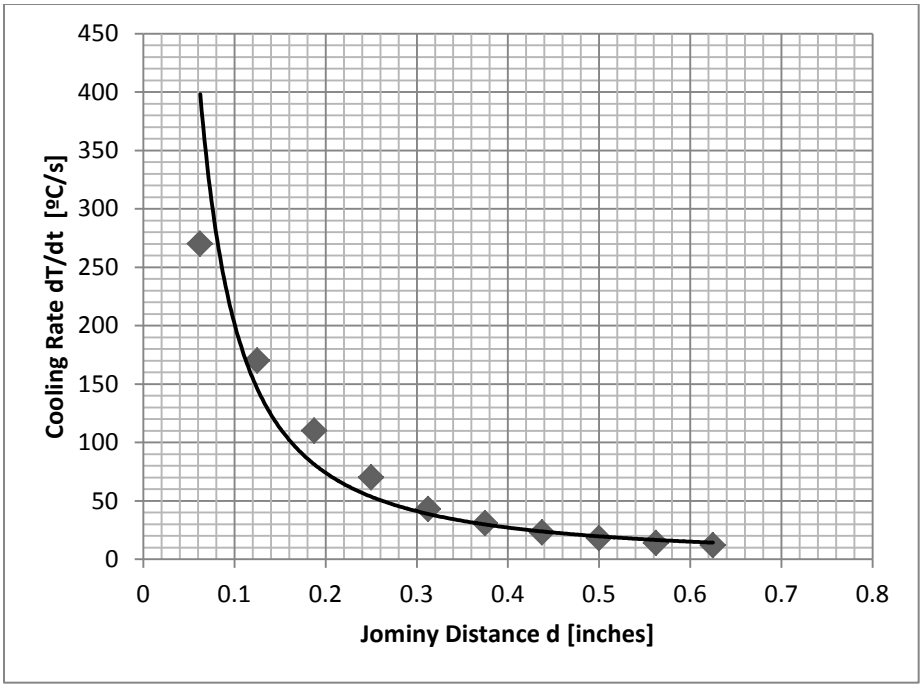

Figure 26: Calculated cooling rates determined from Jominy distances and cooling rate at 704ºC. (25) (26)

The serial application of these three linear regressions allows the calculation of approximate experimental cooling rates at the tested points.

VI. RESULTS

Test Data

Initial test conditions used to produce the LENS samples are shown in Table 6.

Table 6: Initial input parameters for LENS experiments

Test Series #	Specimen #	Initial Powder Feed Rate [g/min]	Power [Watts]	Laser Speed [mm/s]
1	10	13.98	430	6.35
2	7	3.75	290	2.11
3	6	15	600	19.04

For each test the dimensions of the resultant depositions were measured using a micrometer. The results of the measurements are shown in Table 7.

Table 7: Dimensions for each deposit produced.

	Single Pass		Multi-Pass Wall		Double Pass	
Test Series #	Height [mm]	Width [mm]	Height [mm]	Width [mm]	Height [mm]	Width [mm]
1	0.626	0.917	25.96	1.5	1.161	1.211
2	0.533	0.797	26.02	1.34	1.062	1.145
3	0.629	0.992	18.13	1.46	0.632	0.917

The specific energy for each test was calculated from supplied laser power divided by the horizontal speed of the laser. This quantity is a way of comparing depositions produced from combinations of different laser powers and deposition speeds across multiple samples.

$$\text{Specific Energy} = \frac{P_0}{v} \qquad \text{Eq. 31}$$

Morphology of Deposits

SINGLE PASS SAMPLES

Each single pass deposition was done first in the three test series to eliminate the preheating of the substrate. The three cross sections for the single pass depositions are shown below etched with 5% Nital at 5× magnification.

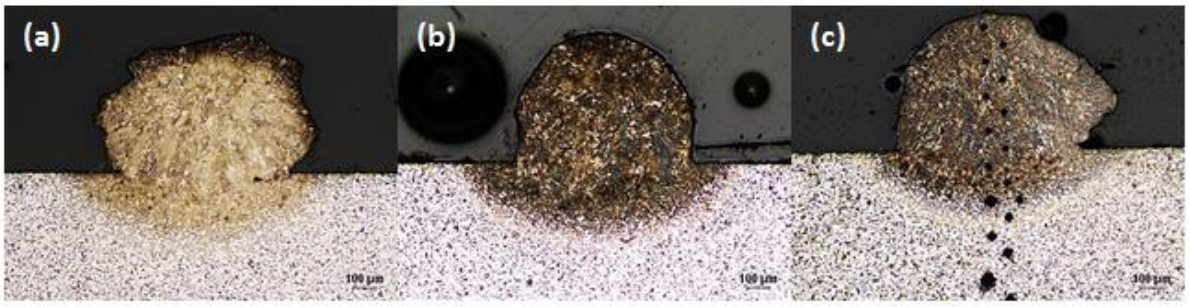

Figure 27: Single pass depositions samples from: Test 1 (a), Test 2 (b), Test 3 (with Vickers hardness indentations) (c)

The first sample had the highest powder feed rate and was performed under moderate laser power and speed. From Fig. 27(a), it is apparent that it yielded good deposition characteristics. For the second sample, the powder feed rate, laser power, and laser speed were all reduced compared to the first sample. This resulted in material being deposited very slowly and being slightly overheated. The overheating is apparent in Fig. 27(b) from the slightly larger fusion zone within the substrate compared to the others. For the third sample, the powder feed, laser power, and laser speed were all increased relative to sample one. From Fig. 27(c), it is apparent that there was very little overheat in this test, as the fusion zone and the deposition have nearly the same diameter. However it is clear from subsequent micrographs that the speed of deposition led to instability in the melt pool, leaving large closed voids inside the deposition.

These defects are not apparent from the surface, but further inspection of subsequent test geometries led to the uncovering of more issues with the third test series.

TWO PASS SAMPLES

The second sample geometries deposited during each test series were the two pass samples. The two pass samples were deposited on the on the opposite side of the substrate compared to the single pass samples, and consisted of two deposited lines, stacked on top of each other. Between the passes, the deposition head height was increased a distance of ~0.51mm (0.02 inches). The 5× cross-sectional micrographs of the two pass tests are shown below in Fig. 28.

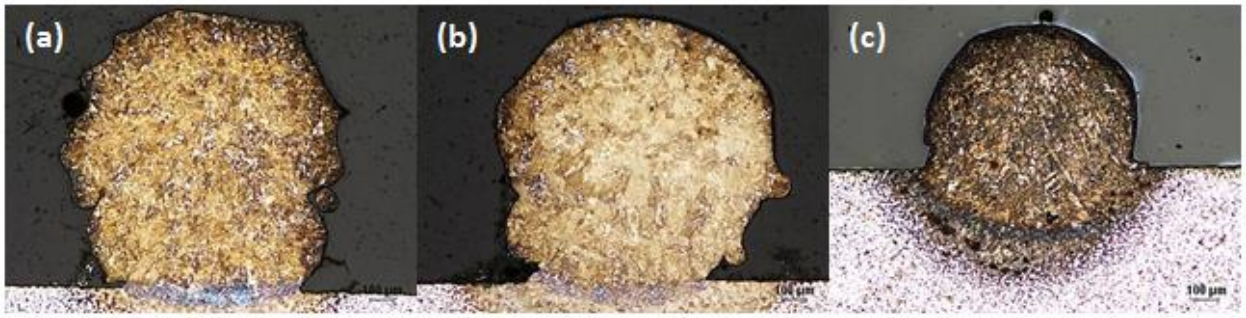

Figure 28: Two pass depositions: Test 1 *(a)*, Test 2 *(b)*, Test 3 *(c)*

The first sample shown in Fig. 28(a) appears to be nearly flawless. The deposition head movement resulted in a roughly doubling of the wall height, which means the laser is at roughly the same distance from the deposit than it was after the first pass. The second test series' two pass sample (Fig. 28(b)) also increases in height, but noticeably less than the first. This difference will compound over successive passes and lead to the focus of the laser becoming unburied in the wall deposits (this phenomena is coined 'runaway' by the operators of the LENS MR-7™). The runaway effect is more drastically shown in the third test (Fig. 28(c)), which increased in height minimally relative to the single pass height.

ONE INCH WALL

The multi-pass depositions consisted of 50 passes, each with a 0.02 in. (0.51 mm) vertical offset between each resulting deposit that was approximately 1 in. (25 mm) tall. However the true height of the deposits varied depending on the laser power, speed, and powder feed rate. This is in contrast to the single pass samples produced at the same powder feed rate, laser power, and laser speed as the multi-pass samples, but which exhibited minimal differences in height.

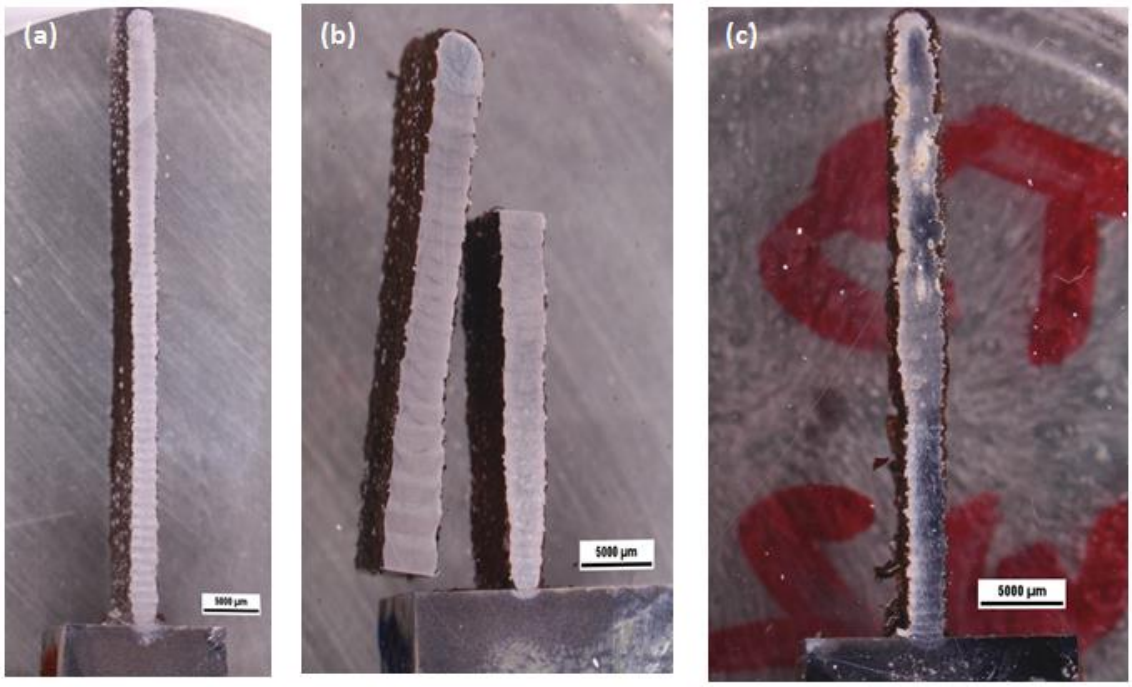

Figure 29: Stereo microscope images of the *multi-pass samples* for tests 1, 2, and 3 (*from left to right*). *Note that in b) the deposit was cut along its height so that it could be fit in the mount.*

Each of the multi-pass samples exhibit very different morphology. The first test series, the multi-pass sample has uniform thickness and layer height throughout. It is nearly ideal, except that it is 500µm taller than intended (note that 500µm over the total 25.4 mm height is an error of only 2%). The second test series, multi-pass sample exhibits characteristics that suggest that there was a variation in the powder feed. Initially the deposition was underfed, and the layer heights were small and narrow. The underfeed of powder was then over corrected resulting in

overly tall and wide layer heights; the actual height was 26.02 mm rather than the intended 25.4 mm. It is immediately apparent that third test series settings led to a severely degraded multi-pass sample. In addition to be 29% shorter than intended (18.31 mm instead of 25.4 mm), there are large closed voids in the upper portions of the deposit that would severely degrade the mechanical performance if they existed in a production component.

MICRO-STRUCTURES FOR SINGLE-PASS SAMPLES

Experimental measurements of cooling rates and peak temperatures were taken both *in-situ* and *post-mortem* using different tests and data acquisitions. The *in-situ* measurement was made using thermocouples attached to the surface of the substrate to measure the temperature transient.

The *post-mortem* thermal characterization of the specimens was inherently designed to have thermal markers in two regimes of cooling; the time dependent martensitic composition or pearlite spacing. Figs. 31-33 are composite 10× macroscopic views of single pass tests, with 100× detail views at specific points of interest. Hardness measurements were taken using a Wilson Tukon 2100 micro-hardness tester.

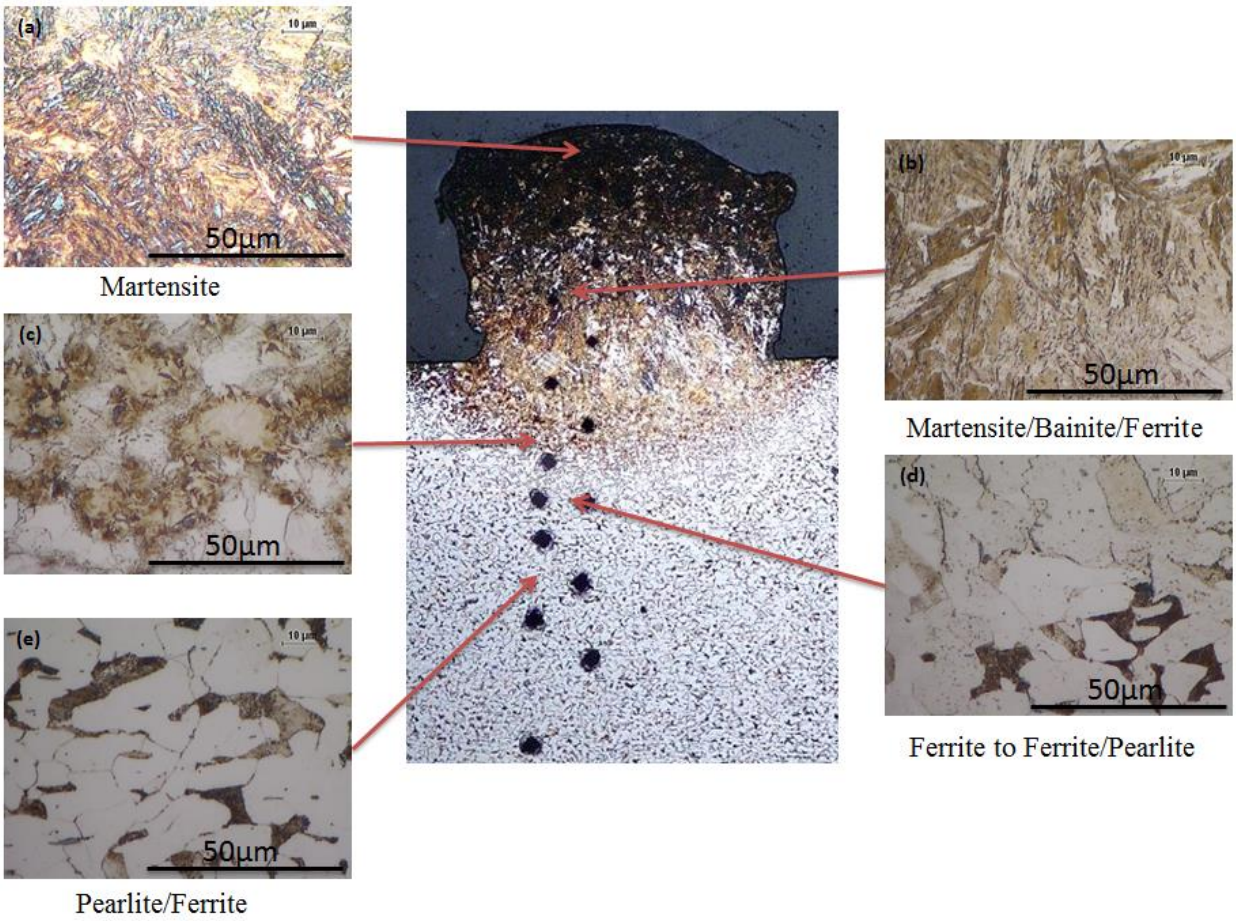

Figure 30: Test 1, Single pass sample. 10× macroscopic composite and accompanying 100× micrographs at points of interests. Note the presence of Vickers indentations in the 10× macroscopic composite.

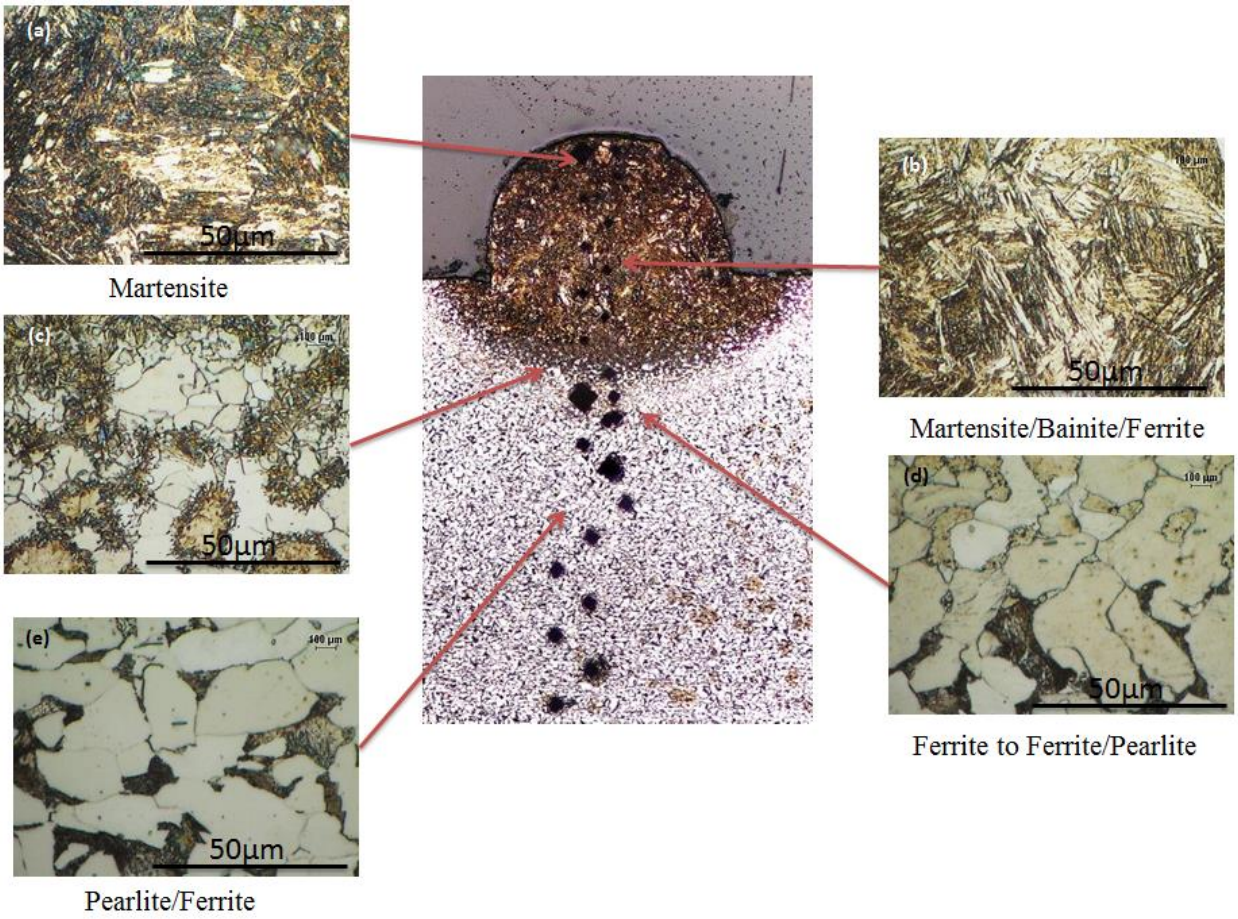

Figure 31: Test 2, Single pass sample. 10× macroscopic composite and accompanying 100× micrographs at points of interests. Note the presence of Vickers indentations in the 10× macroscopic composite.

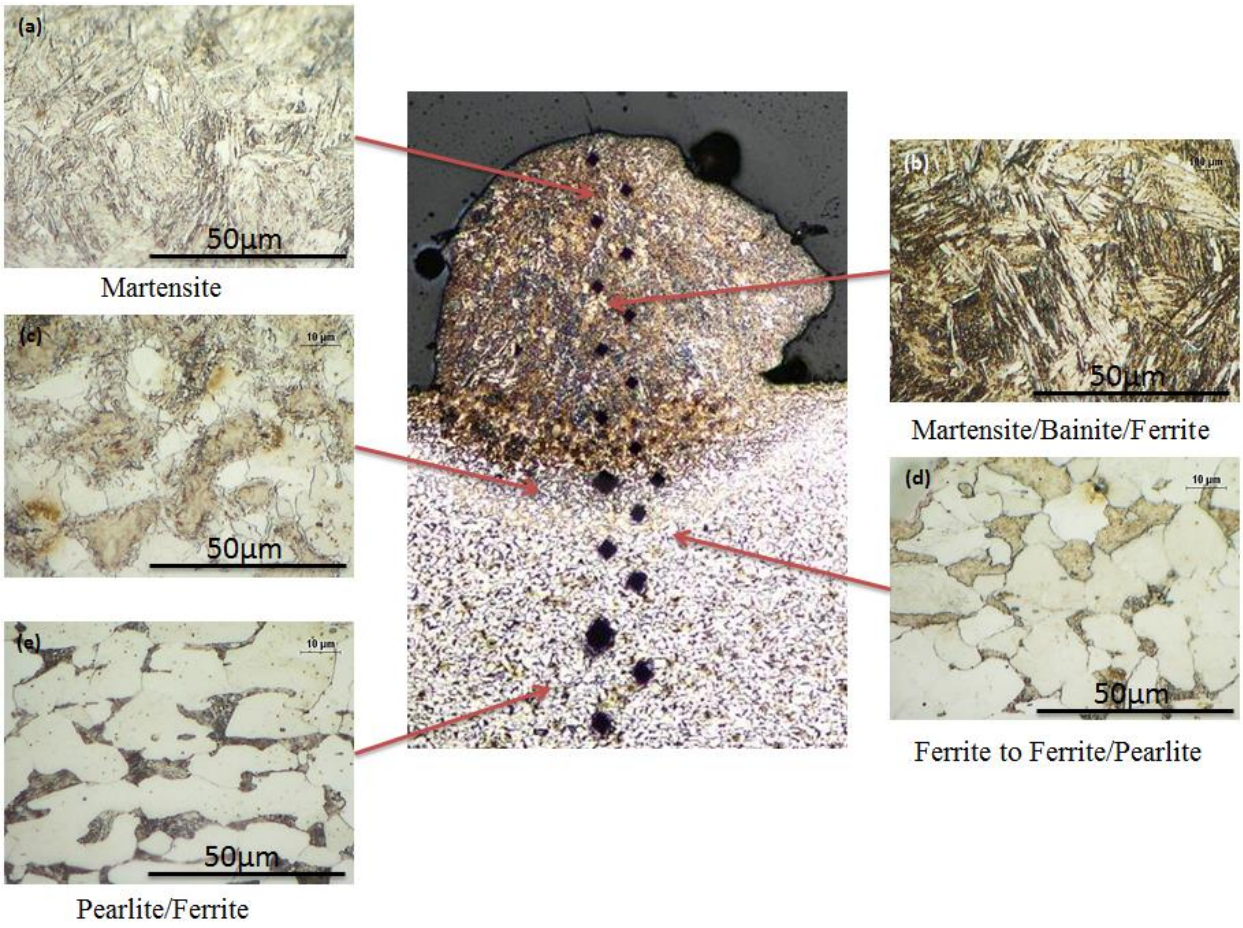

Figure 32: Test 3, Single Pass sample. 10× macroscopic composite and accompanying 100× micrographs at points of interests. Note the presence of Vickers indentations in the 10× macroscopic composite.

HARDNESS TESTING FOR SINGLE PASS SAMPLES

The x-y coordinates of each test point were recorded by a micrometer, along with their corresponding hardness value. After all the data was gathered, the vertical location corresponding to the top surface of the substrate was set to zero. Therefore all the distances in Fig. 33 are relative to the original substrate surface.

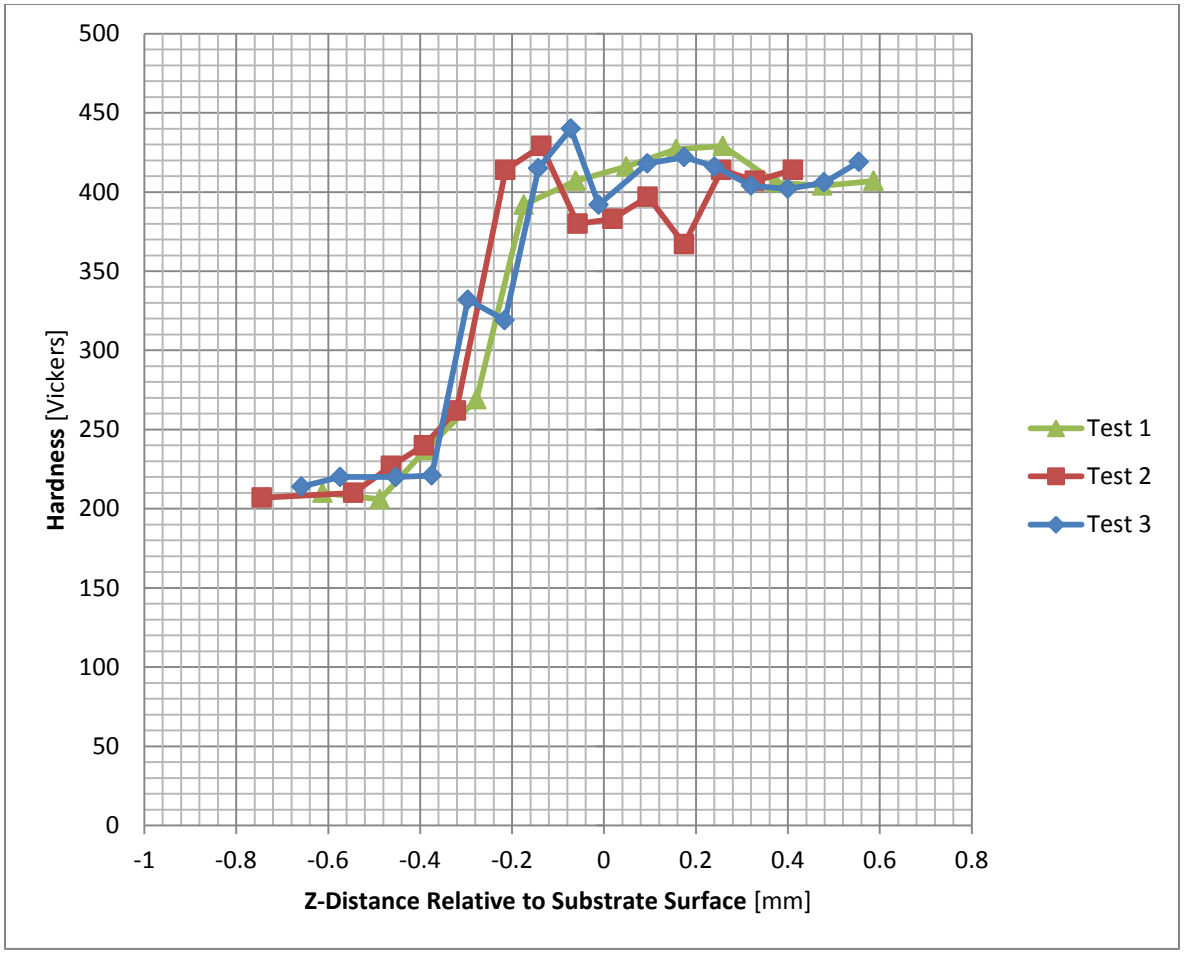

Figure 33: Hardness of single pass depositions for each test as a function of position, relative to the surface of the substrate

All of three of the single pass samples showed the same general trends in micro-hardness: a low hardness away from the deposit, a steady increase in hardness within the heat affected zone, and a nearly constant hardness within the fusion zone. The hardness profiles suggest that the fusion zone extends into the substrate by 150 - 200 µm, depending on operating conditions since the hardness is constant in this region and approximately equal to that in the deposit. Test 2 exhibits the largest fusion zone, which is to be expected since the deposition speed was slowest for this sample, and there was some overheating of the deposit as a result. The micro hardness measurements show that the heat affected zone extends another approximately 200 µm into the substrate, below the fusion zone.

VII. DISCUSSION

Post-Deposition Process Analysis

Powder-use efficiency is very important in DMD; higher efficiencies decrease the cost of the process. Literature values of power use efficiencies can range widely due to their high dependence on input parameters. The powder efficiencies for this test were calculated from

$$\text{Powder Efficiency} = \frac{\Delta W v}{53 \times L \dot{m}} \qquad \text{Eq. 32}$$

L = Length of molten pool v = Velocity of deposition head

$\dot{m}$ = Powder flow rate at nozzle ΔW = Change in weight of the sample

The measured power efficiencies are plotted in Fig. 34. From this plot it is apparent that the powder-use efficiency appears to increase approximately linearly with specific energy in the range specific energies that were measured.

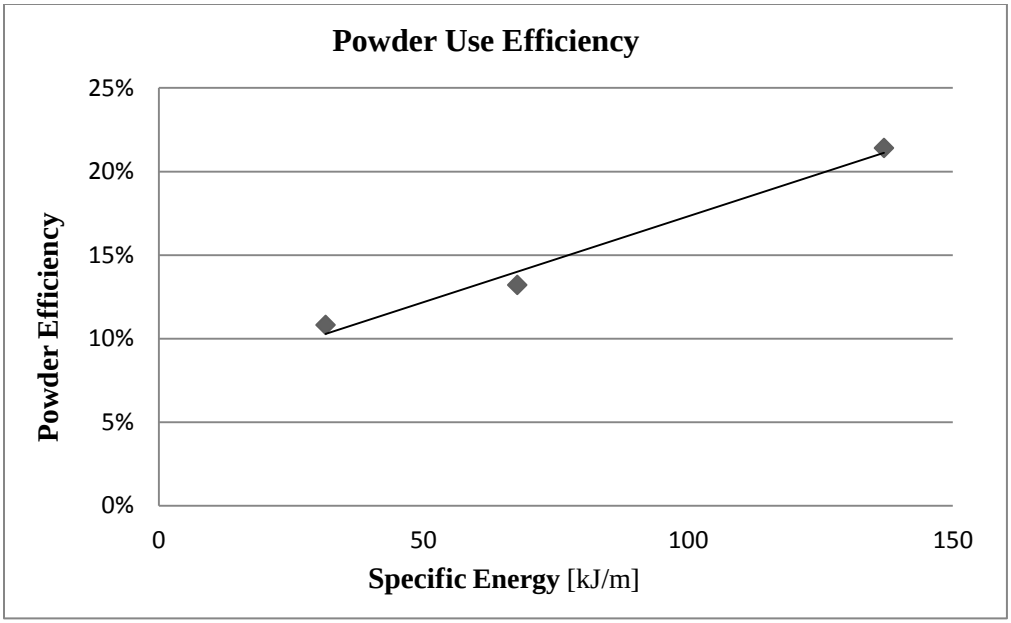

Figure 34: Powder use efficiency as a function of specific energy

In producing the deposits, a phenomena known as runaway was observed on the 1 inch tall multi-pass depositions. Runaway occurs when the powder flow supplied is insufficient to create a deposit of a height that corresponds to the upward z-step of the deposition head. If this condition exists for multiple passes, the laser becomes increasingly defocussed relative to the top of the deposit. This induces a phase transformation in the powder in flight. The highly elevated power density can liquefy, and possibly form plasma from the powder, which is then deposited on top of the wall. This phenomenon changes the deposition regime and results in a wavy and highly porous deposition. In order to be able to tightly control the deposition geometry, the runaway phenomena must be avoided. The data below shows which powder feed rates at specific energies result in an unstable, runaway, deposition regime.

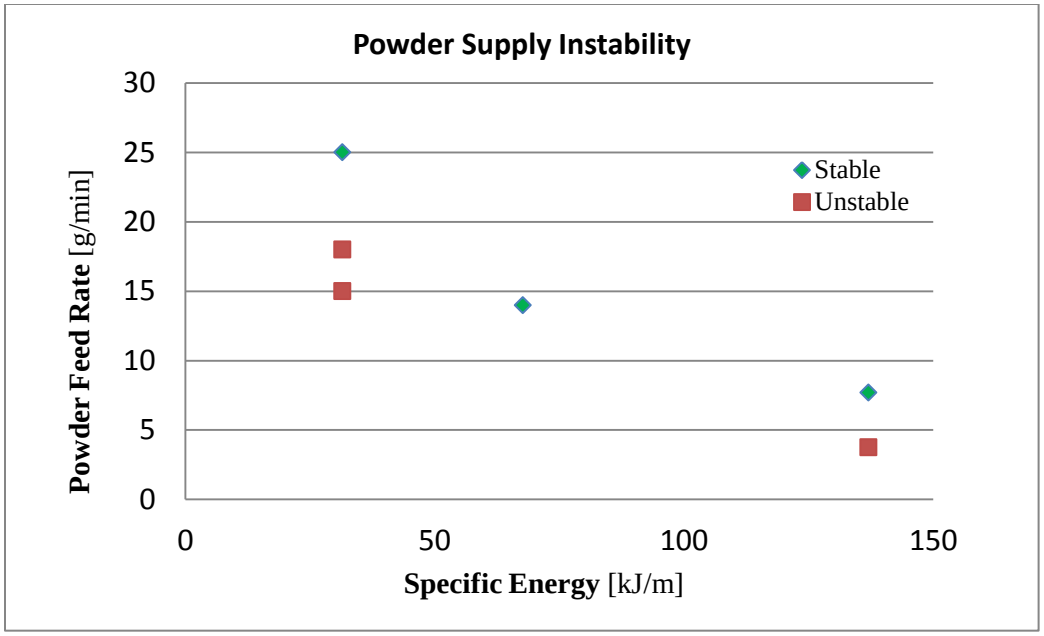

Figure 35: Powder supply stability as a function of specific energy, showing the minimum feed rate necessary as a function of specific energy to avoid runaway.

Process Effects on Sample Morphology

The first test's wall sample was produced using a moderate powder feed rate and moderate laser power and speeds and has a nearly uniform thickness throughout with consistent layer size. This is because the initial powder flow was optimized for the specific energy of the test through trial runs.

The second test's wall sample was started lean on powder supply ($3.75\frac{g}{min}$), however the runaway phenomena began occurring around ⅓ of the way up the wall. A quick decision was made to increase in the powder supply to save the component and the powder flow rate increased to ~8 $\frac{g}{min}$. When the powder feed was adjusted it was inadvertently overfed powder, leading to much larger layer heights as well as wider layer height. The saturation of powder was so drastic that the deposited wall was actually taller the intended 1 inch, which is why it had to be sectioned to be mounted for metallography.

The third test was done by a new LENS™ operator and it was recommended against my better judgment that the powder feed rate remain at 15.0 $\frac{g}{min}$, similar to the 13.98 $\frac{g}{min}$ that was used in test series one). My intuition was validated; the powder feed rate was woefully lacking. The extremely fast deposit speed coupled with an initially low powder feed meant that the deposition began to exhibit runaway conditions almost immediately. Over the course of the multi-pass wall deposition, the powder feed rate was increased twice to a final value of 25 $\frac{g}{min}$, at which point the deposition began to stabilize.

While inconvenient for creating constant input parameters during testing, the experments that were conducted demonstrated the importance of processing parameters on the quality of the component that was produced. In the lower sections of the third test's wall sample there are large closed pores apparent that approach 500 μm in diameter, which is very large in a multi-pass deposit that has a total width of just over 1 mm. While these imperfections are not apparent from the surface, they would severely degrade the performance of a production component fabricated under the test three conditions.

Experimental Determination of Cooling Rate

Using the measured Vickers micro-hardness for the single pass samples in all three tests and the series of regression fits detailed in Equations 28, 29, and 30, the cooling rates at specific points can be determined. The cooling rates as a function of position for the entire test area are plotted below on a log plot due to the wide range of cooling rates. The fastest cooling rates were seen in the deposit, which exceeded $2 \times 10^4 \frac{^{o}C}{minute}$. Slower cooling rates, approximately $800 \frac{^{o}C}{minute}$ existed below the deposited material.

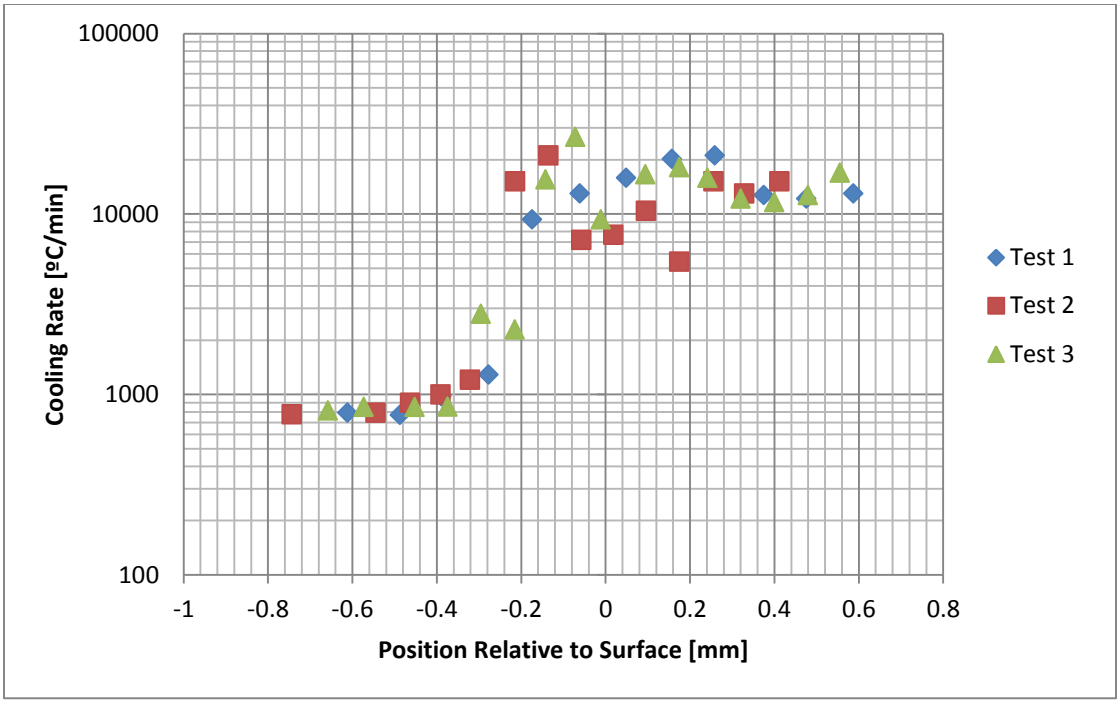

Figure 36: Calculated cooling rates $\left(\frac{ºC}{min}\right)$ as a function of position for entire deposit

The general trend of cooling rates at function of position follows the same trend as the hardness values, as is expected. There is a plateau around 800$\frac{ºC}{min}$ which correlates to the cooling rate at the edge of the HAZ, nearest the UBZ. This cooling rate occurs in the region ~400µm below the surface of the substrate. Beginning at about 400µm below the surface of the substrate, a rapid increase in cooling rate occurs in the heat affected zone of the deposit, which extends to 200µm below the substrate surface. At 200µm below the surface another plateau is clearly visible at a nominal value of ~15,000$\frac{ºC}{min}$. The high cooling rate plateau corresponds to the fusion zone in the deposition. The combination of the two cooling rate plateaus connected by a rapidly increasing zone leads to two important conclusions.

1. The high cooling rate plateau which extends ~200µm into the substrate corresponds to the total penetration of the fusion zone. This means that when passes are compounded, such as in the two-pass deposition, the top 200 µm *(at a minimum)* of the first pass *are* re-melted.

2. In the compounding of passes, the heat affected zone of the second deposit extends ~400 μm *(at a minimum)* into the first deposit. This means that the top half of the first deposition has its initial microstructure changed in either a re-melting process, or transformation of microstructure due to elevated solid state temperature.

When the measured cooling rates are superimposed on a continuous cooling curve for an AISI 1017-22 type steel, it is clear why only a mixture of martensite, bainite, and very small fraction of ferrite is observed.

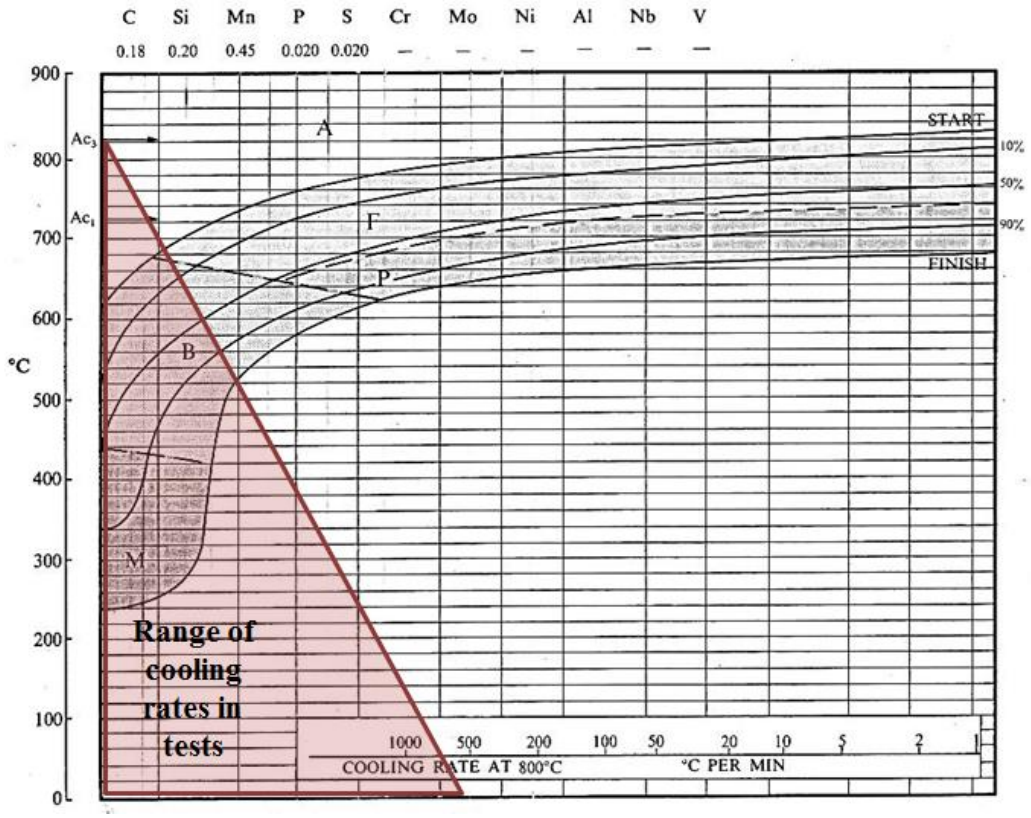

Figure 37: Calculated cooling rates of tests superimposed on 1017-22 CCT. Fig. modified from (23).

The hardness-derived cooling rates superimposed on the CCT diagram indicate why the pearlite spacing method for the measurement of cooling rate cannot be used in this case. The

deposition and the heat affected zone cooling kinetics are simply too fast for the formation of pearlite. To obtain pearlite, an even lower carbon content steel such as AISI 1008 steel would have to be used in place of 1018.

Comparison between Models and Experiments of Thermal Characteristics

COOLING RATES

To validate the analytical solution, it was compared to the experimental thermocouple temperature distribution. The comparison is shown below in Fig. 37.

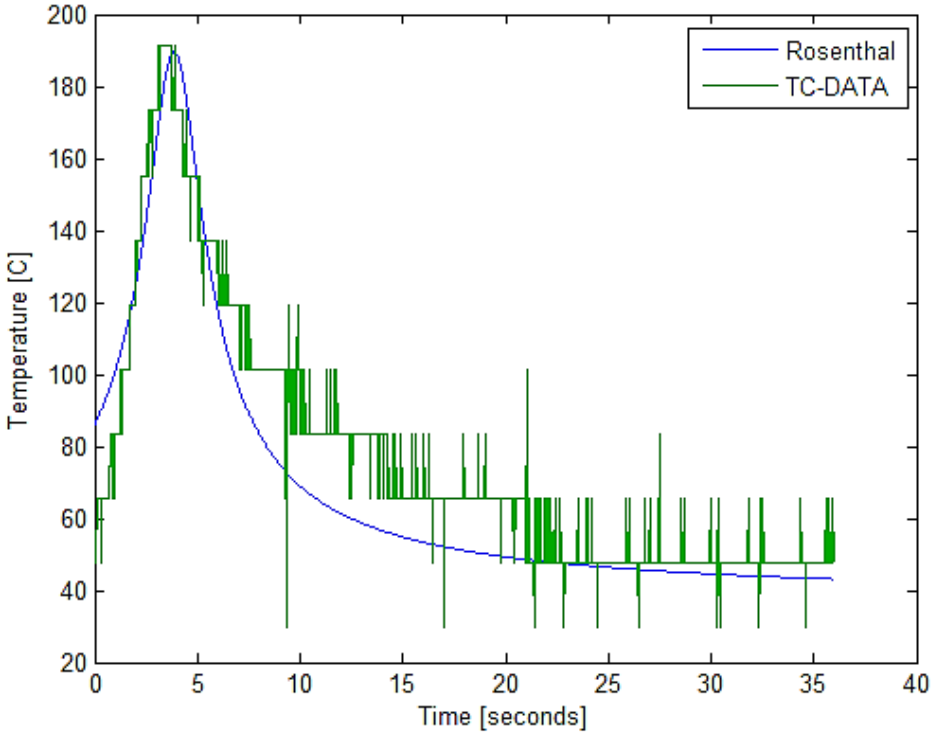

Figure 38: Comparison between analytical and experimental temperature transient

As previously mentioned the thermocouple data had to be transmitted wirelessly, requiring an analog signal. The discretization is very coarse; however the general trend is clear.

In comparison, the analytical model is slightly slower to heat and faster to cool. This can be explained by the convection of the hot shield gas onto the exposed thermocouple during deposition, which creates an artificially high localized ambient temperature that slightly increases the temperature of the very thin thermocouple wires. Predicted very well by the model is the peak temperature reached; which predicted the peak temperature within 3 ºC of the measured peak temperature.

Comparisons between the numerical calculations and the experimental thermocouple probes are shown in Fig. 39. The experimental thermocouple data is overlaid with the numerical results and shows the difference in temperature transients at two fixed locations.

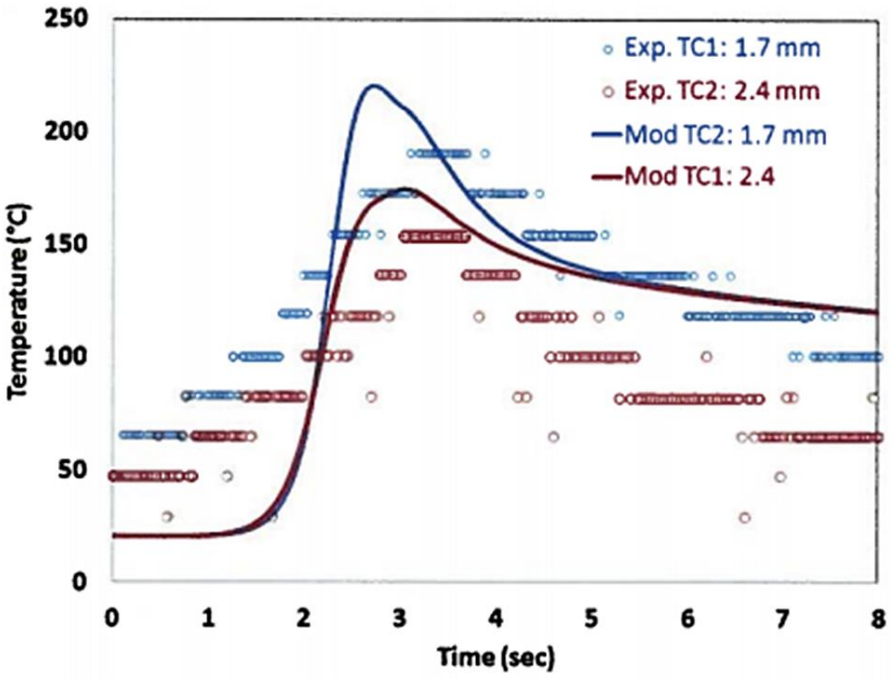

Figure 39: Comparison of Sysweld predicted values and experimental thermocouple data

The two thermocouples were each at varying distances from the centerline. Thermocouple 1*(shown in blue)* was at 1.7 mm from the centerline, while thermocouple 2

(shown in red) was further away at 2.4 mm from the centerline. There is an obvious difference in the measured and modeled peak temperatures. This can be explained by the time response of the thermocouples. Thermocouples rely on the Seebeck effect and thus there is a time lag which makes it impossible to resolve rapid changes in temperature. This has the effect of reducing the measured peak temperature and reducing temperature gradients, which is consistent with our findings relative to the numerical results.

PEAK TEMPERATURES

The validation of analytical peak temperature distribution can be done by comparing predicted locations for the A1 and A3 temperatures against the same locations determined from the metallographic analysis. As a reminder, in the locations where the metal peak temperature exceeds the A3 temperature, the entire previous microstructure will transform to austenite and upon cooling will form a mixture bainite and martensite due to the very high cooling rated. At the point where the peak temperature surpasses the A1 temperature all of the pearlite will be transform to austenite, which upon cooling will transform to a mixture of bainite and martensite. The ferrite will not be affected in this region since it is stable until the A3 temperature is reached. Thus, at the locations where the peak temperature was between the A1 and A3 temperatures, the pearlite will transform to martensite and bainite, but the pre-existing ferrite will remain unchanged. The A1 and A3 temperatures determined from the analytical model are superimposed on a micrograph of a specimen in Fig. 40.

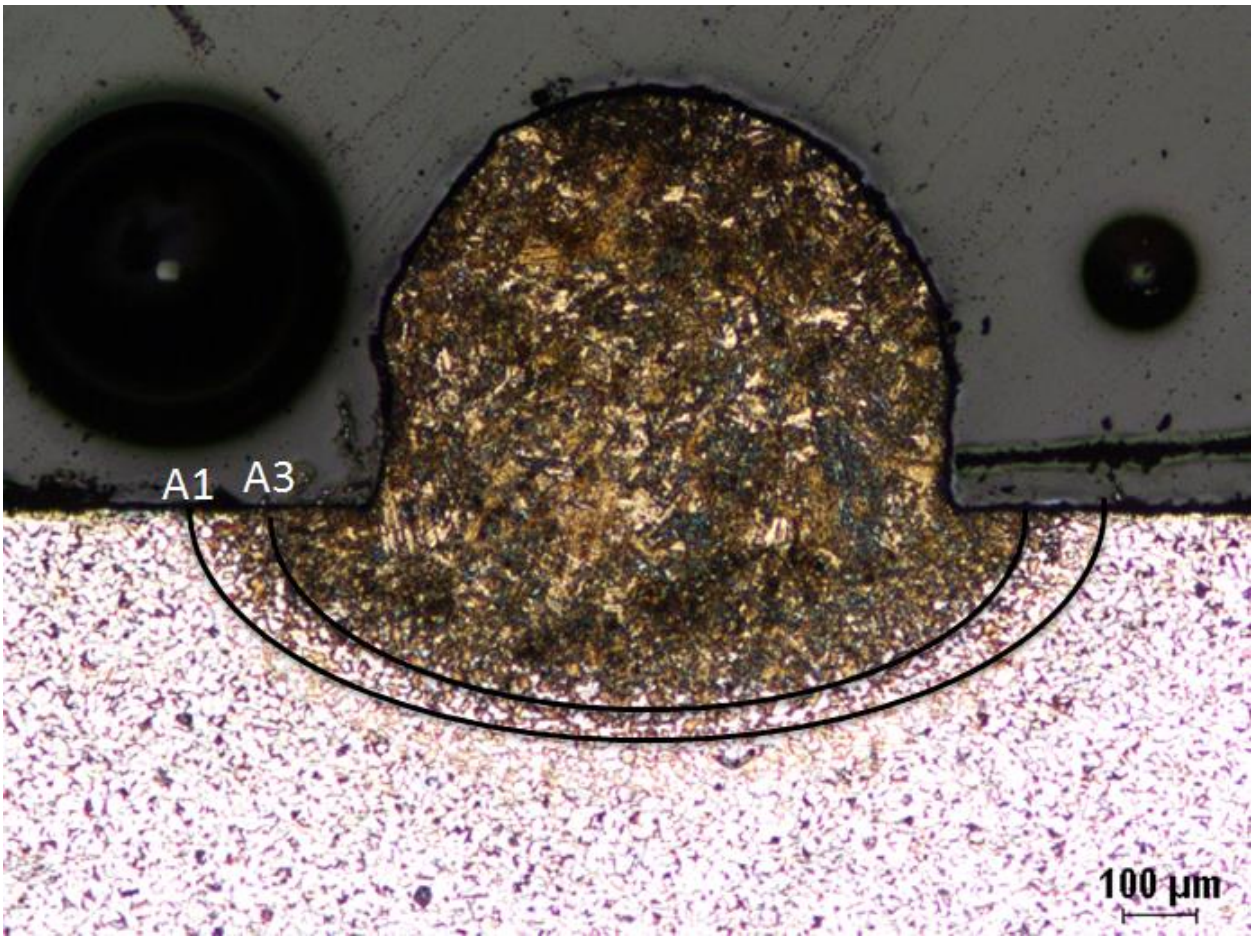

Figure 40: Analytical predictions of the A1 and A3 peak temperature for test 2 single pass deposition

From inspection of the superimposed A1 and A3 locations, it is clear that the location of the A3 peak temperature coincides with the extinction of any prior ferrite grains. Further from the location where A3 peak temperature was reached, there exists prior ferrite grains and re-transformed pearlite grains that exist now as a mixture of bainite and martensite, as expected. This validated the ability of the analytical modeled to accurately predict the location of the heat affected zones and the peak temperatures as a function of radius from the FZ.

A second comparison is shown in Fig. 41 for peak temperatures calculated from the numerical model and the metallographic cross sections. The idealized square deposition lines are for numerical simplicity; however the temperature in the heat affected zone should not be affect by this.

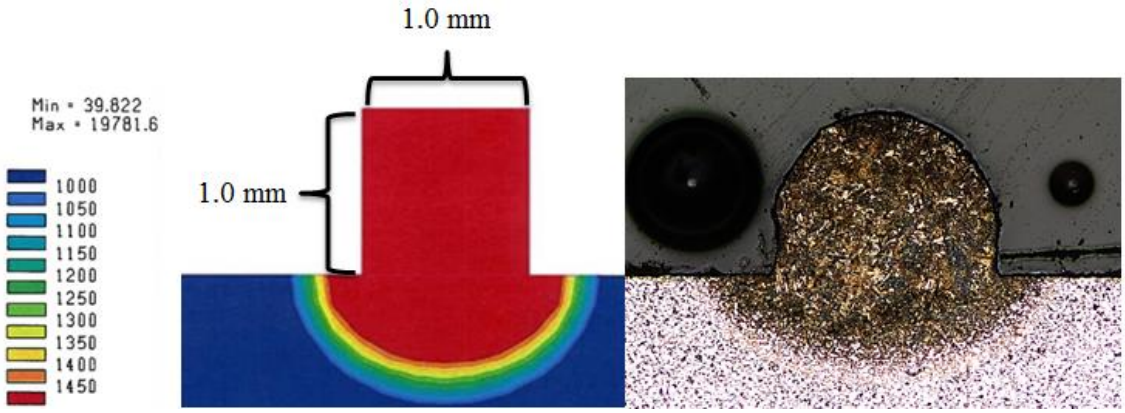

Figure 41: Cross sectional view with deposition direction out of the page showing a comparison of experimental and numerical fusion zones

It is clear from inspection that the fusion zone in the numerical model is nearly hemispherical, while the metallographic sample is a shallower ellipse. The penetration depth is 120 μm deeper in the numerical model than in the micrograph. This difference can be attributed the inability of the numerical model to account for the forced convention of the argon in the shield gas and powder feed system. Forced convection would cool the surface and drive a higher thermal gradient, and therefore a higher flux. The higher flux towards the surface would flatten the heat affected zone and the fusion zone would merge closer to the flattened ellipsoid seen in the metallographic sample.

The findings of this research are in general agreement with published literature findings. Through micro-hardness testing and subsequent linear regression analysis, it was experimentally determined that the cooling rate at 704 ºC of the deposits ranged from 13 $\frac{^{o}\mathrm{C}}{\mathrm{second}}$ to 250 $\frac{^{o}\mathrm{C}}{\mathrm{second}}$. These findings are within the range published by Thoma *et al.* (28) of 10^{1}-10^{5} $\frac{^{o}\mathrm{C}}{\mathrm{second}}$, but provide a narrower range that is useful. Numerical models using SysWeld showed similar qualitative trends as well as showing a significant extension of the fusion and heat affected zones into the substrate, although absolute quantitative agreement was not perfect.

The trend of measured micro-hardness values which showed two plateaus connected by a rapid increase in hardness in the heat affected zone, is similar to the observed micro-hardness trends obtained for low alloy AISI 4340 steel in published work by Bhattacharya *et al.* (12) and H13 tool steel by Mazumder *et al.* (2). Both literature hardness values approached 200 H_V in the substrate; however both AISI 4340 and H13 tool steel can form fully martensitic microstructure much easier due to their respective alloying contents of nickel, chromium, molybdenum, and vanadium. Therefore in the deposit, where cooling rates are much higher, the hardnesses approached 600 H_V in these materials. Elevated hardness in AISI 4340 and H13 tool steel is to be expected, as compared to AISI 1018, due to significantly higher hardenabilities of both steels.

Unique to this study was the incorporation of analytical, numerical, and experimental techniques to quantify the same process, with the same material, under different input conditions. The convergence of all three techniques was demonstrated for AISI 1018 steel and should be applicable to other materials.

VIII. CONCLUSIONS

This research was conceptualized to independently investigate the numerical, analytical, and experimental aspects of DMD, and to see if there would be convergence between these different methods. An analytical model was developed which can predict temperature distributions inside of the substrate during DMD. A commercial code was used to model the melt pool, and obtain temperature profiles at points of interest. Instrumented experiments were then done to obtain both *in-situ* and *post-mortem* temperature data.

The experiments demonstrated that the peak temperatures and cooling rates for single pass depositions of AISI 1018 powder on AISI steel plates could accurately modeled. Locations of A1 and A3 peak temperatures in the substrate were predicted and cooling rates of 13 $\frac{^{o}C}{\text{second}}$ to 250 $\frac{^{o}C}{\text{second}}$ were modeled in the FZ and HAZ regions of the deposit. Comparisons between the analytical model and the experimentally determined microstructures and hardness values showed excellent agreement. Comparisons with the numerical model and the experimental microstructures showed good qualitative agreement but there were some systematic differences that were attributed to the inability of the numerical model to account for the forced convention of the argon in the shield gas and powder feed system.

This research demonstrates the ability to integrate analytical and numerical physics based models to characterize the direct metal deposition process. In principle it shows that while additive manufacturing is a re-conceptualization of manufacturing, the fundamental science that is required to understand direct metal deposition exists in other areas of engineering, material science, and computing. These concepts and techniques need only to be modified to account for the physics of DMD.

The next step understanding DMDS is being able to characterize temperature regimes inside the deposit itself, as well as more complicated geometries. Immediate future work will include the application of these models to new materials, and assessing its capability to drive

input parameters such as laser power, laser speed, and powder feed rate; as well as the resulting deposition morphology.

IX. APPENDIX I: MICROGRAPHS

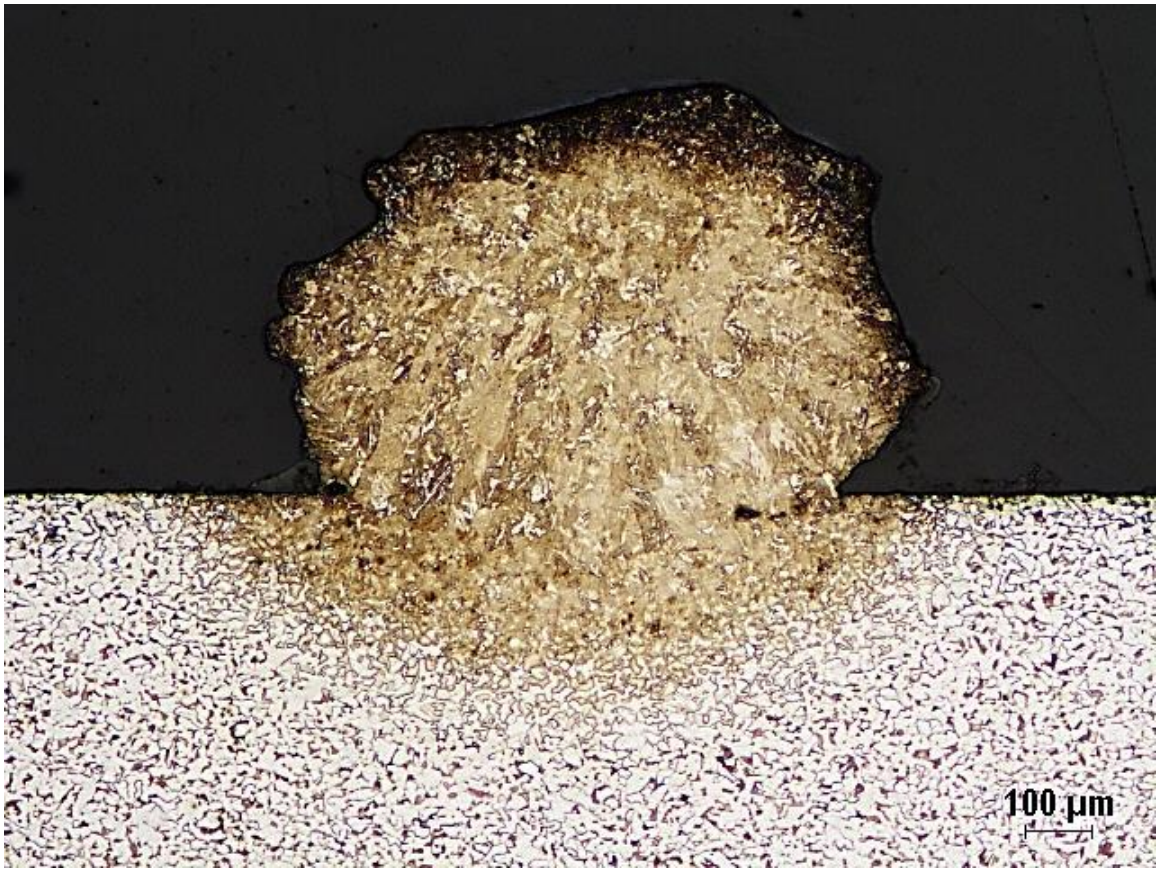

Figure 42: 10× micrograph of the crosssection of the single pass deposition from test series one

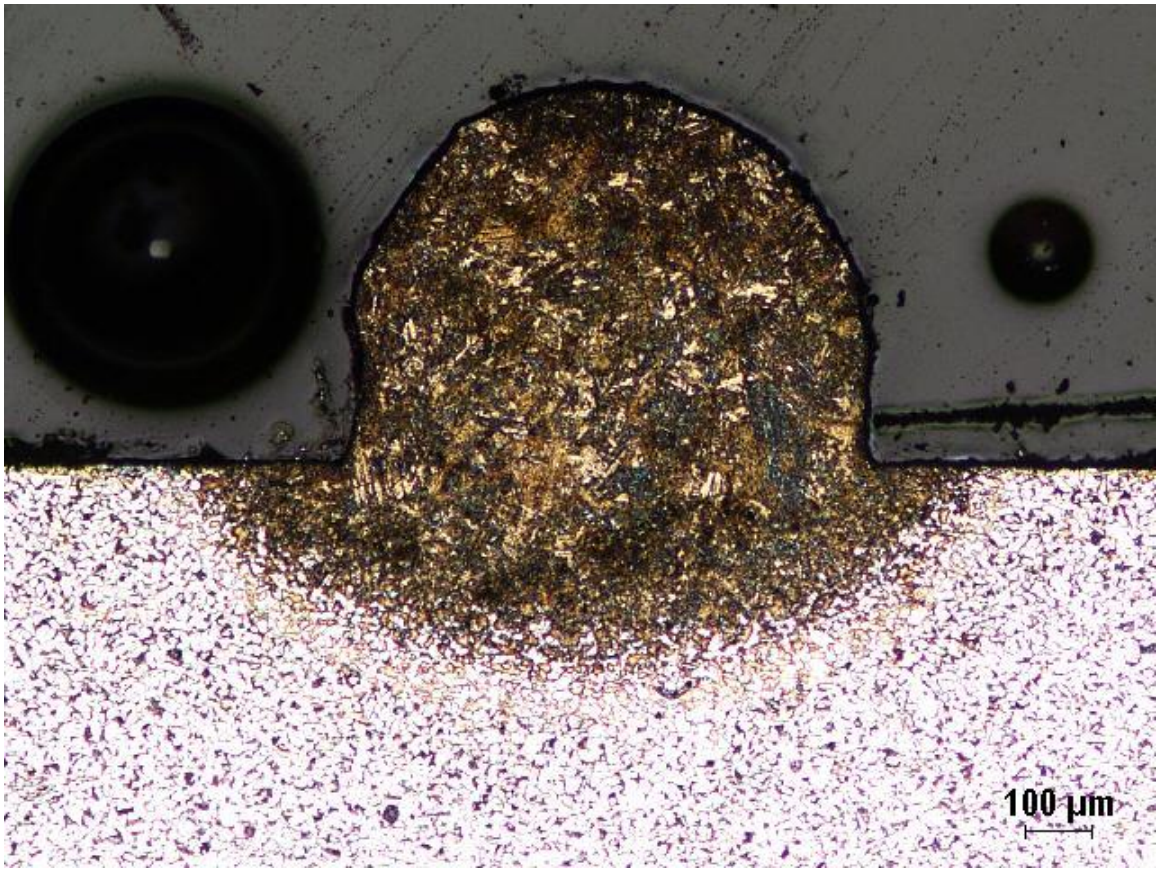

Figure 43: 10× micrograph of the crosssection of the single pass deposition from test series two

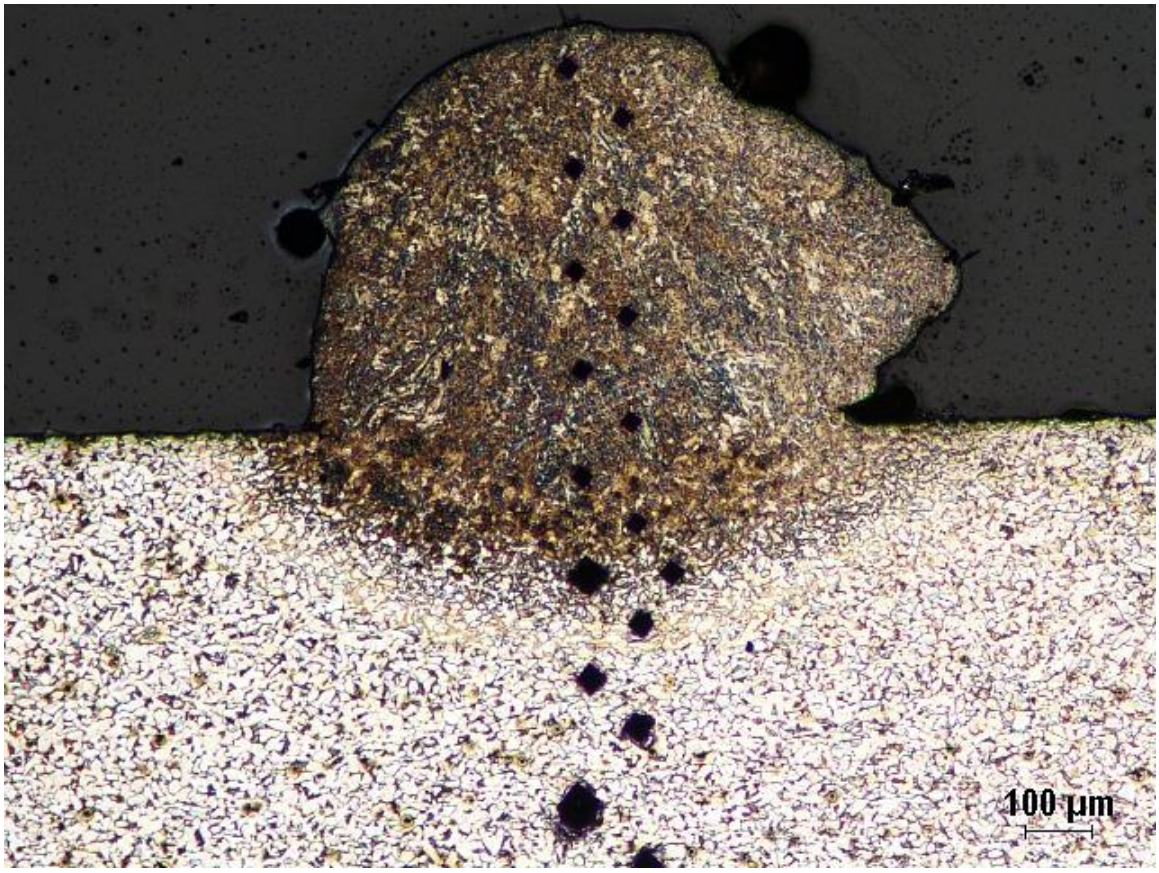

Figure 44: 10× micrograph of the crosssection of the single pass deposition from test series three. With Vickers microhardness test array

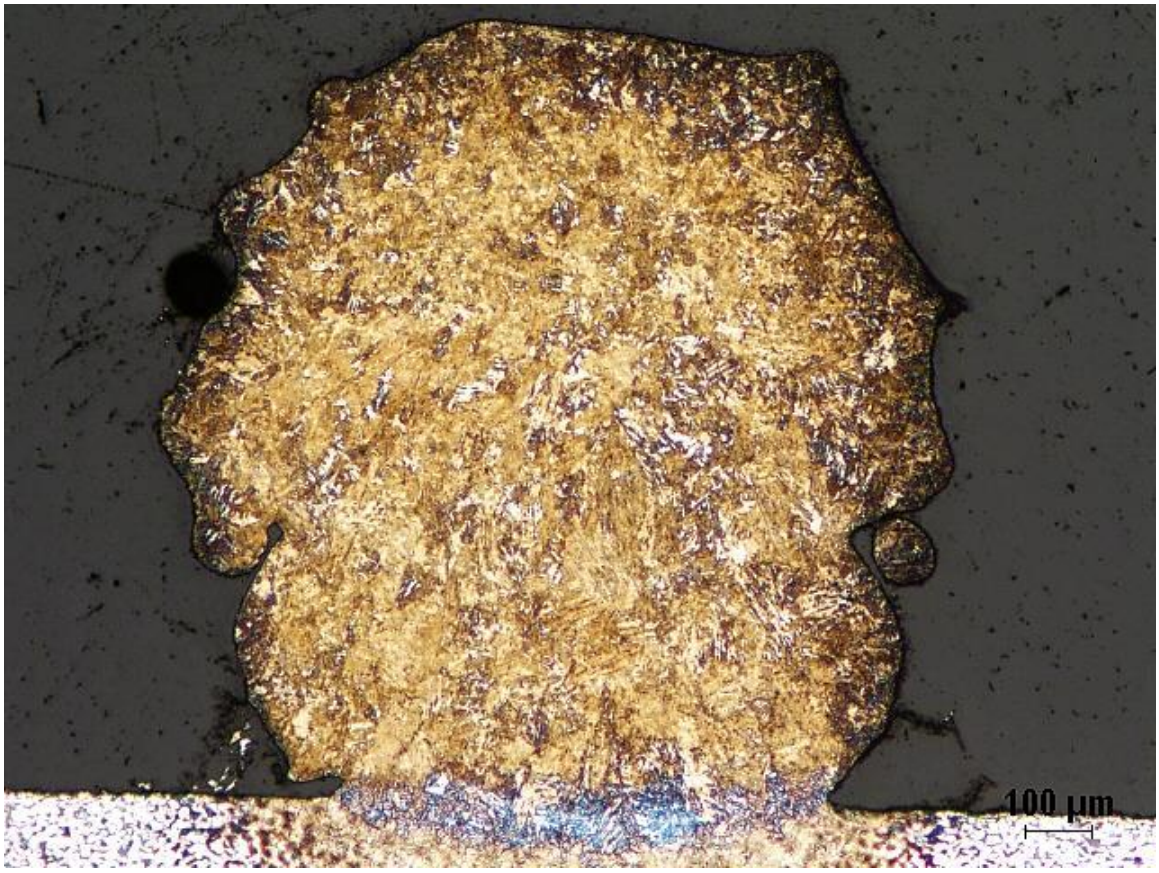

Figure 45: 5× micrograph of the crosssection of the two pass deposition from test series one

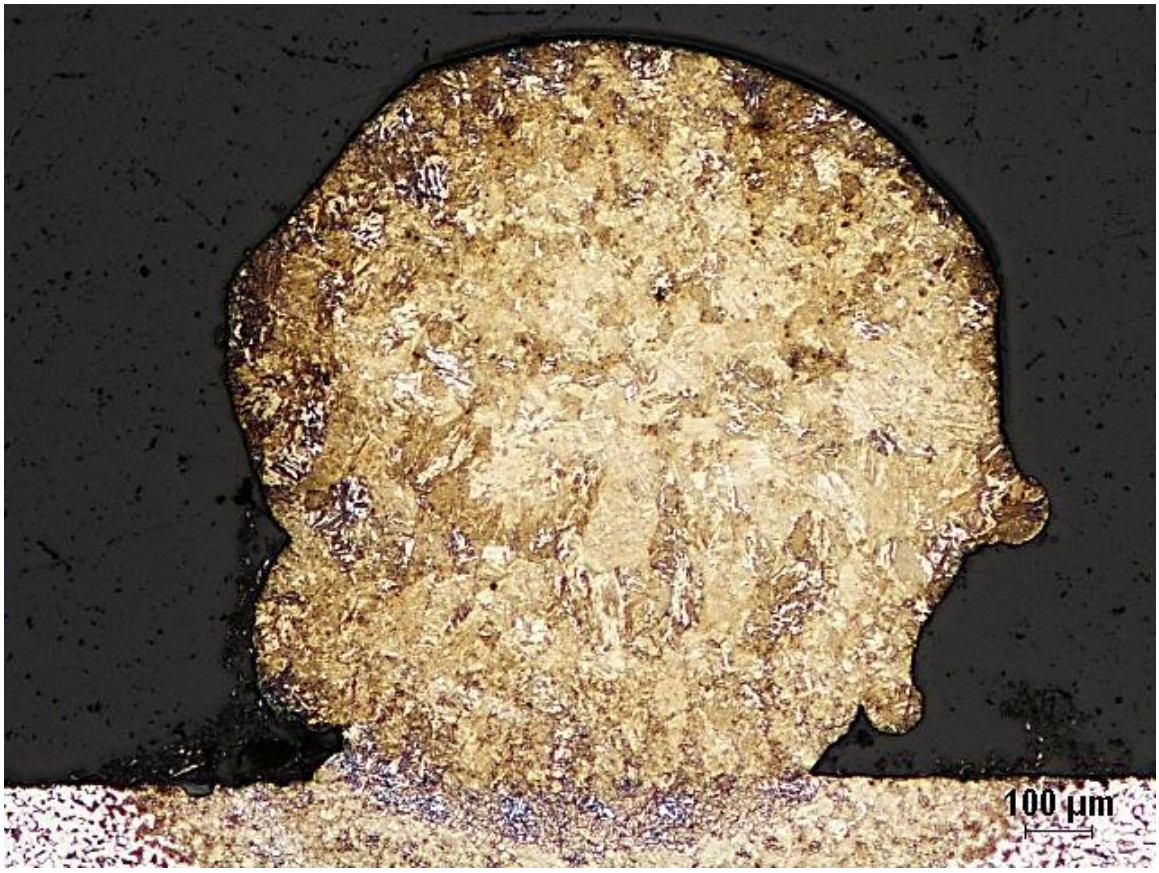

Figure 46: 5× micrograph of the crosssection of the two pass deposition from test series two

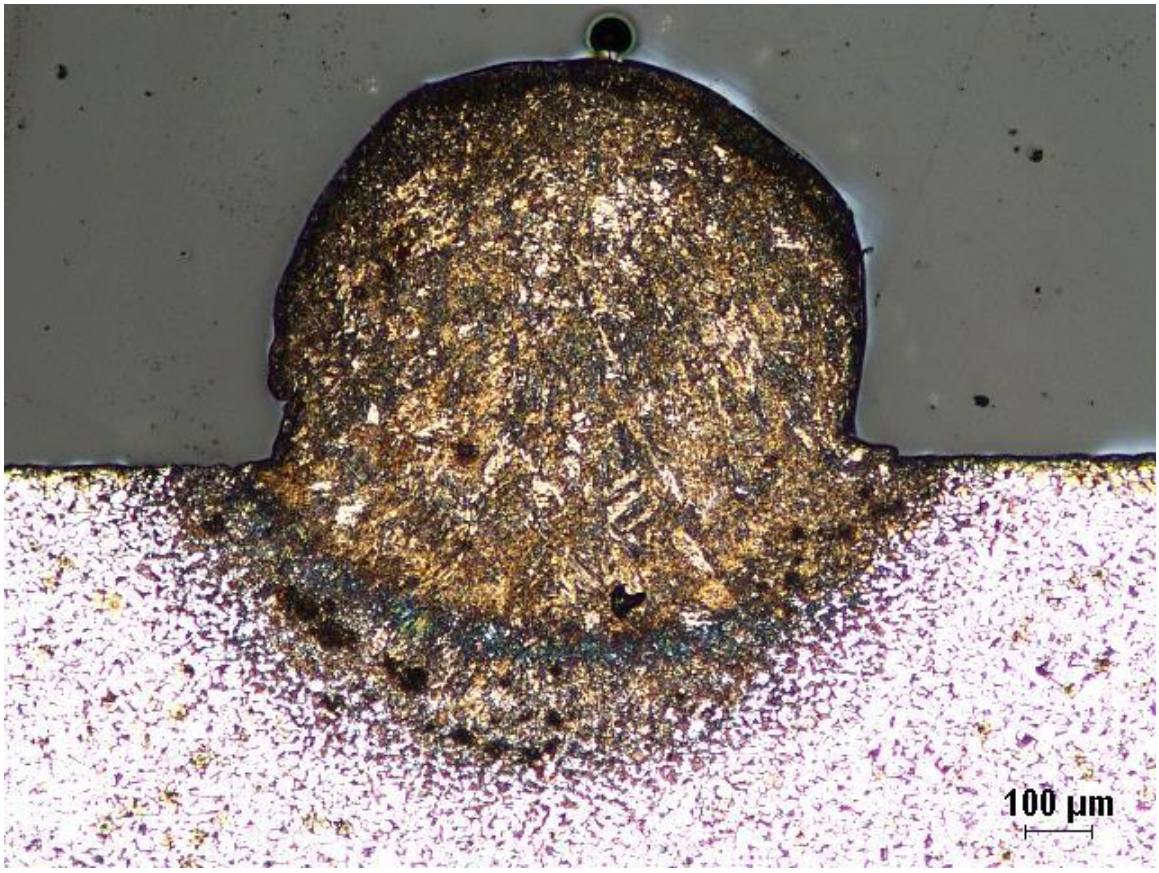

Figure 47: 5× micrograph of the crosssection of the two pass deposition from test series three

Figure 48: Stereo-microscope cross section image of the one inch wall deposition from test series one

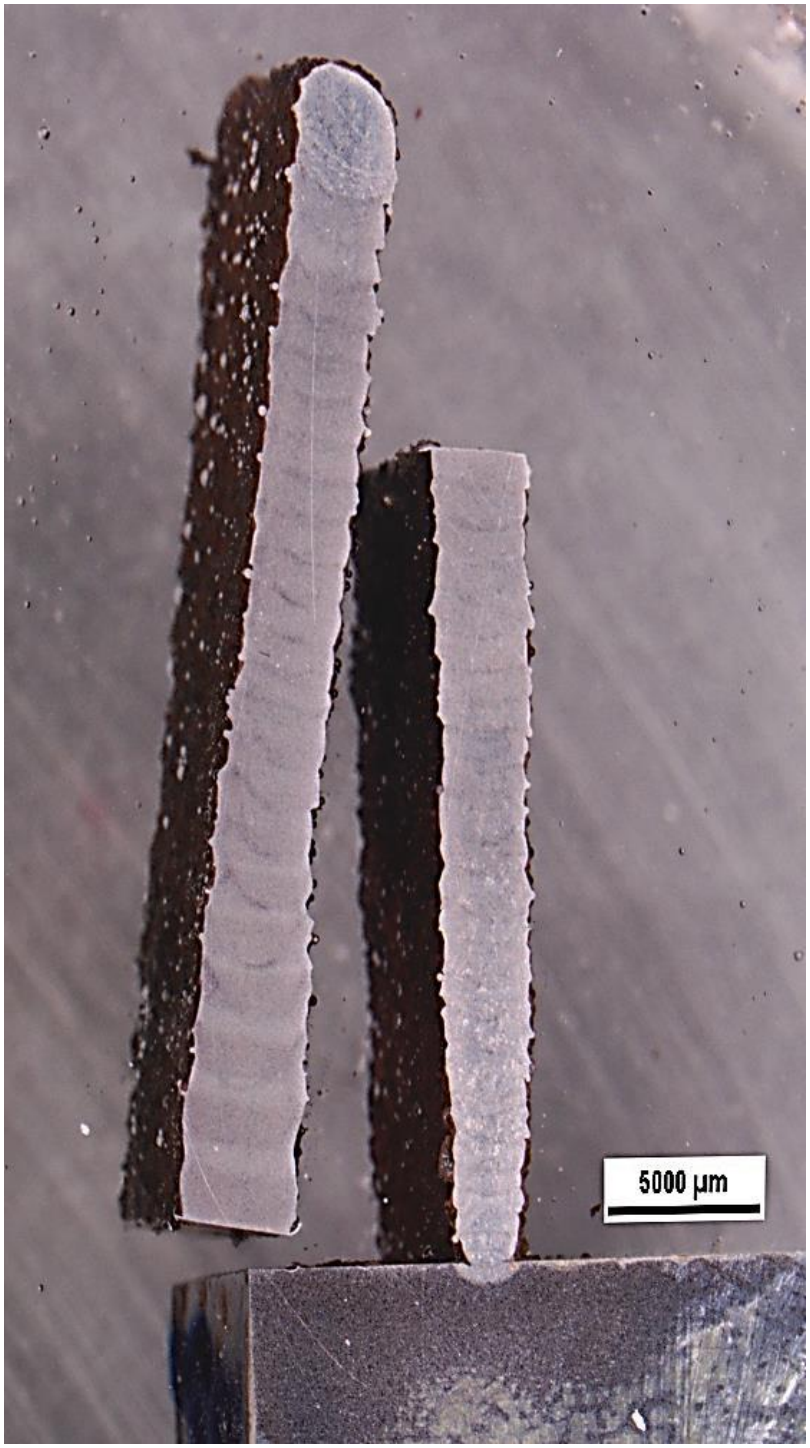

Figure 49: Stereo-microscope cross section image of the one inch wall deposition from test series two. The sample was cut along its height so that it could be mounted for polishing.

Figure 50: Stereo-microscope cross section image of the one inch wall deposition from test series three

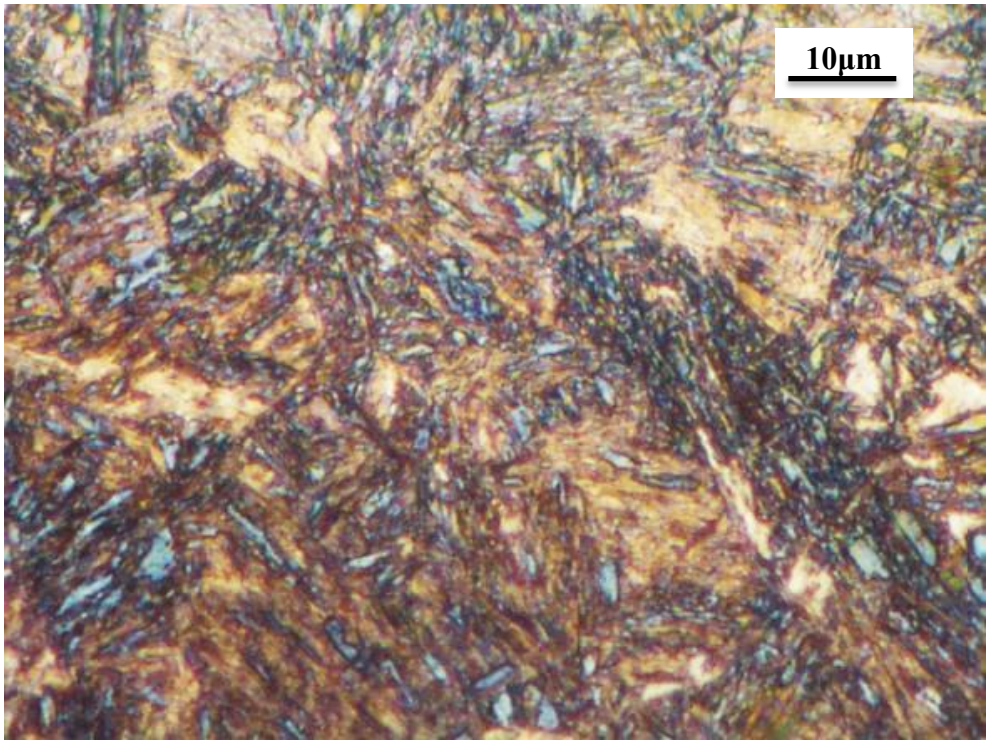

Figure 51: Enlarged 100× micrograph from Fig. 30 (a)

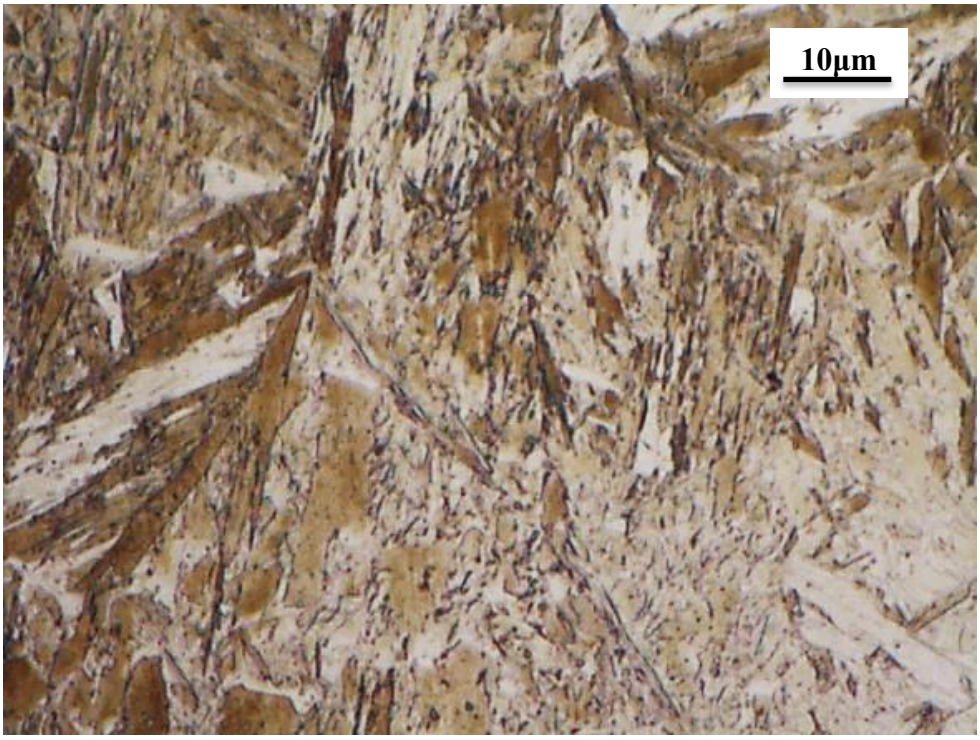

Figure 52: Enlarged 100× micrograph from Fig. 30 (b)

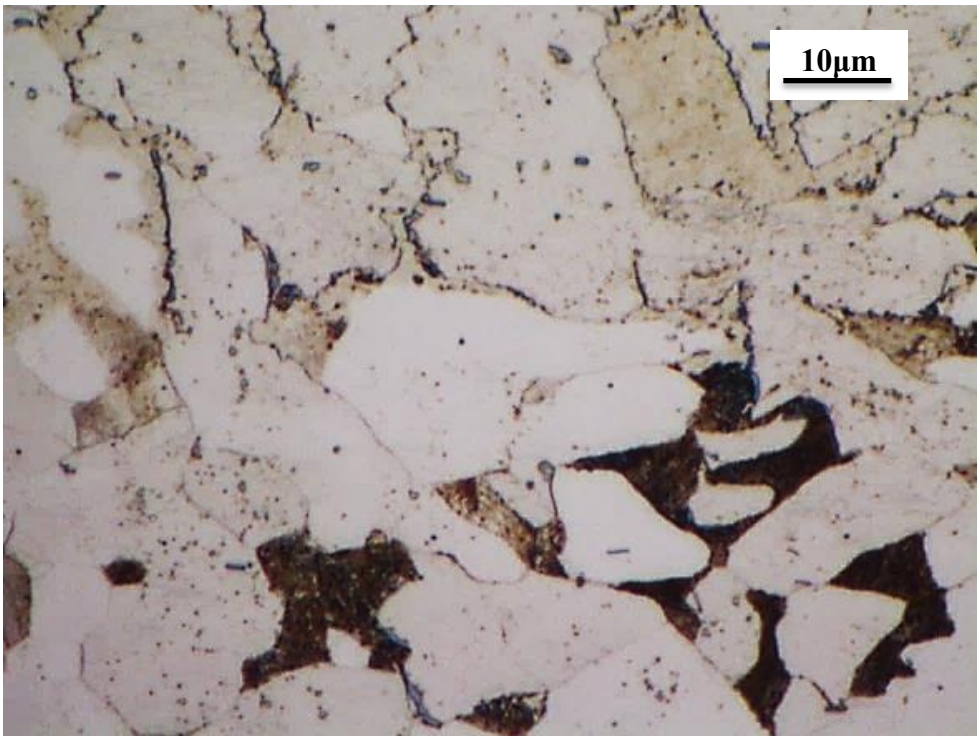

Figure 53: Enlarged 100× micrograph from Fig. 30 (c)

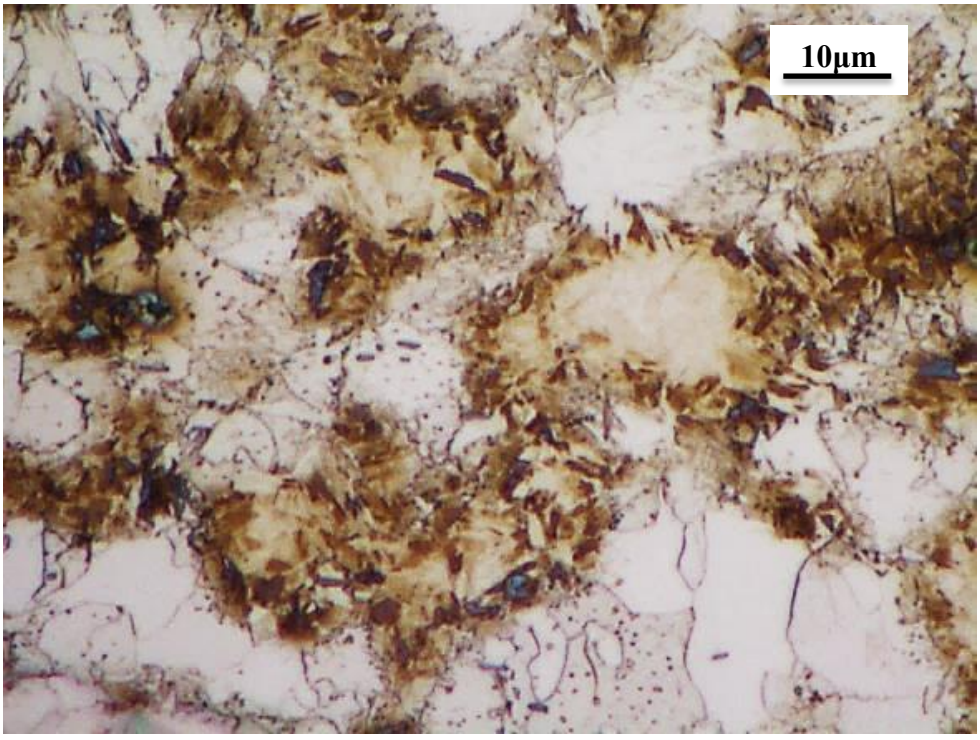

Figure 54: Enlarged 100× micrograph from Fig. 30 (d)

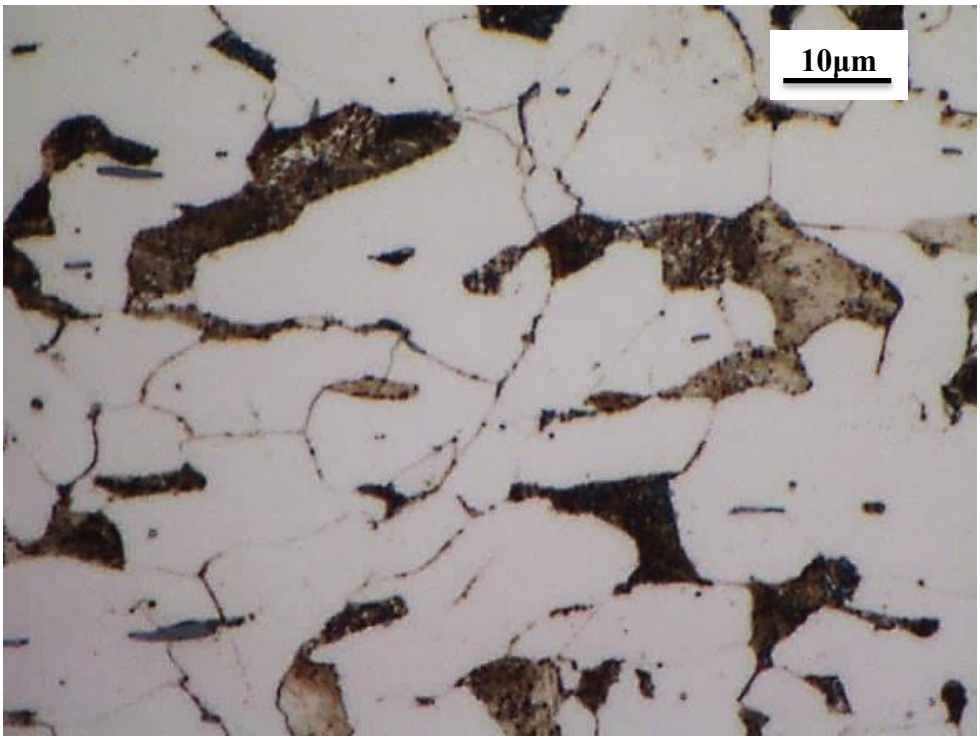

Figure 55: Enlarged 100× micrograph from Fig. 30 (e)

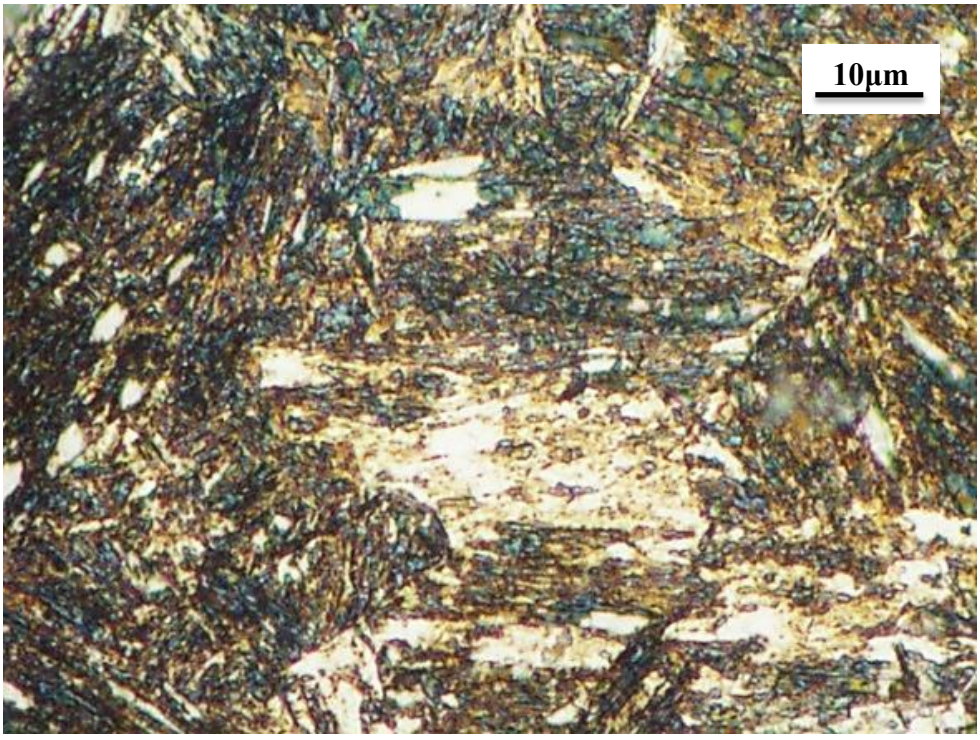

Figure 56: Enlarged 100× micrograph from Fig. 31 (a)

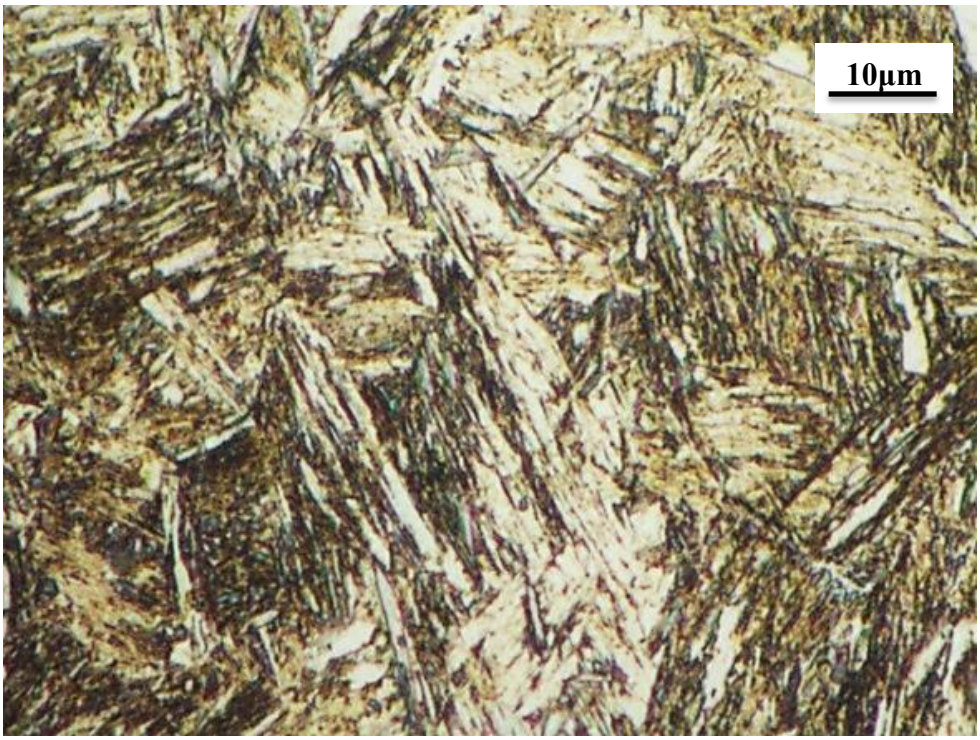

Figure 57: Enlarged 100× micrograph from Fig. 31 (b)

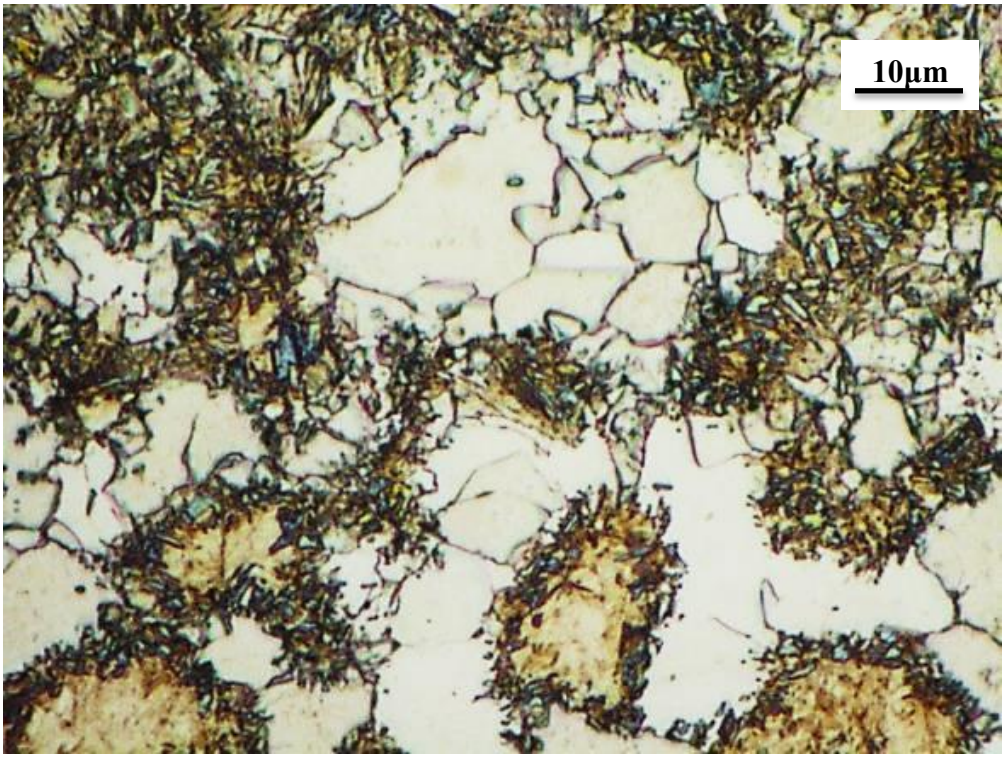

Figure 58: Enlarged 100× micrograph from Fig. 31 (c)

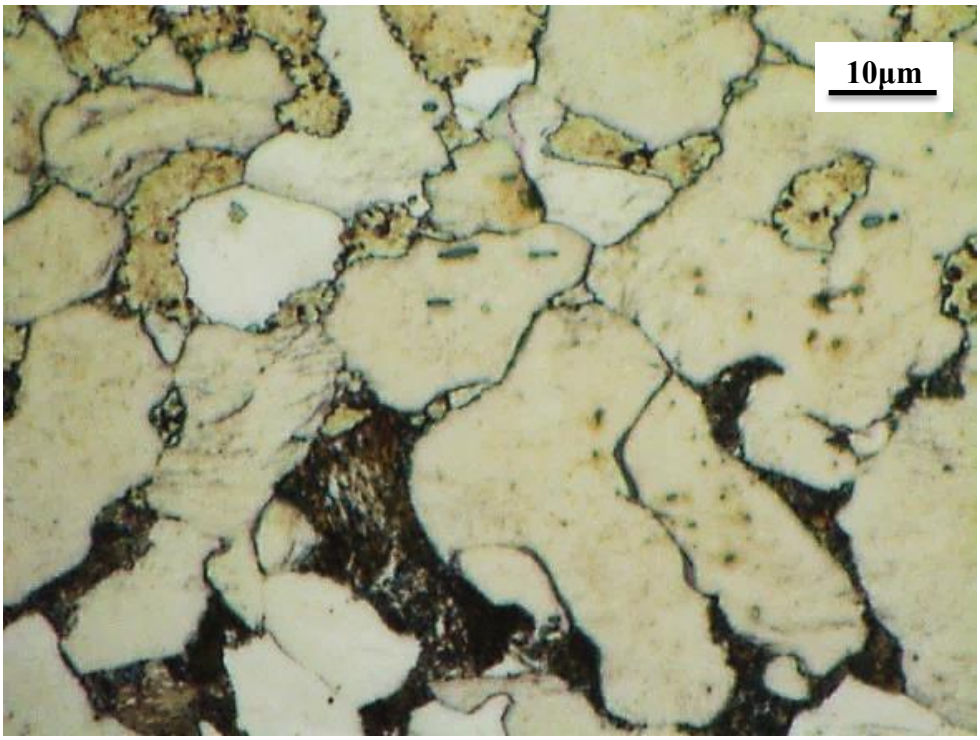

Figure 59: Enlarged 100× micrograph from Fig. 31 (d)

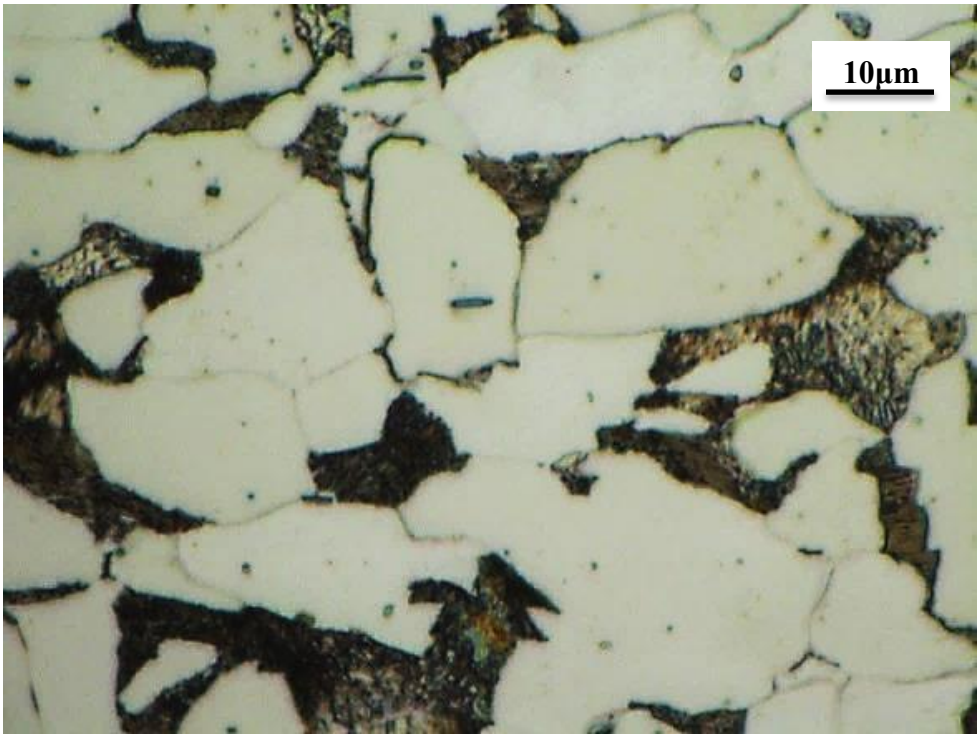

Figure 60: Enlarged 100× micrograph from Fig. 31 (e)

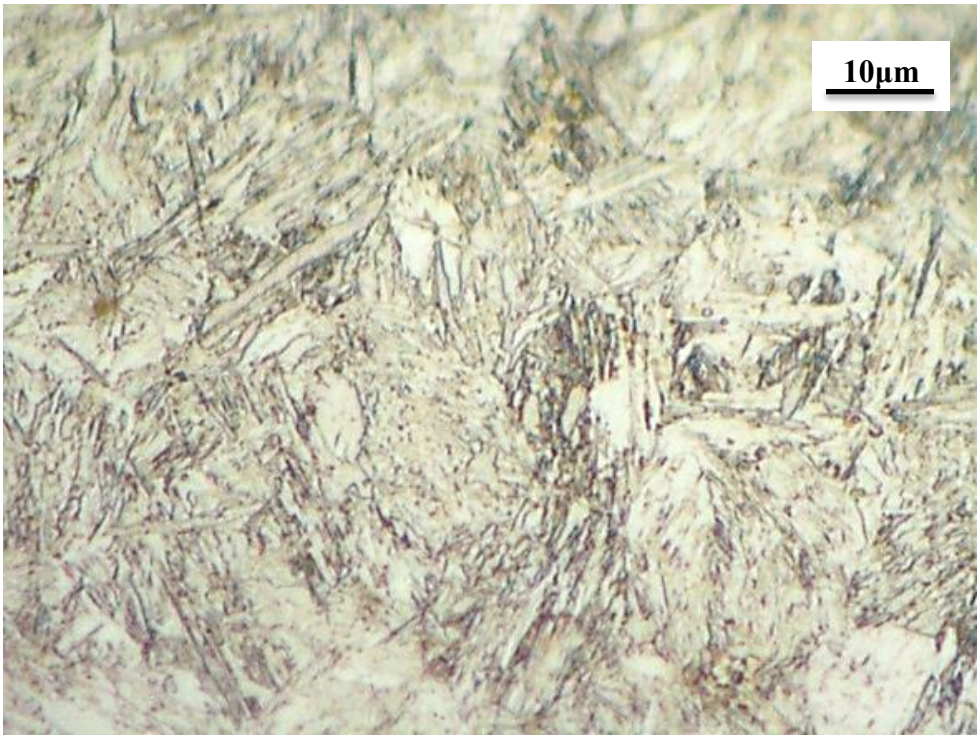

Figure 61: Enlarged 100× micrograph from Fig. 32(a)

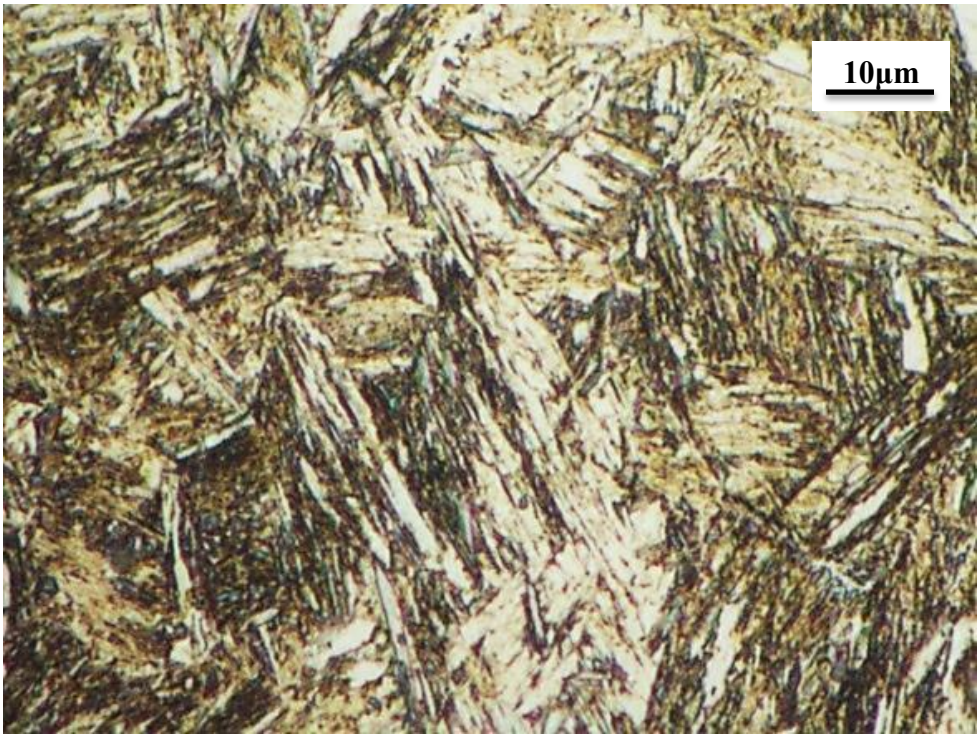

Figure 62: Enlarged 100× micrograph from Fig. 32 (b)

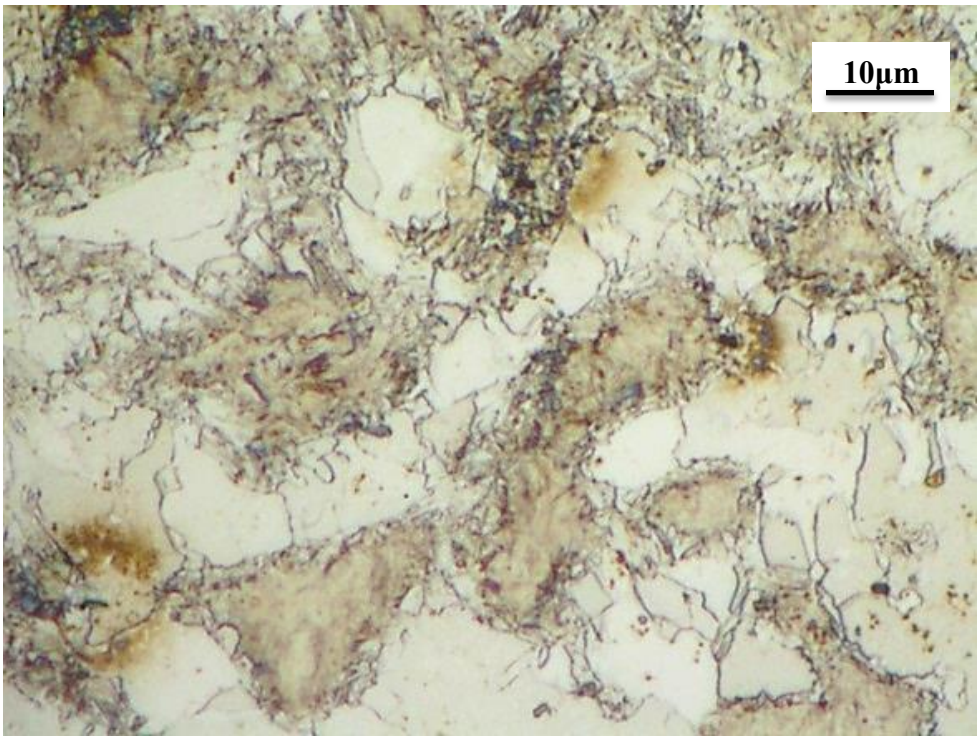

Figure 63: Enlarged 100× micrograph from Fig. 32 (c)

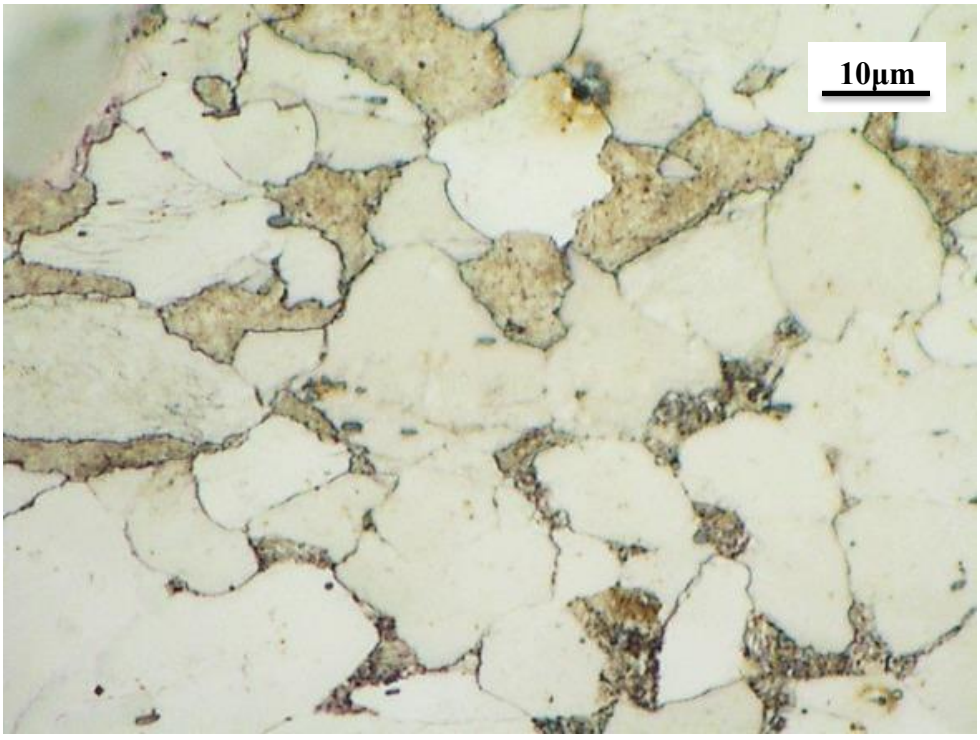

Figure 64: Enlarged 100× micrograph from Fig. 32 (d)

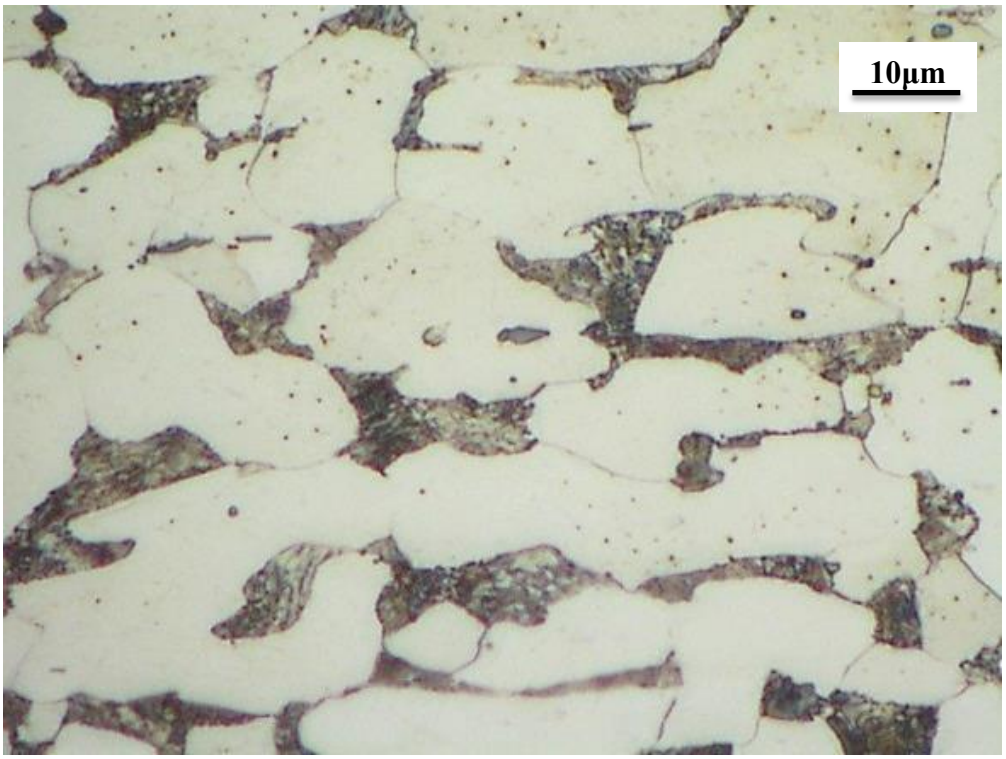

Figure 65: Enlarged 100× micrograph from Fig. 32 (e)

APPENDIX II: SysWeld Numerical Model Figures

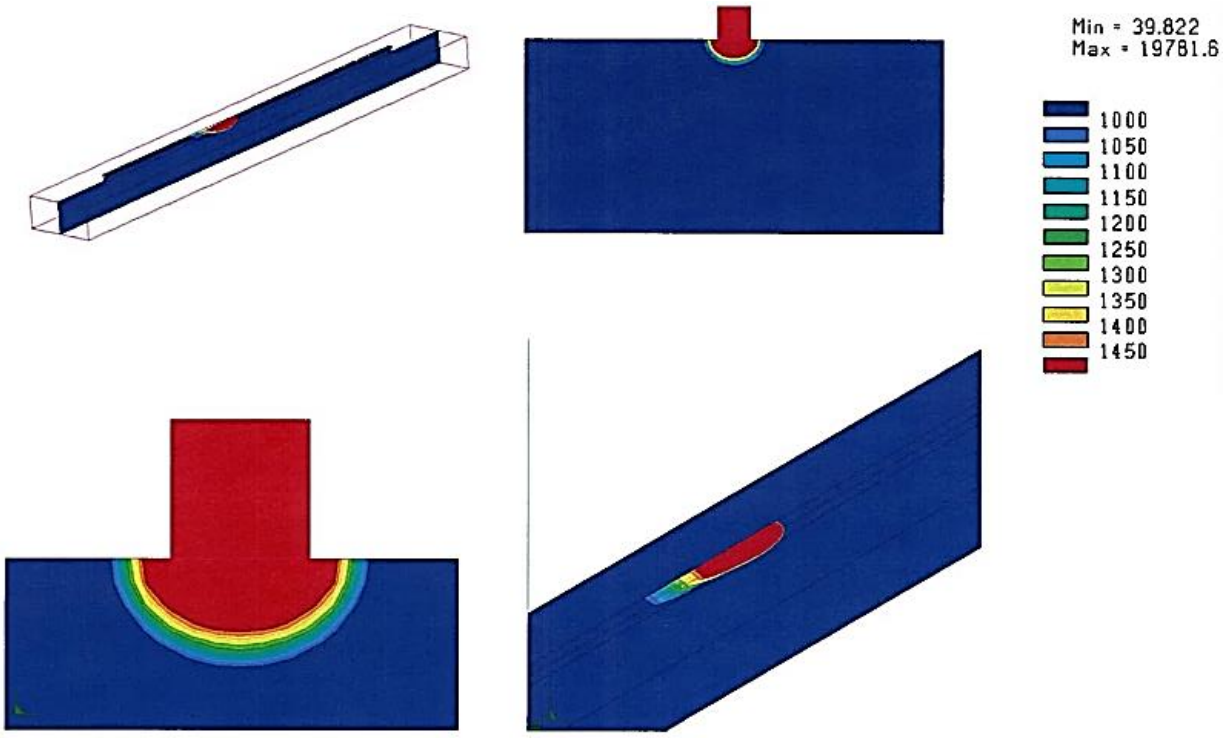

Figure 66: Additional SysWeld molten pool cross sections

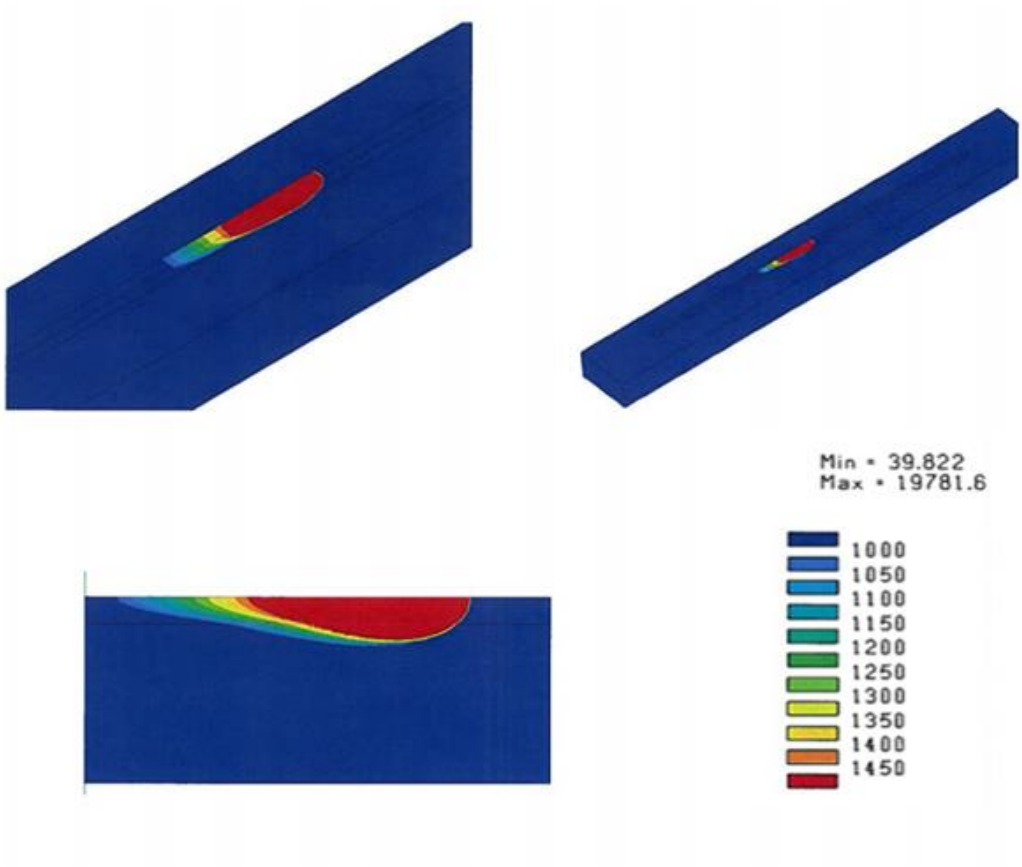

Figure 67: SysWeld molten pool cross sections

X. APPENDIX III: MATLAB CODES

Cooling Rate as a Function of Time

```
%An analytical model of energy distribution in direct metal deposition

%Moving Heat Source models as a moving Point source in 3D from
% Daniel Rosenthal

%Initial Conditions%
ap=.5 ;              %Powder Coupling Eff
as=.5;               %Substrate Coupling Eff
B=900;               %Melt Pool Conduction Calibration Constant
D0= 8.0E-3;          %meters Initial Beam and Powder diameters
D1= 1.0E-3;          %meters Beam diameter at surface
cp = 600.0;          %J/kgK Specific Heat
epsilon= 0.4;        %Emmissivity of melt pool
h= 1E3;              %W/m2K Convective HTC
hfg = 6.8E6;         %J/kg Latent heat of Vaporization
k=51.9;              %W/mK Thermal Conductivity
L= 0.0012;            %m melt pool length
ldeposit = .0762;    %m
Lb= 1.6E-2;          %Beam-powder interaction distance
mdot= 1.08E-4;       %mass flow of powder
P0=290;              %Watts Laser Power
r= 5.5e-5;           %meters Radius of Powder
rho= 7850;           %kg/m3 density of material system
sigma= 5.67E-8;      %W/m2K4 Boltzman Constant
Tm= 1735;            %K Solidus Temp
T0 = 310.0;          %K Ambient Temperature
Vp= 1.4;             %meters/sec powder velocity
vsource = .002116; %m/s Source Velocity
xTC = .0082 ;        %meters x-Location along deposit of TC
yTC = [.0005 0.001 0.0015 0.002 0.003 0.004 0.005];       %meters y-Location
from centerline on substrate surface
b=numel(yTC);
zTC = 0.000;       %meters z-Location depth into substrate
z=.0162;             %meters Axial distance below nozzle

%Initial Calculations

deposittime=ldeposit/vsource;
alpha = k/ (rho *cp) ; %m2/s
tzero = T0-273.15; %Celcius
t = 0:.01:deposittime;
numofsteps = numel(t);
a = numofsteps;
step = .0005; %mm
w = xTC - (vsource*t);
RM = zeros(1,a);
stepm = step *1000;
vsourcem = vsource*1000;
tenpassheight = step * 100;
xposs = xTC*1000;
```

```
yposs = yTC*1000;


%Powder Laser Interaction%
Fv = 4*mdot/(pi()*rho*Vp*(D0^2));
Ab= pi()*((D0*Lb*D0*z)+(D1*z))/(4*(Lb^2));
Pap1= ((3*ap*mdot*D1*Lb*P0)/(pi()*r*Vp*rho*(D0^3)));%Inflight Absorption
Prp1= ((3*(1-ap)*mdot*D1*Lb*P0)/(pi()*r*Vp*rho*(D0^3))); %Inflight reflection
Pap2= ((3*ap*mdot*(D0-D1)*Lb*P0)/(pi()*r*Vp*rho*(D0^3)));%Inflight Absorption
Prp2= ((3*(1-ap)*mdot*(D0-D1)*Lb*P0)/(pi()*r*Vp*rho*(D0^3)));%Inflight
reflection
Psum= Pap1+Prp1+Pap2+Prp2;
P1= as*(P0-Psum)+Pap1;

%Temperature%
Tpeak = Tm + (P1/(2*pi()*k*D1));
Tmean = Tm + (P1/(4*pi()*k*D1));

%Energy Flow%
Q1C1= (pi()*(D1^2)*k*B)/2;
Q1C2= (pi()*D1*L*k*B)/2;
Q2C1= (pi()*(D1^2)*h)/2;
Q2C2= (pi()*D1*L*h)/2;
Q3C1= (pi()*(D1^2)*epsilon*sigma)/2;
Q3C2= (pi()*D1*L*epsilon*sigma)/2;

Q2= (Q2C1*(Tpeak-T0))+(Q2C1*(Tmean-T0));
Q3= (Q3C1*((Tpeak^4)-(T0^4)))+(Q3C1*((Tmean^4)-(T0^4)));
Q4= (28295*pi()*(D1^2)*hfg*(exp(-
18836/Tpeak)/(sqrt(Tpeak))))+(28295*pi()*(D1*L)*hfg*(sqrt(2)*exp(-
37672/(Tpeak+Tm))/ (sqrt(Tpeak+Tm))));
Q1= P1-Q2-Q3-Q4;
Qsum= Q1+Q2+Q3+Q4;

%Energy Losses

Powderloss= (Prp1+Pap2+Prp2)/P0;
AbsinSurf=P1/P0;
Reflected= ((P0-P1)/P0)-Powderloss;
CondtoSub= Q1/P0;
ConvPoolLoss=Q2/P0;
RadPoolLoss=Q3/P0;
VapPoolLoss=Q4/P0;
SurfRef=P0-P1-Powderloss;
Losstotal= Powderloss+Reflected+CondtoSub+ConvPoolLoss+VapPoolLoss;
Eff=P1/P0;

EnergyBal1= ['%PO Lost to Powder =', num2str(Powderloss)];
EnergyBal2= ['%P0 Reflected off Surface =', num2str(Reflected)];
EnergyBal3= ['%PO Conducted into Substrate=' , num2str(CondtoSub)] ;
EnergyBal4= ['%PO Convected from Pool=' ,num2str(ConvPoolLoss)];
EnergyBal5= ['%P0 Evaporated from Pool=' ,num2str(VapPoolLoss)];
EnergyTotal= ['Energy total=', num2str(Losstotal)];

disp(EnergyBal1);
```

```
disp(EnergyBal2);
disp(EnergyBal3);
disp(EnergyBal4);
disp(EnergyBal5);
disp(EnergyTotal);

%Measured Results%
exptime= 0: 0.03125:36.0;
T1 = [47.60300253   47.60300253 47.60300253 65.39308634 65.39308634
65.39308634 65.39308634 65.39308634 65.39308634 65.39308634 47.60300253
65.39308634 65.39308634 65.39308634 65.39308634 65.39308634 65.39308634
65.39308634 65.39308634 65.39308634 65.39308634 65.39308634 65.39308634
65.39308634 83.25498697 83.25498697 83.25498697 65.39308634 83.25498697
83.25498697 65.39308634 83.25498697 83.25498697 83.25498697 83.25498697
83.25498697 83.25498697 83.25498697 83.25498697 83.25498697 101.1826707
83.25498697 83.25498697 101.1826707 101.1826707 101.1826707 101.1826707
101.1826707 101.1826707 101.1826707 101.1826707 101.1826707 101.1826707
101.1826707 101.1826707 101.1826707 119.1672559 119.1672559 119.1672559
119.1672559 119.1672559 119.1672559 119.1672559 137.1978206 119.1672559
137.1978206 137.1978206 137.1978206 137.1978206 137.1978206 137.1978206
137.1978206 137.1978206 155.2621103 155.2621103 155.2621103 155.2621103
155.2621103 155.2621103 155.2621103 155.2621103 155.2621103 155.2621103
173.34715   155.2621103 173.34715   173.34715   173.34715   173.34715
155.2621103 173.34715   173.34715   173.34715   173.34715   173.34715
173.34715   173.34715   173.34715   173.34715   191.4397684 173.34715
173.34715   191.4397684 191.4397684 191.4397684 191.4397684 191.4397684
191.4397684 191.4397684 191.4397684 191.4397684 191.4397684 191.4397684
191.4397684 191.4397684 191.4397684 191.4397684 191.4397684 191.4397684
173.34715   173.34715   173.34715   173.34715   173.34715   191.4397684
173.34715   173.34715   173.34715   173.34715   173.34715   173.34715
173.34715   173.34715   173.34715   173.34715   173.34715   173.34715
173.34715   155.2621103 155.2621103 155.2621103 155.2621103 173.34715
155.2621103 155.2621103 155.2621103 155.2621103 155.2621103 155.2621103
137.1978206 155.2621103 155.2621103 155.2621103 155.2621103 155.2621103
155.2621103 155.2621103 155.2621103 155.2621103 155.2621103 155.2621103
137.1978206 137.1978206 137.1978206 155.2621103 137.1978206 137.1978206
137.1978206 137.1978206 119.1672559 137.1978206 137.1978206 137.1978206
137.1978206 137.1978206 137.1978206 137.1978206 137.1978206 137.1978206
137.1978206 137.1978206 137.1978206 137.1978206 137.1978206 137.1978206
137.1978206 137.1978206 137.1978206 137.1978206 137.1978206 137.1978206
137.1978206 119.1672559 119.1672559 137.1978206 119.1672559 119.1672559
119.1672559 119.1672559 119.1672559 137.1978206 119.1672559 119.1672559
119.1672559 119.1672559 119.1672559 137.1978206 119.1672559 119.1672559
119.1672559 119.1672559 119.1672559 119.1672559 119.1672559 119.1672559
119.1672559 119.1672559 119.1672559 119.1672559 119.1672559 119.1672559
119.1672559 119.1672559 119.1672559 119.1672559 119.1672559 119.1672559
101.1826707 119.1672559 101.1826707 119.1672559 119.1672559 119.1672559
119.1672559 101.1826707 101.1826707 101.1826707 101.1826707 119.1672559
101.1826707 101.1826707 119.1672559 101.1826707 101.1826707 101.1826707
101.1826707 101.1826707 101.1826707 101.1826707 101.1826707 101.1826707
101.1826707 101.1826707 101.1826707 101.1826707 101.1826707 101.1826707
101.1826707 101.1826707 101.1826707 101.1826707 101.1826707 101.1826707
101.1826707 101.1826707 101.1826707 101.1826707 101.1826707 101.1826707
101.1826707 101.1826707 101.1826707 101.1826707 101.1826707 101.1826707
101.1826707 101.1826707 101.0654813 101.1826707 101.1826707 101.1826707
```

101.1826707 101.1826707 101.1826707 101.1826707 101.1826707 29.66041946
101.1826707 101.1826707 101.1826707 119.1672559 101.1826707 83.25498697
101.1826707 101.1826707 83.25498697 101.1826707 101.1826707 101.1826707
83.25498697 101.1826707 83.25498697 101.1826707 101.1826707 119.1672559
101.1826707 101.1826707 101.1826707 83.25498697 101.1826707 101.1826707
83.25498697 83.25498697 83.25498697 83.25498697 101.1826707 83.25498697
83.25498697 83.25498697 83.25498697 83.25498697 83.25498697 83.25498697
101.1826707 83.25498697 83.25498697 83.25498697 83.25498697 83.25498697
83.25498697 83.25498697 83.25498697 83.25498697 83.25498697 83.25498697
83.25498697 83.25498697 83.25498697 83.25498697 83.25498697 83.25498697
83.25498697 83.25498697 83.25498697 83.25498697 83.25498697 83.25498697
83.25498697 83.25498697 101.1826707 83.25498697 83.25498697 83.25498697
83.25498697 83.25498697 101.1826707 83.25498697 83.25498697 83.25498697
83.25498697 83.25498697 101.1826707 83.25498697 83.25498697 83.25498697
101.1826707 83.25498697 83.25498697 83.25498697 83.25498697 83.25498697
83.25498697 83.25498697 83.25498697 83.25498697 83.25498697 83.25498697
83.25498697 83.25498697 83.25498697 83.25498697 83.25498697 83.25498697
83.25498697 83.25498697 83.25498697 65.39308634 83.25498697 83.25498697
65.39308634 83.25498697 83.25498697 83.25498697 83.25498697 83.25498697
83.25498697 83.25498697 83.25498697 83.25498697 83.25498697 83.25498697
83.25498697 83.25498697 83.25498697 83.25498697 83.25498697 83.25498697
83.25498697 83.25498697 83.25498697 83.25498697 83.25498697 83.25498697
83.25498697 83.25498697 83.25498697 83.25498697 65.39308634 83.25498697
83.25498697 83.25498697 83.25498697 83.25498697 83.25498697 83.25498697
83.25498697 83.25498697 83.25498697 83.25498697 83.25498697 65.39308634
83.25498697 65.39308634 83.25498697 83.25498697 83.25498697 83.25498697
83.25498697 65.39308634 83.25498697 83.25498697 83.25498697 83.25498697
83.25498697 65.39308634 83.25498697 65.39308634 65.39308634 65.39308634
65.39308634 65.39308634 65.39308634 65.39308634 83.25498697 65.39308634
65.39308634 83.25498697 65.39308634 65.39308634 65.39308634 65.39308634
65.39308634 65.39308634 65.39308634 65.39308634 83.25498697 65.39308634
65.39308634 65.39308634 65.39308634 65.39308634 65.39308634 65.39308634
65.39308634 65.39308634 65.39308634 65.39308634 65.39308634 65.39308634
65.39308634 65.39308634 65.39308634 83.25498697 65.39308634 65.39308634
65.39308634 65.39308634 65.39308634 65.39308634 83.25498697 65.39308634
65.39308634 65.39308634 65.39308634 65.39308634 65.39308634 65.39308634
65.39308634 65.39308634 65.39308634 83.25498697 83.25498697 65.39308634
65.39308634 65.39308634 65.39308634 65.39308634 65.39308634 65.39308634
83.25498697 65.39308634 65.39308634 65.39308634 65.39308634 47.60300253
65.39308634 65.39308634 65.39308634 65.39308634 65.39308634 65.39308634
65.39308634 65.39308634 65.39308634 65.39308634 65.39308634 65.39308634
65.39308634 65.39308634 65.39308634 65.39308634 65.39308634 29.66041946
65.39308634 65.39308634 65.39308634 65.39308634 65.39308634 65.39308634
65.39308634 65.39308634 65.39308634 65.39308634 65.39308634 65.39308634
65.39308634 65.39308634 65.39308634 65.39308634 65.39308634 65.39308634
65.39308634 65.39308634 65.39308634 65.39308634 65.39308634 65.39308634
65.39308634 65.39308634 65.39308634 65.39308634 65.39308634 65.39308634
83.25498697 65.39308634 65.39308634 65.39308634 65.39308634 65.39308634
65.39308634 65.39308634 65.39308634 65.39308634 65.39308634 65.39308634
65.39308634 65.39308634 65.39308634 65.39308634 65.39308634 65.39308634
65.39308634 65.39308634 65.39308634 65.39308634 83.25498697 65.39308634
65.39308634 65.39308634 65.39308634 65.39308634 65.39308634 65.39308634
65.39308634 65.39308634 65.39308634 83.25498697 65.39308634 65.39308634
65.39308634 65.39308634 65.39308634 65.39308634 65.39308634 65.39308634
65.39308634 65.39308634 65.39308634 65.39308634 65.39308634 65.39308634
65.39308634 65.39308634 65.39308634 65.39308634 47.60300253 65.39308634

65.39308634 65.39308634 65.39308634 65.39308634 65.39308634 65.39308634
65.39308634 65.39308634 65.39308634 65.39308634 65.39308634 65.39308634
65.39308634 65.39308634 65.39308634 65.39308634 65.39308634 47.60300253
65.39308634 47.60300253 65.39308634 65.39308634 65.39308634 65.39308634
65.39308634 65.39308634 65.39308634 65.39308634 65.39308634 65.39308634
65.39308634 65.39308634 65.39308634 65.39308634 65.39308634 65.39308634
65.39308634 47.60300253 101.1826707 47.60300253 47.60300253 65.39308634
47.60300253 47.60300253 47.60300253 47.60300253 47.60300253 47.60300253
47.60300253 47.60300253 29.66041946 47.60300253 65.39308634 47.60300253
47.60300253 65.39308634 65.39308634 47.60300253 47.60300253 65.39308634
47.60300253 47.60300253 47.60300253 47.60300253 47.60300253 47.60300253
65.39308634 65.39308634 65.39308634 47.60300253 65.39308634 47.60300253
47.60300253 65.39308634 47.60300253 65.39308634 47.60300253 47.60300253
47.60300253 47.60300253 47.60300253 47.60300253 65.39308634 47.60300253
47.60300253 47.60300253 47.60300253 47.60300253 47.60300253 47.60300253
65.39308634 47.60300253 47.60300253 47.60300253 47.60300253 47.60300253
29.66041946 47.60300253 47.60300253 47.60300253 47.60300253 47.60300253
47.60300253 47.60300253 47.60300253 47.60300253 47.60300253 47.60300253
47.60300253 47.60300253 47.60300253 47.60300253 47.60300253 47.60300253
47.60300253 47.60300253 47.60300253 47.60300253 65.39308634 47.60300253
47.60300253 47.48581313 47.60300253 47.60300253 47.60300253 47.60300253
47.60300253 47.60300253 47.60300253 47.60300253 47.60300253 65.39308634
47.60300253 65.39308634 47.60300253 47.60300253 47.60300253 47.60300253
47.60300253 65.39308634 47.60300253 47.60300253 47.60300253 47.60300253
47.60300253 47.60300253 47.60300253 47.60300253 29.66041946 47.60300253
47.60300253 47.60300253 47.60300253 47.60300253 47.60300253 47.60300253
47.60300253 47.60300253 47.60300253 47.60300253 47.60300253 47.60300253
47.60300253 47.60300253 47.60300253 47.48581313 47.60300253 47.60300253
47.60300253 47.60300253 47.60300253 47.60300253 47.60300253 47.60300253
47.60300253 47.60300253 47.60300253 47.60300253 47.60300253 47.60300253
47.60300253 47.60300253 47.60300253 47.60300253 47.60300253 47.60300253
47.60300253 47.60300253 47.60300253 47.60300253 47.60300253 47.60300253
47.60300253 65.39308634 47.60300253 47.60300253 47.60300253 47.60300253
65.39308634 47.60300253 47.60300253 47.60300253 47.60300253 47.60300253
47.60300253 47.60300253 47.60300253 47.60300253 47.60300253 47.60300253
47.60300253 47.60300253 29.66041946 47.60300253 47.60300253 47.60300253
47.60300253 47.60300253 47.60300253 47.60300253 47.60300253 47.60300253
65.39308634 47.60300253 47.60300253 47.60300253 47.60300253 47.60300253
47.60300253 47.60300253 65.39308634 47.60300253 47.60300253 47.60300253
47.60300253 47.60300253 47.60300253 47.60300253 47.60300253 47.60300253
47.60300253 47.60300253 47.60300253 47.60300253 83.25498697 47.60300253
47.60300253 47.60300253 47.60300253 47.60300253 47.60300253 47.60300253
47.60300253 47.60300253 47.60300253 47.60300253 47.60300253 47.60300253
47.60300253 47.60300253 47.60300253 47.60300253 47.60300253 47.60300253
47.60300253 47.60300253 47.60300253 47.60300253 47.60300253 47.60300253
47.60300253 47.60300253 47.60300253 47.60300253 47.60300253 47.60300253
47.60300253 47.60300253 47.60300253 65.39308634 47.60300253 47.60300253
47.60300253 47.60300253 65.39308634 47.60300253 47.60300253 47.60300253
47.60300253 47.60300253 47.60300253 47.60300253 47.60300253 47.60300253
47.60300253 47.60300253 47.60300253 47.60300253 47.60300253 47.60300253
47.60300253 47.60300253 47.60300253 47.60300253 47.60300253 47.60300253
47.60300253 47.60300253 47.60300253 47.60300253 47.60300253 47.60300253
47.60300253 47.60300253 47.60300253 47.60300253 47.60300253 47.60300253
47.60300253 47.60300253 47.60300253 47.60300253 47.60300253 47.60300253
65.39308634 47.60300253 47.60300253 47.60300253 47.60300253 47.60300253
47.60300253 47.60300253 47.60300253 47.60300253 29.66041946 47.60300253
65.39308634 47.60300253 47.60300253 29.66041946 47.60300253 47.60300253

```
47.60300253 47.60300253 47.60300253 47.60300253 47.60300253 47.60300253
47.60300253 47.60300253 47.60300253 47.60300253 47.60300253 47.60300253
47.60300253 47.60300253 47.60300253 47.60300253 47.60300253 47.60300253
47.60300253 47.60300253 47.60300253 47.60300253 47.60300253 47.60300253
47.60300253 47.60300253 47.60300253 47.60300253 47.60300253 47.60300253
47.60300253 47.60300253 47.60300253 47.60300253 47.60300253 47.60300253
47.60300253 47.60300253 47.60300253 47.60300253 47.60300253 65.39308634
47.60300253 47.60300253 47.60300253 47.60300253 47.60300253 47.60300253
47.60300253 47.60300253 47.60300253 47.60300253 47.60300253 47.60300253
47.60300253 47.60300253 47.60300253 29.66041946 29.66041946 47.60300253
47.60300253 65.39308634 47.60300253 47.60300253 65.39308634 47.60300253
47.48581313 47.60300253 47.60300253 47.60300253 47.60300253 47.60300253
47.60300253 47.60300253 47.60300253 47.60300253 47.60300253 47.60300253
47.60300253 47.60300253 47.60300253 47.60300253 47.60300253 47.60300253
47.60300253 47.60300253 47.60300253 47.60300253 47.60300253 47.60300253
47.60300253 47.60300253 47.60300253 47.60300253 47.60300253 47.60300253
47.60300253 47.60300253 47.60300253 47.60300253 47.60300253 47.60300253
47.60300253 47.60300253 47.60300253 47.60300253 47.60300253 47.60300253
47.60300253 47.60300253 47.60300253 47.60300253 47.60300253 47.60300253
47.60300253 47.60300253 47.60300253 65.39308634 47.60300253 47.60300253
47.60300253 47.60300253 47.60300253 47.60300253 29.66041946 47.60300253
47.60300253 47.60300253 47.60300253 47.60300253 47.60300253 47.60300253
47.60300253 47.60300253 47.60300253 47.60300253 47.60300253 47.60300253
47.60300253 47.60300253 47.60300253 47.60300253 47.60300253 47.60300253
47.60300253 47.60300253 47.60300253 47.60300253 47.60300253 47.60300253
47.60300253 47.60300253 47.60300253 47.60300253 47.60300253 47.60300253
65.39308634 47.60300253 47.60300253 47.60300253 47.60300253 65.39308634
47.60300253 47.60300253 47.60300253 47.60300253 47.60300253 65.39308634
47.48581313 47.60300253];
T2 = [47.60300253   29.66041946 29.66041946 47.60300253 29.66041946
29.66041946 47.60300253 47.60300253 29.66041946 47.60300253 47.60300253
29.66041946 47.60300253 47.60300253 47.60300253 47.60300253 47.60300253
47.60300253 47.60300253 47.60300253 47.60300253 47.60300253 47.60300253
83.25498697 47.60300253 47.60300253 47.60300253 47.60300253 47.60300253
47.60300253 47.60300253 47.60300253 47.60300253 47.60300253 47.60300253
47.60300253 47.60300253 29.66041946 47.60300253 65.39308634 65.39308634
65.39308634 65.39308634 65.39308634 65.39308634 65.39308634 65.39308634
83.25498697 83.25498697 65.39308634 65.39308634 65.39308634 65.39308634
65.39308634 65.39308634 65.39308634 65.39308634 65.39308634 65.39308634
83.25498697 83.25498697 83.25498697 83.25498697 83.25498697 83.25498697
83.25498697 83.25498697 47.60300253 83.25498697 83.25498697 83.25498697
83.25498697 83.25498697 83.25498697 83.25498697 83.25498697 83.25498697
83.25498697 83.25498697 101.1826707 101.1826707 101.1826707 101.1826707
101.1826707 101.1826707 101.1826707 101.1826707 101.1826707 101.1826707
101.1826707 101.1826707 101.1826707 101.1826707 101.1826707 83.25498697
101.1826707 101.1826707 101.1826707 101.1826707 101.1826707 101.1826707
101.1826707 101.1826707 101.1826707 83.25498697 101.1826707 101.1826707
101.1826707 101.1826707 101.1826707 101.1826707 101.1826707 101.1826707
101.1826707 101.1826707 101.1826707 101.1826707 101.1826707 101.1826707
101.1826707 83.25498697 101.1826707 101.1826707 101.1826707 101.1826707
101.1826707 83.25498697 101.1826707 119.1672559 83.25498697 101.1826707
101.1826707 101.1826707 83.25498697 101.1826707 101.1826707 101.1826707
101.1826707 83.25498697 83.25498697 83.25498697 83.25498697 83.25498697
119.1672559 83.25498697 83.25498697 83.25498697 83.25498697 83.25498697
137.1978206 65.39308634 101.1826707 83.25498697 83.25498697 83.25498697
83.25498697 83.25498697 83.25498697 83.25498697 119.1672559 83.25498697
```

83.25498697 83.25498697 83.25498697 83.25498697 83.25498697 83.25498697
83.25498697 83.25498697 101.1826707 83.25498697 83.25498697 83.25498697
65.39308634 83.25498697 83.25498697 65.39308634 83.25498697 83.25498697
83.25498697 83.25498697 83.25498697 83.25498697 83.25498697 83.25498697
83.25498697 83.25498697 65.39308634 83.25498697 83.25498697 83.25498697
83.25498697 83.25498697 83.25498697 65.39308634 65.39308634 83.25498697
83.25498697 83.25498697 65.39308634 83.25498697 83.25498697 83.25498697
83.25498697 83.25498697 83.25498697 65.39308634 65.39308634 65.39308634
65.39308634 65.39308634 65.39308634 65.39308634 65.39308634 65.39308634
65.39308634 83.25498697 47.60300253 65.39308634 65.39308634 65.39308634
65.39308634 65.39308634 65.39308634 65.39308634 83.25498697 65.39308634
65.39308634 47.60300253 65.39308634 65.39308634 47.60300253 83.25498697
65.39308634 65.39308634 65.39308634 47.60300253 65.39308634 65.39308634
65.39308634 65.39308634 65.39308634 65.39308634 65.39308634 65.39308634
65.39308634 29.66041946 65.39308634 65.39308634 65.39308634 47.60300253
65.39308634 65.39308634 65.39308634 65.39308634 65.39308634 47.60300253
83.25498697 65.39308634 65.39308634 65.39308634 83.25498697 65.39308634
65.39308634 65.39308634 65.39308634 65.39308634 65.39308634 65.39308634
65.39308634 65.39308634 65.39308634 65.39308634 65.39308634 47.60300253
65.39308634 65.39308634 65.39308634 83.25498697 65.39308634 65.39308634
65.39308634 65.39308634 83.25498697 65.39308634 65.39308634 65.39308634
65.39308634 65.39308634 65.27589694 65.39308634 65.39308634 65.39308634
65.39308634 65.39308634 65.39308634 65.39308634 47.60300253 65.39308634
65.39308634 65.39308634 47.60300253 65.39308634 65.39308634 47.60300253
65.39308634 65.39308634 65.39308634 47.60300253 65.39308634 29.66041946
65.39308634 65.39308634 65.39308634 47.60300253 83.25498697 65.39308634
65.39308634 65.39308634 47.60300253 47.60300253 47.60300253 65.39308634
47.60300253 83.25498697 47.60300253 47.60300253 47.60300253 47.60300253
47.60300253 47.60300253 47.60300253 65.39308634 47.60300253 47.60300253
47.60300253 101.1826707 47.60300253 47.60300253 47.60300253 47.60300253
47.60300253 47.60300253 47.60300253 47.60300253 47.60300253 47.60300253
47.60300253 29.66041946 47.60300253 29.66041946 47.60300253 47.60300253
47.60300253 47.60300253 47.60300253 47.60300253 47.60300253 47.60300253
47.60300253 47.60300253 47.60300253 47.60300253 47.60300253 47.60300253
47.60300253 47.60300253 47.60300253 47.60300253 47.60300253 47.60300253
47.60300253 47.60300253 47.60300253 47.60300253 47.60300253 65.39308634
47.60300253 47.60300253 47.60300253 47.60300253 47.60300253 47.60300253
47.60300253 47.60300253 47.60300253 29.66041946 47.60300253 47.60300253
47.60300253 47.60300253 47.60300253 47.60300253 47.60300253 47.60300253
29.66041946 47.60300253 47.60300253 47.60300253 47.60300253 47.60300253
47.60300253 47.60300253 47.60300253 47.60300253 47.60300253 47.60300253
47.60300253 47.60300253 47.60300253 47.60300253 47.60300253 47.60300253
47.60300253 47.60300253 65.39308634 47.60300253 47.60300253 29.66041946
47.60300253 47.60300253 47.60300253 47.60300253 65.39308634 83.25498697
47.60300253 47.60300253 65.39308634 65.39308634 65.39308634 65.39308634
65.39308634 65.39308634 65.39308634 65.39308634 65.39308634 65.39308634
65.39308634 47.60300253 65.39308634 65.39308634 65.39308634 65.39308634
65.39308634 83.25498697 83.25498697 65.39308634 83.25498697 83.25498697
83.25498697 83.25498697 83.25498697 83.25498697 29.66041946 83.25498697
83.25498697 83.25498697 83.25498697 83.25498697 83.25498697 83.25498697
83.25498697 83.25498697 83.25498697 101.1826707 101.1826707 101.1826707
101.1826707 101.1826707 101.1826707 119.1672559 101.1826707 101.1826707
119.1672559 119.1672559 101.1826707 119.1672559 101.1826707 101.1826707
119.1672559 119.1672559 119.1672559 119.1672559 119.1672559 119.1672559
119.1672559 83.25498697 119.1672559 119.1672559 137.1978206 137.1978206
137.1978206 119.1672559 137.1978206 137.1978206 137.1978206 137.1978206
155.2621103 155.2621103 155.2621103 155.2621103 155.2621103 155.2621103

155.2621103 155.2621103 155.2621103 155.2621103 155.2621103 155.2621103
155.2621103 155.2621103 155.2621103 155.2621103 155.2621103 155.2621103
155.2621103 155.2621103 155.2621103 137.1978206 137.1978206 137.1978206
137.1978206 119.1672559 137.1978206 137.1978206 137.1978206 137.1978206
137.1978206 137.1978206 137.1978206 137.1978206 137.1978206 137.1978206
137.1978206 137.1978206 83.25498697 119.1672559 119.1672559 83.25498697
119.1672559 119.1672559 119.1672559 119.1672559 119.1672559 119.1672559
119.1672559 101.1826707 65.39308634 119.1672559 101.1826707 119.1672559
101.1826707 101.1826707 119.1672559 101.1826707 101.1826707 101.1826707
101.1826707 101.1826707 101.1826707 101.1826707 101.1826707 119.1672559
101.1826707 101.1826707 101.1826707 101.1826707 101.1826707 101.1826707
83.25498697 101.1826707 101.1826707 101.1826707 83.25498697 101.1826707
83.25498697 83.25498697 83.25498697 83.25498697 83.25498697 83.25498697
83.25498697 83.25498697 83.25498697 83.25498697 83.25498697 83.25498697
83.25498697 83.25498697 83.25498697 83.25498697 83.25498697 83.25498697
83.25498697 83.25498697 83.25498697 83.25498697 83.25498697 101.1826707
83.25498697 83.25498697 83.25498697 83.25498697 83.25498697 83.25498697
83.25498697 83.25498697 83.25498697 83.25498697 83.25498697 65.39308634
29.66041946 83.25498697 83.25498697 65.39308634 83.25498697 83.25498697
65.39308634 65.39308634 65.39308634 65.39308634 65.39308634 65.39308634
47.60300253 65.39308634 83.25498697 65.39308634 83.25498697 65.39308634
65.39308634 65.39308634 119.1672559 65.39308634 65.39308634 65.39308634
65.39308634 65.39308634 65.39308634 65.39308634 65.39308634 65.39308634
65.39308634 65.39308634 65.39308634 65.39308634 65.39308634 65.39308634
65.39308634 65.39308634 65.39308634 65.39308634 65.39308634 65.39308634
65.39308634 83.25498697 65.39308634 65.39308634 65.39308634 65.39308634
65.39308634 65.39308634 65.39308634 65.39308634 65.39308634 65.39308634
65.39308634 65.39308634 65.39308634 83.25498697 65.39308634 65.39308634
65.39308634 65.39308634 65.39308634 65.39308634 65.39308634 65.39308634
65.39308634 47.60300253 65.39308634 65.39308634 65.39308634 47.60300253
65.39308634 47.60300253 65.39308634 29.66041946 65.39308634 65.39308634
47.60300253 47.60300253 83.25498697 65.39308634 47.60300253 47.60300253
47.60300253 65.39308634 65.39308634 65.39308634 65.39308634 47.60300253
47.60300253 47.60300253 65.39308634 47.60300253 47.60300253 47.60300253
65.39308634 47.60300253 47.60300253 47.60300253 47.60300253 47.60300253
65.39308634 65.39308634 47.60300253 47.60300253 47.60300253 47.60300253
101.1826707 47.60300253 47.60300253 47.60300253 47.60300253 47.60300253
47.60300253 65.39308634 47.60300253 47.60300253 47.60300253 47.60300253
47.60300253 47.60300253 47.60300253 47.60300253 65.39308634 47.60300253
47.60300253 65.39308634 47.60300253 47.60300253 47.60300253 47.60300253
155.2621103 47.60300253 47.60300253 47.60300253 47.60300253 47.60300253
47.60300253 47.60300253 47.60300253 101.1826707 47.60300253 47.60300253
47.60300253 83.13779757 47.60300253 47.60300253 47.60300253 47.60300253
47.60300253 47.60300253 47.60300253 47.60300253 47.60300253 47.60300253
47.60300253 83.25498697 47.60300253 47.60300253 47.60300253 47.60300253
47.60300253 47.60300253 47.60300253 47.60300253 47.60300253 47.60300253
47.60300253 47.60300253 47.60300253 47.60300253 47.60300253 47.60300253
47.60300253 47.60300253 47.60300253 47.60300253 47.60300253 47.60300253
47.60300253 47.60300253 47.60300253 47.60300253 47.60300253 47.60300253
47.60300253 47.60300253 47.60300253 47.48581313 83.25498697 29.66041946
47.60300253 47.60300253 47.60300253 47.60300253 47.60300253 47.60300253
47.60300253 47.60300253 47.60300253 65.39308634 47.60300253 47.60300253
47.60300253 47.60300253 47.60300253 47.60300253 47.60300253 47.60300253
47.60300253 47.60300253 47.60300253 47.60300253 47.60300253 47.60300253
47.60300253 47.60300253 47.60300253 65.39308634 47.60300253 47.60300253
47.60300253 47.60300253 47.60300253 47.60300253 47.60300253 47.60300253
47.60300253 47.60300253 47.60300253 47.60300253 47.60300253 47.60300253

```
47.60300253 47.60300253 47.60300253 47.60300253 47.60300253 47.60300253
47.60300253 47.60300253 29.66041946 47.60300253 47.60300253 47.60300253
47.60300253 47.60300253 47.60300253 47.60300253 47.60300253 47.60300253
47.60300253 47.60300253 47.60300253 47.60300253 47.60300253 47.60300253
65.39308634 47.60300253 83.25498697 65.39308634 47.60300253 47.60300253
47.60300253 47.60300253 101.1826707 47.60300253 47.60300253 47.60300253
47.60300253 47.60300253 47.60300253 47.60300253 47.60300253 47.60300253
47.60300253 47.60300253 47.60300253 47.60300253 47.60300253 47.60300253
47.60300253 47.60300253 47.60300253 83.25498697 47.60300253 47.60300253
47.60300253 47.60300253 47.60300253 47.60300253 47.60300253 47.60300253
47.60300253 47.60300253 47.60300253 47.60300253 47.60300253 47.60300253
47.60300253 47.60300253 47.60300253 47.60300253 47.60300253 47.60300253
47.60300253 47.60300253 47.60300253 47.60300253 47.60300253 47.60300253
47.60300253 47.60300253 47.60300253 47.60300253 47.60300253 47.60300253
47.60300253 47.60300253 47.60300253 47.60300253 47.60300253 47.60300253
47.60300253 47.60300253 47.60300253 47.60300253 47.60300253 83.25498697
83.25498697 47.60300253 47.60300253 47.60300253 47.60300253 47.60300253
47.60300253 47.60300253 47.60300253 47.60300253 47.60300253 47.60300253
47.60300253 47.60300253 29.66041946 47.60300253 47.60300253 47.60300253
47.60300253 47.60300253 29.66041946 47.60300253 65.39308634 29.66041946
47.60300253 47.60300253 47.60300253 29.66041946 47.60300253 29.66041946
29.66041946 47.60300253 47.60300253 29.66041946 47.60300253 29.66041946
47.60300253 47.60300253 47.60300253 29.66041946 29.66041946 47.60300253
47.60300253 47.60300253 47.60300253 47.60300253 47.60300253 65.39308634
47.60300253 47.60300253 29.66041946 47.60300253 47.60300253 47.60300253
29.66041946 47.60300253 47.60300253 29.66041946 47.60300253 47.60300253
47.60300253 29.66041946 47.60300253 47.60300253 65.39308634 47.60300253
47.60300253 29.66041946 47.60300253 47.60300253 47.60300253 47.60300253
47.60300253 47.60300253 47.60300253 29.66041946 47.60300253 83.25498697
47.60300253 29.66041946 47.60300253 29.66041946 47.60300253 29.66041946
47.60300253 47.60300253 47.60300253 47.60300253 47.60300253 29.66041946
29.54323006 47.60300253 47.60300253 29.66041946 29.66041946 29.66041946
47.60300253 29.66041946 47.60300253 47.60300253 47.60300253 47.60300253
29.66041946 29.66041946 47.60300253 47.60300253 47.60300253 47.60300253
29.66041946 47.60300253 29.66041946 47.60300253 47.60300253 47.60300253
29.66041946 47.60300253 29.66041946 47.60300253 29.66041946 47.60300253
47.60300253 47.60300253 47.60300253 47.60300253 47.60300253 47.60300253
47.60300253 29.66041946 47.60300253 29.66041946 29.66041946 29.66041946
47.60300253 47.60300253 29.66041946 47.60300253 29.66041946 47.60300253
47.60300253 47.60300253 47.60300253 29.66041946 29.66041946 47.60300253
47.60300253 47.60300253 47.60300253 29.66041946 29.66041946 29.66041946
47.60300253 29.66041946 29.66041946 83.25498697 47.60300253 29.66041946
29.66041946 29.66041946 47.60300253 29.66041946 47.60300253 29.66041946
47.60300253 47.60300253 29.66041946 29.66041946 29.66041946 29.66041946
29.66041946 29.66041946 47.60300253 47.60300253 29.66041946 47.60300253
47.60300253 47.60300253 47.60300253 47.60300253 29.66041946 47.60300253
47.60300253 47.60300253 29.66041946 47.60300253 47.60300253 47.60300253
47.60300253 47.60300253 47.60300253 47.60300253 47.60300253 47.60300253
29.66041946 29.66041946 47.60300253 47.60300253 47.60300253 47.60300253
47.48581313 47.60300253];

%%%%%%%%%%%%%%%%%%%%%%
%%%%% Single Pass %%%%%
%%%%%%%%%%%%%%%%%%%%%%
for i=1:b
```

```
    R = (((yTC(1,i)^(2))+((w).^(2)))).^(0.5);
  for n=1:a
      temp(i,n) = tzero + (P1/(2* 3.14159 * k * R(1,n)))*exp( -1* vsource*
alpha * w(1,n))*exp( -1*alpha * vsource * R(1,n));
  end
end

plot(t,temp(1,:),t,temp(2,:),t,temp(3,:),t,temp(4,:),t,temp(5,:),t,temp(6,:),
t,temp(7,:));
hleg1 = legend('0.5mm','1 mm', '1.5mm', '2.0 mm', '3.0 mm', '4.0 mm', '5.0
mm')
xlabel('Time [seconds]');
ylabel('Temperature [C]');
```

Peak Temperature as a Function of R

```
clc
clear all
%Efficiency Calculation from: A. J. Pinkerton and L. Li.
%An analytical model of energy distribution in direct metal deposition

%Moving Heat Source models as a moving Point source in 3D from
% Daniel Rosenthal

%Initial Conditions%
ap=.5 ;             %Powder Coupling Eff
as=.5;              %Substrate Coupling Eff
B=900;               %Melt Pool Conduction Calibration Constant
D0= 8.0E-3;          %meters Initial Beam and Powder diameters
D1= 1.0E-3;          %meters Beam diameter at surface
cp = 600.0;          %J/kgK Specific Heat
epsilon= 0.4;        %Emmissivity of melt pool
h= 1E3;              %W/m2K Convective HTC
hfg = 6.8E6;         %J/kg Latent heat of Vaporization
k=51.9;              %W/mK Thermal Conductivity
L= 0.0012;           %m melt pool length
ldeposit = .0762;    %m
Lb= 1.6E-2;          %Beam-powder interaction distance
mdot= 1.08E-4;       %mass flow of powder
P0=290;              %Watts Laser Power
r= 6.065e-5;          %meters Radius of Powder
rho= 7850;           %kg/m3 density of material system
sigma= 67E-8;      %W/m2K4 Boltzman Constant
Tm= 1735;            %K Solidus Temp
T0 = 310.0;          %K Ambient Temperature
Vp= 1.4;             %meters/sec powder velocity
vsource = .002116; %m/s Source Velocity
xTC = .00834 ;        %meters x-Location along deposit of TC
yTC = .00015:.00001:.005;  %meters y-Location from centerline on substrate
surface
zTC = .00015:.00001:.005;       %meters z-Location depth into substrate
z=.0162;             %meters Axial distance below nozzle


%Powder Laser Interaction%
Fv = 4*mdot/(pi()*rho*Vp*(D0^2));
Ab= pi()*((D0*Lb*D0*z)+(D1*z))/(4*(Lb^2));
Pap1= ((3*ap*mdot*D1*Lb*P0)/(pi()*r*Vp*rho*(D0^3)));%Inflight Absorption
Prp1= ((3*(1-ap)*mdot*D1*Lb*P0)/(pi()*r*Vp*rho*(D0^3))); %Inflight reflection
Pap2= ((3*ap*mdot*(D0-D1)*Lb*P0)/(pi()*r*Vp*rho*(D0^3)));%Inflight Absorption
Prp2= ((3*(1-ap)*mdot*(D0-D1)*Lb*P0)/(pi()*r*Vp*rho*(D0^3)));%Inflight
reflection
Psum= Pap1+Prp1+Pap2+Prp2;
P1= as*(P0-Psum)+Pap1;

%Temperature%
```

```
Tpeak = Tm + (P1/(2*pi()*k*D1));
Tmean = Tm + (P1/(4*pi()*k*D1));

%Energy Flow%
Q1C1= (pi()*(D1^2)*k*B)/2;
Q1C2= (pi()*D1*L*k*B)/2;
Q2C1= (pi()*(D1^2)*h)/2;
Q2C2= (pi()*D1*L*h)/2;
Q3C1= (pi()*(D1^2)*epsilon*sigma)/2;
Q3C2= (pi()*D1*L*epsilon*sigma)/2;

Q2= (Q2C1*(Tpeak-T0))+(Q2C1*(Tmean-T0));
Q3= (Q3C1*((Tpeak^4)-(T0^4)))+(Q3C1*((Tmean^4)-(T0^4)));
Q4= (28295*pi()*(D1^2)*hfg*(exp(-
18836/Tpeak)/(sqrt(Tpeak))))+(28295*pi()*(D1*L)*hfg*(sqrt(2)*exp(-
37672/(Tpeak+Tm))/ (sqrt(Tpeak+Tm))));
Q1= P1-Q2-Q3-Q4;
Qsum= Q1+Q2+Q3+Q4;

%Energy Losses

Powderloss= (Prp1+Pap2+Prp2)/P0;
AbsinSurf=P1/P0;
Reflected= ((P0-P1)/P0)-Powderloss;
CondtoSub= Q1/P0;
ConvPoolLoss=Q2/P0;
RadPoolLoss=Q3/P0;
VapPoolLoss=Q4/P0;
SurfRef=P0-P1-Powderloss;
Losstotal= Powderloss+Reflected+CondtoSub+ConvPoolLoss+VapPoolLoss;
Eff=P1/P0;

EnergyBal1= ['%PO Lost to Powder =', num2str(Powderloss)];
EnergyBal2= ['%P0 Reflected off Surface =', num2str(Reflected)];
EnergyBal3= ['%PO Conducted into Substrate=' , num2str(CondtoSub)] ;
EnergyBal4= ['%PO Convected from Pool=' ,num2str(ConvPoolLoss)];
EnergyBal5= ['%P0 Evaporated from Pool=' ,num2str(VapPoolLoss)];
EnergyTotal= ['Energy total=', num2str(Losstotal)];

disp(EnergyBal1);
disp(EnergyBal2);
disp(EnergyBal3);
disp(EnergyBal4);
disp(EnergyBal5);
disp(EnergyTotal);

%Initial Calculations

deposittime=ldeposit/vsource;
alpha = k/ (rho *cp) ; %m2/s
tzero = T0-273.15; %Celcius
t = 0:.01:deposittime;
numofsteps = numel(t);
a = numofsteps;
step = .0005; %mm
```

```
w = xTC - (vsource*t);
stepm = step *1000;
vsourcem = vsource*1000;
ptey=numel(yTC);
ptez=numel(zTC);
localmaxY=zeros(1,ptey);
localmaxZ=zeros(1,ptez);

%%%%%%%%%%%%%%%%%%%%%%
%%%%% Single Pass %%%%%
%%%%%%%%%%%%%%%%%%%%%%

for i=1:ptey
R = ((yTC(1,i)^(2))+((w).^(2))).^(0.5);
for n=1:a
      Pass1(1,n) = tzero + (P1/(2* 3.14159 * k * R(1,n)))*exp( -1* vsource*
alpha * w(1,n))*exp( -1*alpha * vsource * R(1,n));
   end
localmaxY(1,i) = max(Pass1);
end


for j=1:ptez
R = (((zTC(1,j)^(2))*4.84)+((w).^(2))).^(0.5);
for n=1:a
      Pass1(1,n) = tzero + (P1/(2* 3.14159 * k * R(1,n)))*exp( -1* vsource*
alpha * w(1,n))*exp( -1*alpha * vsource * R(1,n));
   end
localmaxZ(1,j) = max(Pass1);
end

plot(yTC,localmaxY,zTC,localmaxZ);
hleg1 = legend('Y-Direction','Z-Direction')
xlabel('Distance from centerline [m]');
ylabel('Temperature (C)');
```

XI. REFERENCES

1. **Liou, Frank, et al.** *Applications of a hybrid manufacturing process for fabrication of metallic structures.* 2007. pp. 236-244.

2. **Mazumder, J., A, Schifferer. and Choi, J.** *Direct Materials Deposition: Designed Macro and Microstructure.* 1999. p. 14. Vol. 3.

3. **Lewis, Gary K., et al.** *Directed Light Fabrication of Near-Net Shape Metal Components.* s.l. : Los Alamos National Laboratory: Materials Sceince and Technology Division, 1994.

4. **DuPont, J.N. and Marder, A.R.** *Dilution ion Single Pass Arc Welds.* s.l. : Metallurgical and Materials Transactions B, June 1996. Volume 27B.

5. **Unocic, R.R and Dupont, J.N.** *Process Efficiency Measurements in the Laser Engineered Net Shaping Process.* 2004. p. 143. Vol. 35B.

6. **de Deus, A.M. and Mazumder, J.** *Two-Dimensional Thermo-Mechanical Finite Element Model for Laser Cladding.* Urbana Illinois : Center for Laser Aided Materials Processing, University of Illinios at Urbana-Champaign.

7. **Peyre, P., et al.** *Analytical and Numerical Modeling of the Direct Metal Deposition Laser Process.* 2008. p. 10.

8. **Labudovic, M. and Kovacevic, D. Hu.** *A Three Dimensional Model for Direct Laser Metal Powder Deposition and Rapid Prototyping.* 2003. p. 15.

9. **Madigan, R. Bruce.** *Measurement and Simulation of Titanium Alloy Deposit Temperature in Electron Beam Additive Manufacturing.* 2012. p. 7. Vol. Proceedings of the 9th International Conference.

10. **Pinkerton, A J and Li, L.** *An analytical model of energy distribution in laser direct metal deposition.* 2004. p. 12. Vol. B.

11. **Lewis, Gary, Nemec, Ron and Thoma, Dan.** *Materials Analyis of Deposits Made by the Directed Light Fabrication Process.* Los Alamos : DOE Office of Scientific and Technical Information, 1995.

12. **Bhattacharya, S., et al.** *Microstructural Evolution of AISI 4340 Steel During Direct Metal Deposition.* 2011. p. 9.

13. **Kumar, Subodh, et al.** *Determination of Layer Thickness in Direct Metal Deposition.* 2013. p. 6. Vol. 67.

14. **Hochanadel, Patrick, et al.** *The Microstructure and mechanical properties of type 316 stainless produced by directed light fabrication (DLF) technology.* San Antonio, Texas : TMS Annual Meeting, 1998.

15. **Jang, Jeong-Hwan, et al.** *Characterization of Deposited Layer Fabrication by Direct Laser Melting Process.* s.l. : Metals and Materials International, 2013. Vol. 19.

16. **Rosenthal, Daniel.** *Mathematical Theory of Heat Distribution During Welding and Cutting.* 1941. pp. 220-234.

17. **Choi, M, Greif, R and Salcudean, M.** *A study of the heat transfer during arc welding with applications to pure metals or alloys and low or high boiluing temperature materials.* 1987. p. 11.

18. **Touloukian, Y. S., et al.** Thermophysical Properties of Matter. *Volume 12: Thermal Expansion of Metallic Elements and Alloys.* New York : Plenum, 1970.

19. **Touloukian, Y. S., et al.** Thermophysical Prosperties of Matter. *Volume 10: Thermal Diffusivity.* New York : Plenum, 1970.

20. **Touloukian, Y.S and Buyco, E.H.** Thermophysical Properties of Matter. *Volume 4: Specifc Heat of Metallic Elements and Alloys.* New York : Plenum, 1970.

21. **Touloukian, Y.S., et al.** Thermophysical Properties of Matter. *Volume 1: Thermal Conductivity of Metallic Elements and Alloys.* New York : Plenum, 1970.

22. **Pollack.** *Material Science and Metallurgy 4th Ed.* s.l. : Prentice-Hall, 1988.

23. **Atkins, M.** *Atlas of Continuous Cooling Transformation Diagrams for Engineering Steels.* Sheffield, UK : British Steel Corporation, 1980.

24. **Heilbronner, Renee.** *How to Derive Size Distributions of Particles from Size Distrubitions of Sectional Areas.* Basel, Switzerland : Department of Earth Sciences, Basel University, 2002.

25. **Jominy, W.E.** *Hardenability of Alloy Steels.* Metals Park, Ohio : American Society for Metals, 1939.

26. **Brooks, Charles R.** *Principles of the Heat Treatment of Plain Carbon and Low-Alloy Steel.* Materials Park, Ohio : ASM International, 1996.

27. **Kern, R.F. and Suess, M.E.** *Steel Selection.* New York : Wiley, 1979.

28. **Thoma, D.J., et al.** *Directed Light Fabrication of Iron-Based Materials.* s.l. : Materials Research Society, 1996. Volume 397.

29. **Zeng, Kai, Pal, Deepankar and Stucker, Brent.** *A Review of Thermal Analysis Methods in Laser Sintering and Selective Laser Melting.* Louisville, KY : Department of Industrial Engineering, University of Loiusville, 2012.